Modification strategies and photocatalytic performance investigation of ceria-based photocatalyst materials

著者	Yang　Hui
その他のタイトル	CeO2光触媒材料の改良指針と光触媒性能に関する研究
学位授与年度	令和4年度
学位授与番号	17104甲工第575号
URL	http://doi.org/10.18997/00009180

Doctoral (Engineering) Dissertation

Modification strategies and photocatalytic performance investigation of ceria-based photocatalyst materials

Kyushu Institute of Technology
Graduate School of Engineering

Major: Engineering, Graduate School of Engineering

205F8003 Hui Yang

Contents

Part 1.

Introduction of photocatalysis principle and ceria-based photocatalyst materials

1.1 Background of photocatalysis

Since the 21st century, the rapid renewal and progress of industry has promoted the prosperity of economy, but also effectively improved people's living standards and boosted the development of human society [1-4]. Solar energy is a pure and limitless source of energy, but as the industrialization process worsens the energy issue, its application study is becoming more and more vital. The conversion of solar energy into electricity using solar cells is by far the most common application of it [5]. However, this path also has some impedes of energy storage, transmission and utilization efficiency. Another technique to convert solar energy directly into useful chemical energy is through processes that result in the creation of H_2 from water vapor decomposition reactions or the conversion of carbon dioxide into fossil fuels including methane.

On the other hand, a variety of industrial pollutants, including organic dye pollutants, organic volatile gas pollutants or heavy metal pollutants, are produced in this process and become difficult puzzles to be solved urgently [2]. In the process of seeking solutions, photocatalysis is considered to be one of the most potential pollution control technologies because of its advantages of high efficiency, non-toxicity and low cost in the degradation of organic pollutants. Although the history of photocatalysis can be traced back to 1960s, we usually take as the starting point of the photocatalysis investigation in 1972s, when A. Fujishima and K. Honda first used n-type semiconductor TiO_2 electrode to decompose H_2O under ultraviolet light. Since then, as a new semiconductor material, TiO_2 has attracted researcher's enthusiastic attention. They mainly focus on the principle of photocatalysis, enhancement of the photocatalytic efficiency, improvement of the visible light absorption and expansion of TiO_2-based photocatalysts application range [2, 5].

According to the International Union of Pure and Applied Chemistry (IUPAC) group,

photocatalytic reaction refers that a reaction is accelerated by the absorption of light in conjunction with a catalyst material. In other words, photocatalysis is the use of light energy to catalyze reactions, so the catalyst material and light at the same time can accelerate chemical reactions. The energy band structure of semiconductor is usually composed of a valence band (VB) full of electrons and an empty conduction band (CB). The difference area between valence band and conduction band is the band gap, and the value of this area is usually called energy band gap (E_g). For a semiconductor, the potential value of the electrons on CB position is between -1.5 V and +0.5 V (vs. NHE), which mainly shows reduction ability. On the other hand, the holes on VB position display strong oxidation efficiency, and the potential is between +1.0 V and +3.5 V (vs. NHE). Because the process of obtaining the final products by photocatalysis involves many possible reaction processes, its mechanism is quite complex. However, with the development of the research of photocatalysis, it has been extended to energy, health, environment, pollution control, synthesis and other fields. We believe that the further photocatalysis technology will bring us great benefits with its broad prospect in the near future [6, 7].

1.2 Principle of photocatalytic reactions

Photogenerated charges mainly participated in the following processes as shown in **Figure 1-1** during photocatalysis process:

(a) The photocatalyst is excited by absorbing photons from light. Then photogenerated charge is diffused and transferred to the surface of the photocatalyst for redox reactions with adsorbed reactants. When the photogenerated electron and hole meet on the surface of the photocatalyst, surface recombination will occur as shown in ***Path A***. If photogenerated electron holes meet and react in the interior of the photocatalyst, volume recombination will occur as shown in ***Path B***.

(b) In the case of photoexcited electrons or holes, they can diffuse and transfer to the semiconductor's outer surface, where they can subsequently be absorbed by the reactants, thus catalyzing the reactions. The electron transfer process is more efficient if the pre-absorbed material (such as O_2) is already present on the surface of the catalyst. Then, the semiconductor can catalyze the reduction reaction by injecting photogenerated electrons into the reduction acceptor (such as CO_2) on the surface, as shown in ***Path C***.

(c) On the other hand, when photogenerated holes are transferred to the semiconductor surface, here, the composite flooding photocatalytic oxidation reaction of holes from the electron donor material (H_2O) energy and the surface is carried out as shown in ***Path D***. Therefore, the separation degree of photogenerated charge is an important factor affecting the photocatalytic activity.

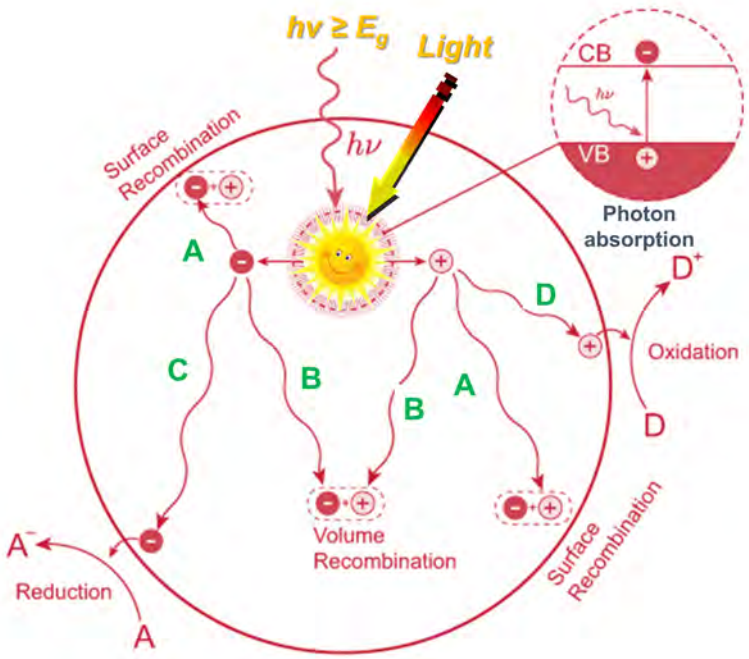

Figure 1-1. Basic mechanism of photocatalytic reaction steps of redox process on the surface of photocatalyst.

Different from the traditional thermodynamic catalytic reactions, photocatalytic reactions can be carried out by optical drive either spontaneously ($\Delta G<0$) or non-spontaneously ($\Delta G>0$). No matter

the radiation energy of the light is equal or higher than the band gap (E_g) of the semiconductor, then on its surface, numerous photoexcited electron-hole pairs will be produced. With the help of various oxidation and reduction reactions, these photogenerated electrons and holes will effectively transform reactants into end products. However, if the electrons or holes cannot be trapped by the reactants, or if the energy of the light radiation cannot completely excite the semiconductor, the photogenerated electrons and holes will rapidly recombine and then release their energy as ineffective heat energy. In general, the photocatalytic activity of materials mainly depends on the following four aspects: (a) the composition of the reaction medium, (b) the absorptive capacity of the material surface, (c) the type of semiconductor and its crystal/morphological characteristics, and (d) the absorptive capacity of light.

1.3 Introduction of ceria-based photocatalyst materials

The unique 4f electronic structure of rare earth elements made their compounds to be widely used in optical, electrical and magnetic, material conversion and storage fields. In addition, materials modified by rare earth elements or their compounds will have these special properties, and a variety of new materials are developed for catalysis, electronics, energy, environmental protection, biomedicine and other fields. The atomic number of cerium (Ce) element is 58 and it is the most abundant and the cheapest among all the rare earth elements **(Figure 1-2)**. And the abundance of cerium element in the crust is 68 ppm, it occupied almost fifty percentage of the rare earth elements and occupying about 0.0046 wt% of the earth's crust. A face-centered cubic unit cell of cations makes up CeO_2's fluorite cubic crystal structure, which has a lattice constant of 5.41134 Å (angstrom) [5, 7]. Anions occupy the octahedral interstitial sites, and each cerium is placed in this structure in a face-centered cubic surrounded by eight oxygen anions. In the meantime, oxygen filled every tetrahedral location, and each oxygen anion has four cerium cations bound to it. In this open structure, which is

conducive to electron transportation, there could be formed a great deal of octahedral vacancies. The fundamental defect in CeO_2 is the development of oxygen vacancies, which are brought on by the transition of Ce^{3+} and Ce^{4+}. So, the more Ce^{3+} concentration means there are more oxygen vacancies developed in the overall cerium.

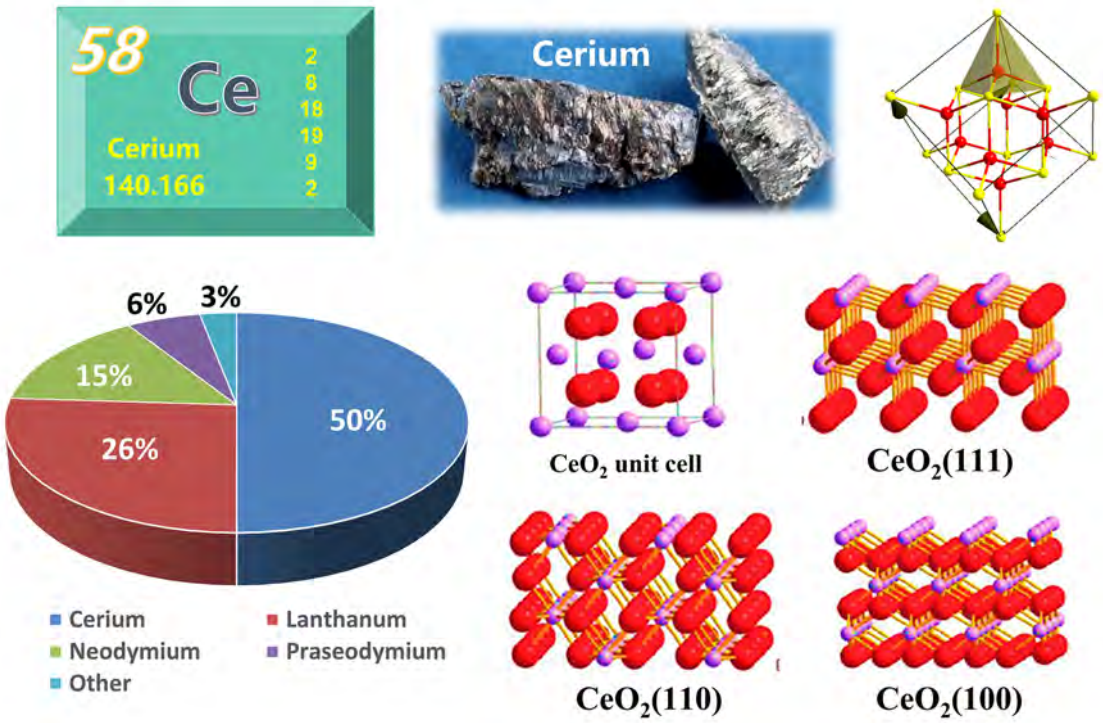

Figure 1-2. Atomic number of cerium, the proportion of rare earth elements in the Earth's crust, cerium dioxide cell and cerium crystal face.

Photocatalysis is based on the band theory of n-type semiconductor, in which a kind of light-involved redox reaction with n-type semiconductor as catalyst. Most of the semiconductors used for photocatalysis are metal oxides and sulfides. Commonly used n-type semiconductors are TiO_2, ZnO, CdS, Fe_2O_2, SnO_2, WO_2, etc [4, 7, 11]. With the progress of research, many other types of materials also have been applied to photocatalysis, such as organic polymer materials such as metal-organic skeleton (MOF) and conjugated organic skeleton (COF) photocatalyst. However, the photocatalytic activity and efficiency of these photocatalysts are not particularly high due to the drawbacks of narrow

light absorption range and rapid carrier recombination rate, which is not favorable for popularization and application. The chemical properties of cerium are extraordinary, with an outer electron configuration is of $4f^1$, $5d^1$, and $6s^2$. Thus, cerium, like other rare earth elements, can exist in a positive trivalent state, but also in a stable positive tetravalent state. This valence variability has a significant effect on the properties of its compounds. CeO_2 is a versatile material usually made of cerium hydroxide or trivalent cerium salt precursors.

In recent years, CeO_2-based materials have been widely used with increasing demand in various high-end technology industries all over the world. CeO_2-based materials have been widely used in UV blocking agent, polishing materials, photocatalysts, electrolytes, sensors and fuel cells. These outstanding performances are mainly attributed to their unique oxygen storage capacity, which can be flexibly converted between trivalent and tetravalent cerium. So far, China has made great progress in cerium dioxide production, application and export. Although China is the largest exporter of rare earth elements, but many applications technology are lack of achievement, therefore a more in-depth study on its properties and mechanism should be deserved for researchers in the past few decades. But the CeO_2-based materials recently reported do exhibit several issues, such as a high photoelectron-hole recombination rate, poor photochemical stability, and a weak capacity to absorb visible light, which seriously restricts their use as inexpensive semiconductor photocatalysts [5, 7, 9]. Also, CeO_2-based materials have attracted more attention recently in the realm of photocatalysis, and have even been used as an alternative to traditional TiO_2 photocatalyst in the applications such as wastewater treatment and water decomposition to produce H_2 and O_2.

1.4 Synthetic methods of ceria-based photocatalyst materials

As we all known, some factors of specific surface area, particle size and oxygen defects or

vacancies can affect the photocatalytic properties of ceria [4, 5]. The synthesis method of ceria plays a decisive role in the various applications, so it is very significant to explore the actual method detailly. The preparation process of ceria-based photocatalysts is mainly by chemical methods, such as precipitation method, solvothermal (hydrothermal) method, calcination method, sol-gel method, electrochemical method and so on [6-13]. Additionally, creating CeO_2 nanomaterials sometimes involves combining two or more techniques. Calcination method usually involves grinding the precursor containing the element cerium (for example, cerium salt and cerium hydroxide) in proportion, fully mixing and calcination at high temperature under different atmosphere conditions. Its advantages are low equipment requirements, relatively simple operation and large output. However, its obvious disadvantage is large particle size, serious agglomeration without regular morphology. On the contrary, the gas phase method is a high requirement for the instrument, but the product particles are small and not easy to unite. In this process, the precursor of cerium is heated into the gas phase and then subjected to physical or chemical reactions to produce the product.

Precipitation method, solvothermal reaction method, sol-gel method, electrochemical method, and other methods mostly carried out in liquid phase combine the advantages of solid phase method, and avoid the disadvantage of high equipment requirements of gas phase method, and have been widely used in the synthesis of ceria-based materials [6-13]. The liquid phase method always controls the properties of ceria nanoparticles by adjusting the concentration, reaction time, reaction temperature, solvent and atmosphere during the reaction systems. Besides, one of the popular crystallographic structure-directed techniques is precipitation, in which a small nanocrystal can form under the control of the crystallographic structure using water or an organic solvent as a solvent. Following the use of basic chemicals to precipitate aqueous cerium salt, the precipitates are heated. And the pH value, concentration of the solution, precipitation agent and reaction temperature, agent

time are the key factor influence. Electrochemical deposition is one of these, this method is influenced by the current density (commonly high current density are benefit for small nanocrystal), organic additive, and PH value, temperature and so on.

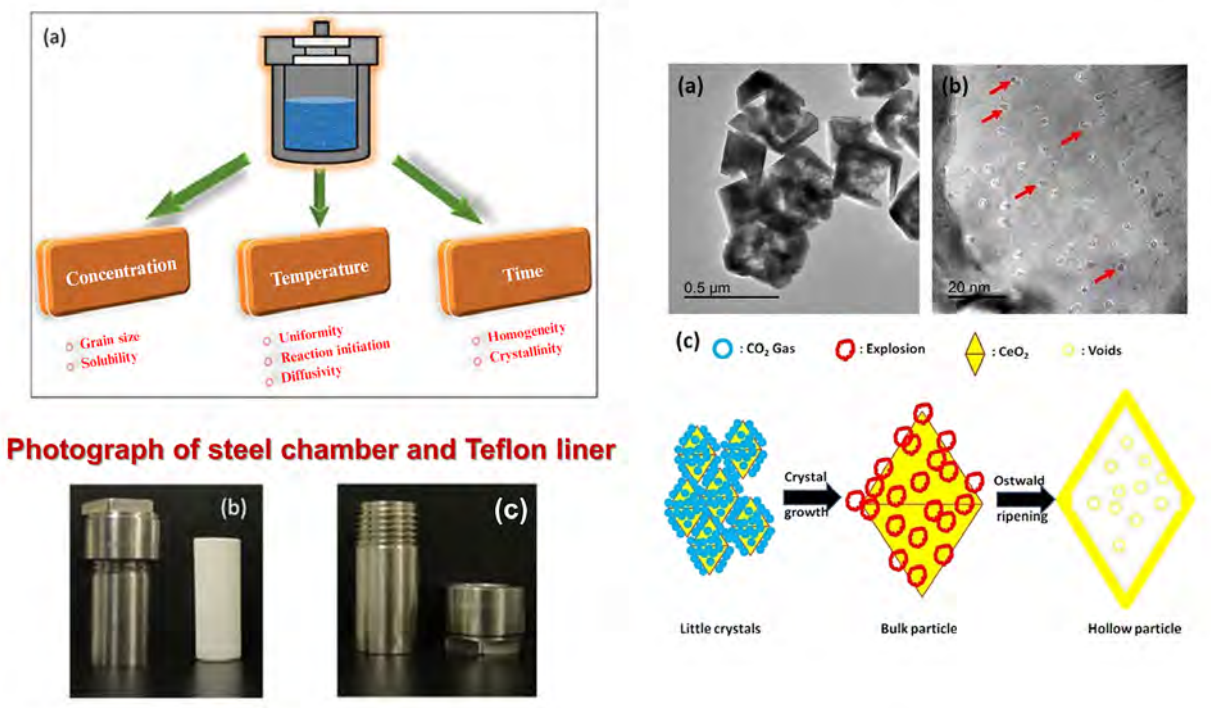

Figure 1-3. Schematic of autoclave used in the solvothermal process and feasible scheme of the hollow structure formation process.

Solvothermal reaction method can make the reactants fully contact in the gas-liquid state under high temperature and high pressure, which is conducive to the growth of crystal **(Figure 1-3)**. Therefore, this method has been widely used in the preparation of new crystal materials, and its growth mechanism has been studied deeply in the lab [6]. Sol-gel method is widely used in ceramic industry and material science, and is suitable for the preparation of most metal oxide (cerium dioxide). While the items lack regular morphologies, it is simple to use and does not require any particular setup. In conclusion, contemporary shape-controlled synthesis techniques were methodically developed in terms of the formation mechanism for materials based on CeO_2. Additionally, the

benefits and drawbacks of each of these approaches have been thoroughly examined. Future fundamental study must focus on the CeO_2 crystal structure in conjunction with contemporary methods.

1.5 Modification strategies of ceria-based photocatalyst materials

The ultimate modification goal is to improve the photocatalytic properties of CeO_2-based materials [5, 13]. Improving the photocatalytic performance generally starts from two aspects: the transformation of its own performance and the addition of other materials to make up for its own shortcomings. The modification itself can be carried out on morphology, specific surface area, oxygen vacancy content, energy band structure and so on. Moreover, the modification around the addition of other components is usually aimed at enhancing the ability to absorb visible light while preventing photoexcited electron-hole pair recombination.

1.5.1 Morphology control

The performance of materials is greatly influenced by their morphologies, which determines the adsorption capacity for reactants and reactive sites of photocatalysts [14-18]. Different morphologies often manifest as the exposure of different crystal planes. According to calculations using the density functional theory, stability has the following order: (111) > (110) > (100), whereas activity has the reverse trend [15, 16]. On the (110) and (100) planes, there are more oxygen vacancies, which is advantageous for photocatalytic processes. As shown in the **Figure 1-4**, Li and co-workers prepared CeO_2-based homojunction composed of octahedra anchored with hexahedral prism by the solid solution crystal oriented epitaxial growth method, in which the prism plane is {100} plane and the octahedral plane is {111} plane [15]. The efficiency of the CO_2 to CH_4 photocatalytic reduction is

increased, according to photocatalytic measurements, by the prism arm generated on the octahedron's inert octahedral CeO_2.

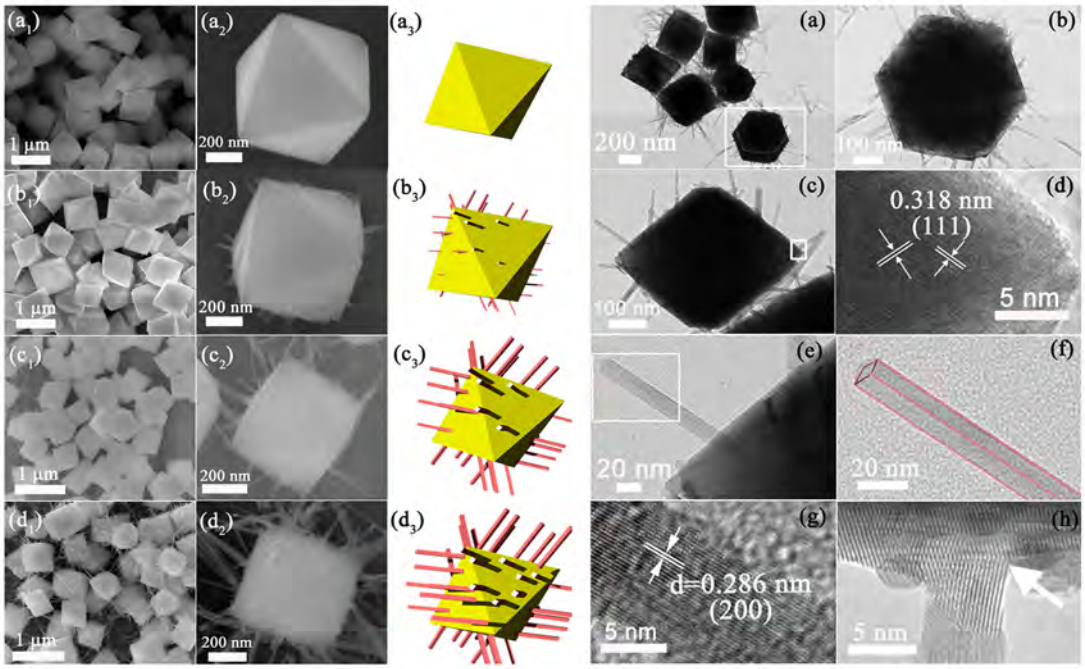

Figure 1-4. SEM and TEM images of hexahedron prism anchored octahedral CeO_2; HRTEM images derived from rectangles of panels, respectively; and HRTEM image of the CeO_2 hexahedron prism arm and the octahedron interface.

1.5.2 Elements doping

In addition, ion doping is one of the effective methods to affect the transmission of photogenerated electrons and holes or change the energy band structure, thus improving the photocatalytic performance [17-19, 21, 22, 25, 26]. It mainly refers to the introduction of ions into the CeO_2 lattice, and doping can efficiently introduce new charges, form defects and change the lattice structure. As reported that rare earth elements (La, Y and Sm) doped ceria nanorods are promising photocatalysts with high activity [20]. The results show that the degradation rate of methylene blue in 10% Y-doped CeO_2 photocatalyst is the highest of 85.59%. This is due to the significantly increased oxygen vacancy concentration and the decreased recombination rate of e^-/h^+ pairs. A highly effective

Fenton-like photocatalyst for the activation of peroxymonosulfate (PMS) was reported by Wang et al. using three-dimensional layered H_2-reduced Mn-doped CeO_2 constructed by nanotubes **(Figure 1-5)**. The produced Re-Mn-CeO_2 NMs exhibit impressive catalytic performance, outstanding redox performance, plentiful oxygen vacancies, a clear adsorption capability, good stability, and a large specific surface area [23].

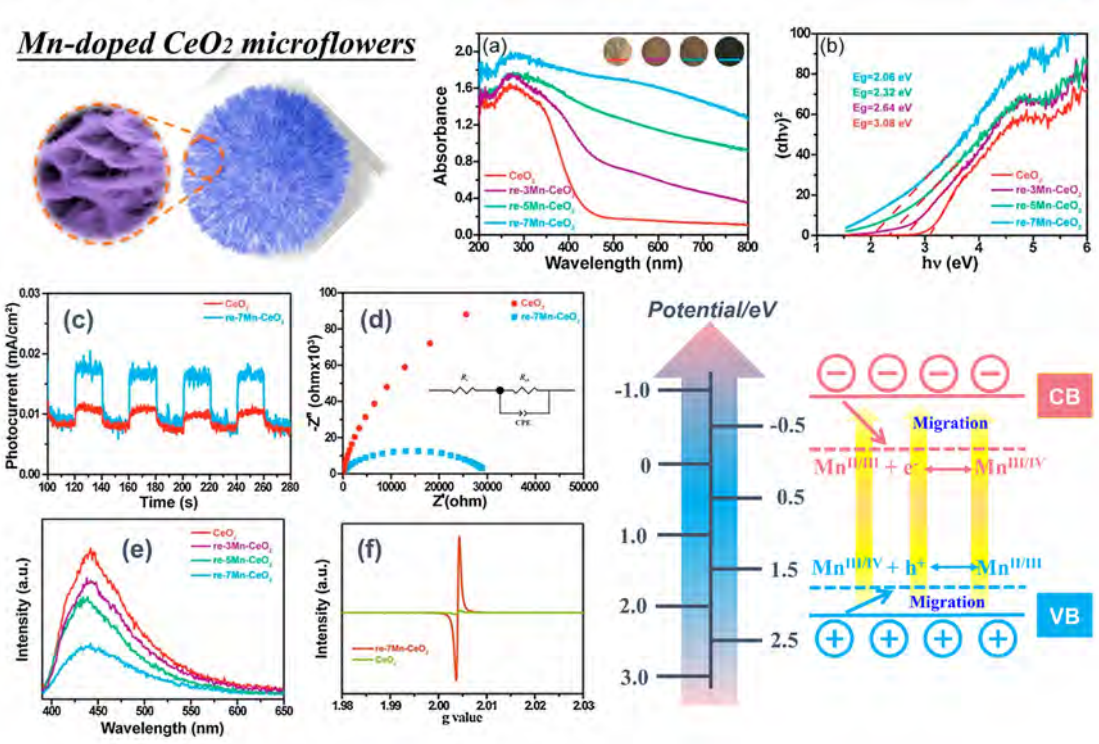

Figure 1-5. (a) UV–vis DRS spectra, (b) Tauc's plots, (c) Transient photocurrent responses, (d) EIS Nyquist plots, (e) PL spectra, (f) EPR spectra, and the possible Fenton-like photocatalytic mechanism for tetracyclines degradation on the re-Mn-CeO_2 NMs/PMS/Vis.

In addition, Shen et al. also prepared a novel nitrogen-doped CeO_2 nanosheet with relatively ordered mesoporous structure (NMCe) by a simple and inexpensive urea-assisted template method **(Figure 1-6)**. NMCe shares structural similarities with nanocasted ordered mesoporous CeO_2 (OMCe), including crystal structure, pore size, and specific surface area. Due to the addition of nitrogen, the band energy of NMCe catalyst decreases, but the concentration of Ce^{3+} and oxygen vacancies on the surface increases. Therefore, NMCe has an extended spectral response in the process

of photocatalytic reactions, which reduces the recombination rate of photogenerated electron-hole pairs, resulting in good adsorption capacity of CO_2 and excellent photocatalytic activity [24].

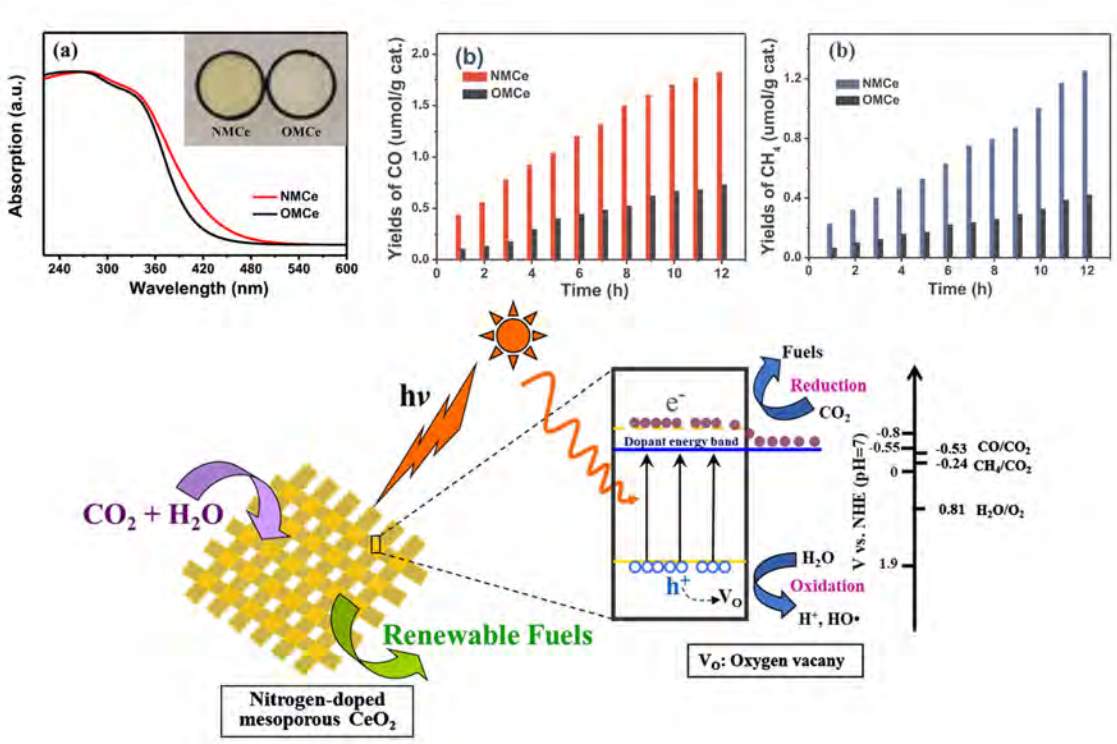

Figure 1-6. (a) UV-vis DRS spectra with insets of digital pictures, (b-c) CO and CH_4 productivity on the NMCe and OMCe, and (d) Potential causes for increased productivity performance of CO and CH_4 to CO_2 on the NMCe.

1.5.3 Noble metal modification

The noble metals modification can affect the surface properties of CeO_2-based materials by changing electron distribution in the system, and then improve its photocatalytic activity. It has been reported that Au has the best modification capacity, but the cost is too high [27-31]. It indicated that the Au/CeO_2 dual group spectrophotometric catalyst had stronger photocatalytic NO removal performance and higher NO conversion efficiency under visible light irradiation **(Figure 1-7)**. Theoretical density function calculations and actual findings indicate that oxygen vacancies on CeO_2 can effectively start O_2 adsorption and activation processes and generate $\cdot O_2^-$. Au nanoparticles placed

on CeO_2 surface are the active center of NO activation and adsorption to create NO^+ when exposed to visible light. Au has the property of surface plasmon resonance, which can improve the absorption efficiency of visible light, so that the efficiency of photocatalytic NO conversion has been greatly improved [27].

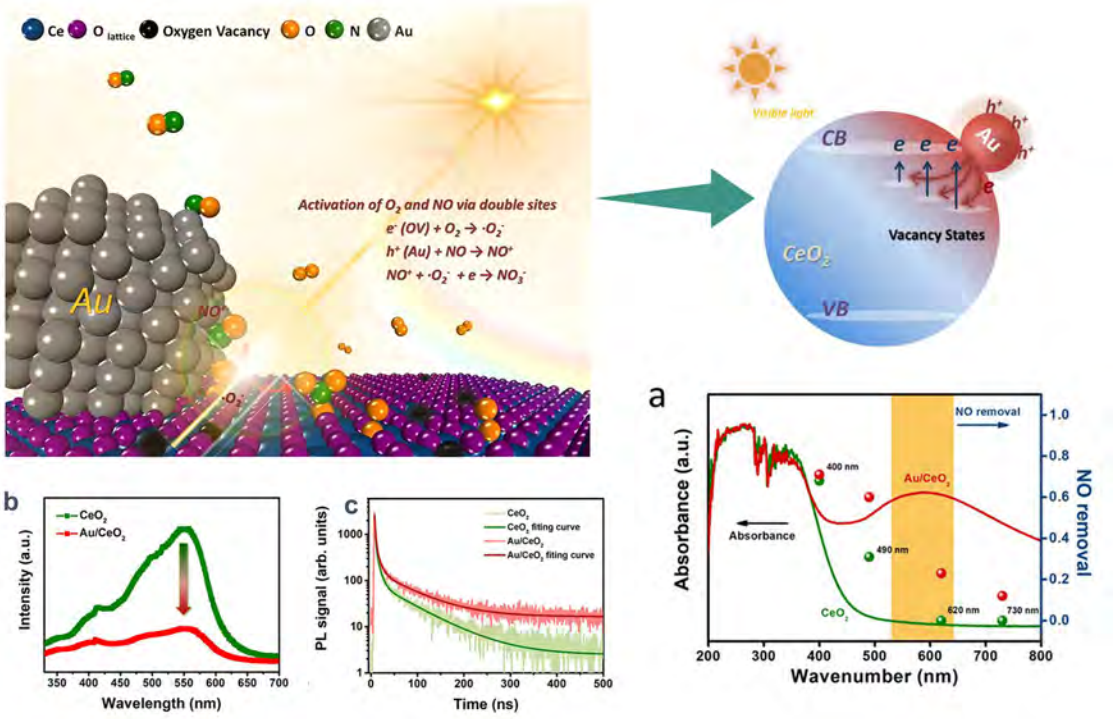

Figure 1-7. Corresponding electronic excitation process with (a) Photocatalytic NO removal over Au/CeO_2 under monochromatic light irradiation, (b) Room temperature steady-state PL spectra and (c) corresponding dynamic decay curves.

By contrast, Ag modification has less toxicity and lower cost than Au. As reported by Samai and co-workers, the photocatalytic activity of AgNC/CeO_2 was increased several times due to the existence of reactive oxygen species compared with pure CeO_2 NPs, even at very low loads of AgNC (about 3%). In addition, Dao et al. investigated the mechanism of enhancing the photocatalytic degradation of Auramine (AO, 92%) by Ag NPs modification after 90 min of visible light irradiation, and pointed out that Ag-CeO_2 nanocomposites have good photocatalytic stability for dye degradation based on the local surface plasmonic resonance (LSPR) effect of Ag NPs [31].

1.5.4 Composite with other materials

In order to improve the absorption of visible light and inhibit the recombination of photogenerated electrons and holes more directly, one simple and effective method is to combine CeO_2 with other materials with high visible light response [32-38]. As reported layered WO_3-CeO_2 hollow spherical heterojunctions were prepared by a two-step hydrothermal method and applied to the visible light degradation of sulfamerazine [34]. This is explained by the effective charge carrier separation made possible by the development of oxygen vacancies at the junction of the two coupled semiconductors. In addition, the hydroxide radical is the primary active ingredient, according to Mott-Schottky calculations, free radical trapping tests, and ESR analysis. The S-scheme charge transfer mechanism is hypothesized to account for its improved photocatalytic activity.

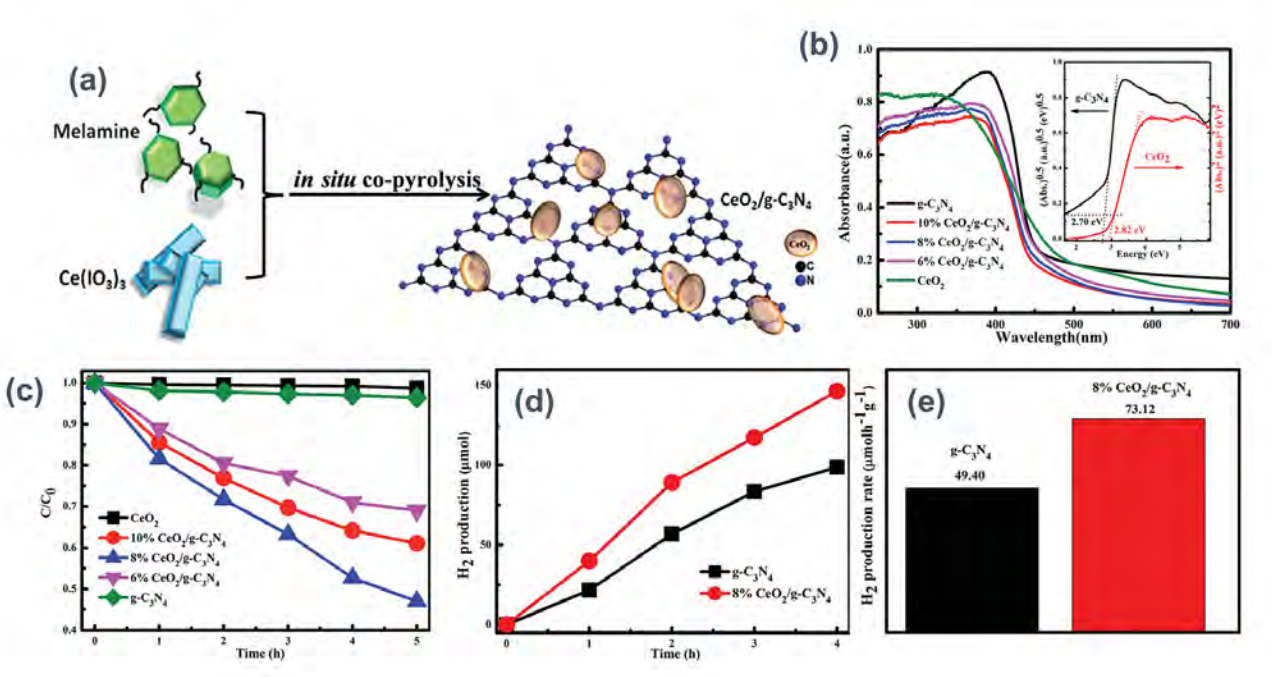

Figure 1-8. (a) Schematic representation of the formation of CeO_2/g-C_3N_4, (b) UV-vis diffuse reflectance spectra of g-C_3N_4, CeO_2 and CeO_2/g-C_3N_4 samples, and band gaps of g-C_3N_4 and CeO_2, (c) Photocatalytic degradation curves of phenol, (d) H_2 production curves and (e) H_2 production rate of g-C_3N_4 and 8% CeO_2/g-C_3N_4 under visible light irradiation ($\lambda > 420$ nm).

Tian's group also prepared CeO_2/g-C_3N_4 composites by in-situ co-pyrolysis of $Ce(IO_3)_3$ and

melamine as precursors **(Figure 1-8)**. The n-n heterojunction of CeO_2/g-C_3N_4 was constructed to form close interaction between the phase interface. Under visible light irradiation, CeO_2/g-C_3N_4 displays strong photocatalytic activity for phenol degradation and NO elimination. The ability of photoexcited carriers to separate and transfer is benefited by this [32]. Additionally, CeO_2 supported on graphitic carbon nitride (g-C_3N_4) composites were made, according to Zou and colleagues, for use in photocatalytic hydrogen (H_2) generation [33]. Additionally, because to its numerous oxygen vacancies and redox-coupled Ce^{4+}/Ce^{3+}, quantum-sized cerium dioxide (CeO_2) exhibits excellent light absorption and high catalytic activity, making it a suitable material for creating better photochemical (PEC) sensors. However, its wide bandgap and aggregation effect limit the photoelectric conversion efficiency, so it is rarely used in the field of photoelectric conversion sensing. Ouyang et al. also addressed these two obstacles by coupling CeO_2 quantum dots (QDs) with graphite carbon nitride (g-C_3N_4) and Au nanoparticles (NPs) [37]. Furthermore, Liang and co-workers also prepared porous microspheres M-ZnO/CeO_2 (M = Ag, Au) photocatalysts by simple hydrothermal and in situ photo-deposition methods. The photocatalyst showed good stability and high efficiency for complete mineralization of non-polar gas molecules (CH_4 and C_2H_4) under simulated sunlight. The formation of heterojunction and oxygen vacancy defects, surface plasmon resonance (SPR) of noble metal nanoparticles and 3D porous microsphere structure are the main reasons for the significant improvement [38].

1.6 Investigation of photocatalytic applications

A variety of photocatalyst materials are applied to water and air purification, self-cleaning, anti-fogging, self-disinfection, antibacterial and other fields [39, 40]. CeO_2 photocatalysts have drawn a lot of interest in these domains because of their high catalytic efficiency, chemical stability,

affordability, low toxicity, and good compatibility [62-65]. Meanwhile, they are crucial in the elimination of microbes including bacteria and viruses as well as the inactivation of some cancer cells. In addition, CeO_2 can also be used to photo dissociate H_2O to produce H_2, which provides a clean and sustainable energy source [39, 40].

1.6.1 VOCs degradation

The indoor volatile organic compounds (VOCs) pollution, which are caused by things like cooking, secondhand smoking, cleaning, consumer goods, home furnishings, and construction materials, among other things, have a significant impact on people's health. The organic substances in the air and waste water, is thought to be the main reason causing many diseases, such as cancer, respiratory disease, sick building syndrome and so on [41-44]. In general, air pollution and waste pollution are becoming more and more important problems for our civilization. The photocatalysis technology can remove VOCs and degrade them into odorless products that are harmless to humans, such as H_2O and CO_2 of minimum molecular weight. Our research group has successfully prepared CeO_2 with different octahedra, rod, ball and broom morphologies, and investigated their photocatalytic degradation performance using acetaldehyde pollutants as models. For instance, uniform and monodisperse porous hollow cerium dioxide spheres (CeO_2-PH) were prepared by a simple solvothermal method without template. CeO_2-PH expresses high activity in evaluating acetaldehyde decomposition. The degradation efficiencies of P-25, CeO_2-NP, and CeO_2-PH are around 5%, 25%, and 92%, respectively, under 24 hours of visible light irradiation [41]. The CeO_2-PH sample had activity that was roughly four times more than CeO_2-NP's and eighteen times greater than P25's (which was unresponsive to visible light). Ce^{3+} ions can lower CeO_2-PH's band gap, increasing the material's capacity to absorb light. During photocatalysis, a significant number of

oxygen vacancies also offer a large number of CeO_2-pH active sites.

1.6.2 Wastewater treatment

Industrial wastewater contains large numbers of natural or synthetic dyes, but also contains trace amounts of heavy metal ions, these pollutants have great harm to the human body, so it must be effectively treated before discharge of wastewater [45-50]. Many semiconductor materials, especially composite materials, can be used as photocatalysts for wastewater treatment. Compared with the traditional precipitation separation and other methods, the photocatalysis technology can not only adsorb but also degrade the dye directly. Guan et al. successfully prepared an efficient and recyclable composite photocatalyst by grafting Ag/AgCl/CeO_2 on the surface of cotton fabric [45]. The results show that Ag/AgCl/CeO_2 modified cotton fabric has good photocatalytic activity. Under visible light, 99.5% of MB, 95.2% of RhB and 92.6% of MO could be degraded within 180 min **(Figure 1-9)**.

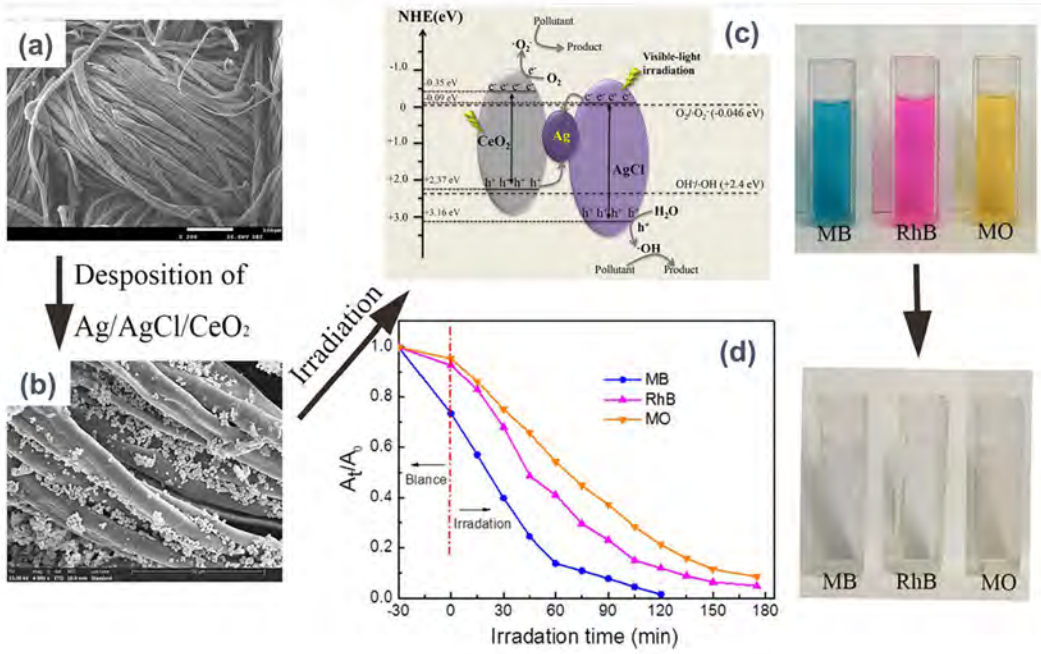

Figure 1-9. SEM images of (a) CF, (b) Ag/AgCl/CeO_2-CF, (c) Possible photocatalytic mechanism of MB with Ag/AgCl/CeO_2–CF Possible photocatalytic mechanism of MB with Ag/AgCl/CeO_2-CF.

In addition, Zhang et al. reported a simple synthesis method to obtain Pd@hCeO$_2$ hollow core-shell nanocomposites, which consist of Pd nanoparticle cores encapsulated in CeO$_2$ hollow shells [49]. For the heterogeneous thermos-catalytic and photocatalytic selective reduction of aromatic nitro compounds in water at room temperature, the Pd@hCeO$_2$ composite can be employed as an effective and multifunctional catalyst. Each component, whether it is the semiconductor CeO$_2$ shell or the Pd metal core, contributes to the same ultimate result in these two distinct catalytic processes in a required but quite different way. Importantly, Pd@hCeO$_2$ has good reusability and higher catalytic performance than the loaded Pd/CeO$_2$.

1.6.3 Water splitting to release hydrogen or oxygen

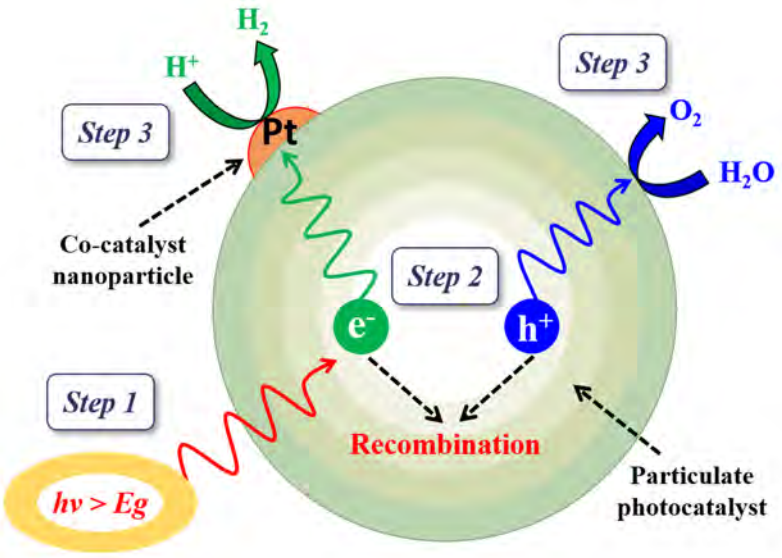

Figure 1-10. Mechanism of photocatalytic reaction steps of hydrogen production process.

Since 1972, when Akira Fujishima and Kendo Hondo first discovered that H$_2$O can yield H$_2$, a large number of semiconductor materials have shown their ability to photocatalytic splitting of H$_2$O [51-59]. **Figure 1-10** shows the photocatalytic decomposition mechanism of H$_2$O, which is based on a semiconductor material and loaded with a cocatalyst on the surface to increase the adsorption

capacity of the reactant or increase the charge transfer rate. If the potential of valence band and conduction band of semiconductor material meet the potential of H_2O decomposition, then the photocatalysis process can be carried out.

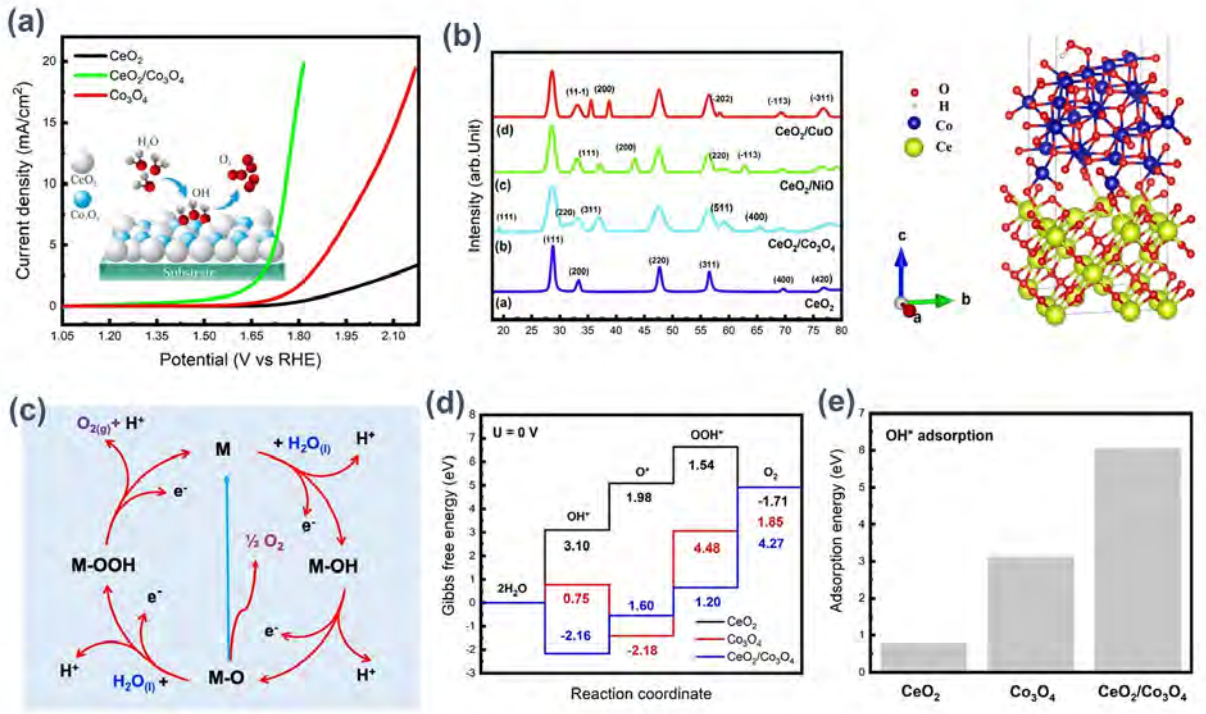

Figure 1-11. (a) iR-corrected curve, (b) XRD patterns, (c) The crystal structures of the unit cells of the FCC fluorite phase CeO_2 with space group Fm3m and of spinel-phase Co_3O_4 with space group Fd3m, where yellow, red, and blue atoms indicate Ce, O, and Co, respectively, (c) Illustration of the four-step mechanism for the adsorption of OH*, O*, and OOH* intermediates during the OER process. (c) Gibbs free energies computed using DFT for the OER process at zero potential. (d) Adsorption energy of OH* determined using DFT on CeO_2, Co_3O_4, and CeO_2/Co_3O_4.

Albu et al. synthesized and characterized CeO_2/Co_3O_4, CeO_2/CuO, and CeO_2/NiO nanoparticles [51]. The initial potential and photoactivity of CeO_2/Co_3O_4 were significantly higher than that of CeO_2 and Co_3O_4 alone **(Figure 1-11)**. This improvement was further investigated by density functional theory (DFT) calculations, and it was found that the adsorption preference and reaction free energy at the CeO_2/Co_3O_4 heterogeneous interface played an important role in the enhancement of water oxidation reactions (OER).

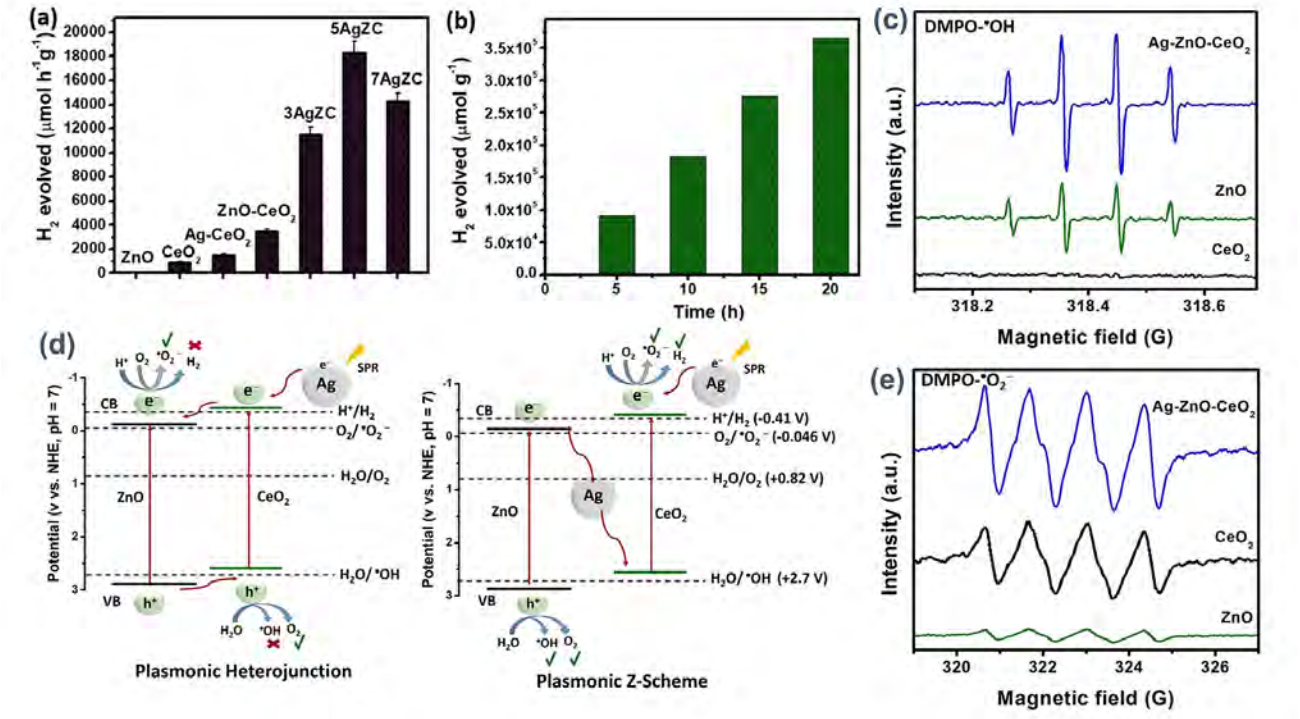

Figure 1-12. (a) H_2 production over various photocatalysts under simulated sunlight illumination, (b) H_2 production over 5AgZC for 20 hours, (c) DMPO-·OH and (e) DMPO-·O_2^- ESR signals for CeO_2, ZnO, and 5AgZC after 15 minutes, and (d) Mechanism of Ag-CeO_2-ZnO heterostructured photocatalyst charge carrier transport and photocatalytic H_2 generation.

In addition, Hezam et al. also combined surface plasmonic resonance and Z-type charge transport in Ag-ZnO-CeO_2 heterostructured photocatalysts to improve their photocatalytic hydrogen production performance **(Figure 1-12)**. Ag plays a dual role as an electron medium, facilitating the transport of Z-scheme charges and maximizing the light absorption of the plasmonic material in the visible region [57]. According to the principles of thermodynamics, electrons in the more negative conduction band will be transferred to another semiconductor, while holes in the more positive valence band will be transferred to another semiconductor. In this way, effective charge separation can be achieved, the rebinding rate of photogenerated charge holes can be inhibited, and the photocatalytic efficiency can be improved. This work provides the opportunity to construct efficient Z-Scheme photocatalysts with full visible light response, inhibition of electrons and holes recombination, and optimization of redox potential using wide bandgap semiconductors.

1.6.4 CO_2 reduction

The reduction of carbon dioxide to hydrocarbons using photocatalysis is extremely challenging [39, 40, 60, 61], but at the same time opens the way to a sustainable energy source that can be used as an alternative to fossil fuels, with the following advantages: (a) It can be done under relatively mild conditions of room temperature and pressure; (b) The process uses large amounts of emitted CO_2 as a carbon source and is driven by inexhaustible amounts of clean solar energy; (c) CO_2 photoreduction can directly generate methane, methanol, ethane and other short-chain hydrocarbon fuels to alleviate the increasingly serious energy crisis; (d) The realization of this technology will make it possible to use carbon dioxide from the chemical industry as a carbon source to replace fossil fuels. Therefore, using photocatalytic reduction technology to synthesize hydrocarbon fuels from CO_2 and H_2O can kill two birds with one stone in terms of energy conservation and environmental protection.

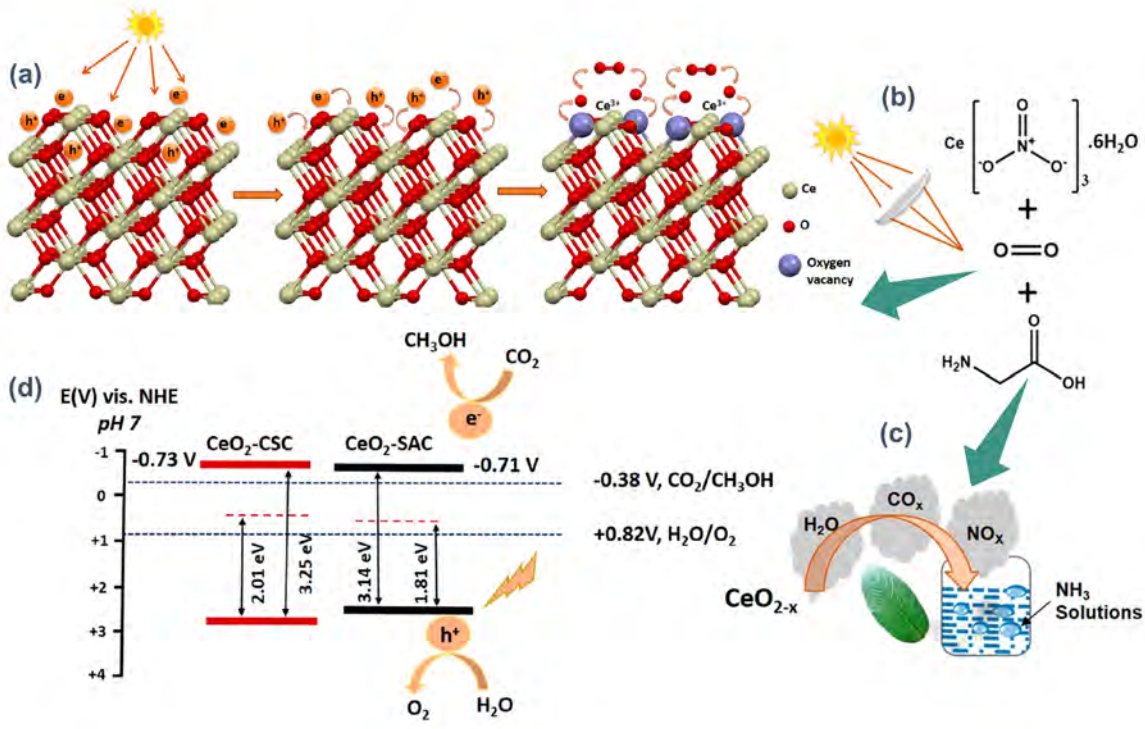

Figure 1-13. (a) Generation mechanism of oxygen vacancies, (b) Schematic diagram for sunlight-driven combustion synthesis of CeO_2 enriched with oxygen vacancies (CeO_{2-x}), and (c) Energy band position diagram of CeO_2-CSC and CeO_2-SAC.

Hezam et al. reported a method for the synthesis of nano-metal oxides (CeO_2) by sun-assisted combustion (**Figure 1-13**). Using sunlight as a clean renewable energy source for the first time, exothermic combustion reaction was initiated to introduce oxygen vacancies into CeO_2 [60]. It has been found that the sunlight-assisted combustion synthesis of CeO_2 (CeO_2-SAC) has a smaller particle size, a higher oxygen vacancy concentration and a narrower band gap than CeO_2-CSC. Therefore, the photocatalytic CO_2 to CH_3OH conversion performance of CeO_2-SAC (0.702 $\mu mol \cdot h^{-1} \cdot g^{-1}$) was higher than that of CeO_2-CSC (0.397 $\mu mol \cdot h^{-1} \cdot g^{-1}$), which indicated the environmental protection of photocatalytic CO_2 emission reduction.

1.7 Conclusions

Cerium (Ce), as the element with the highest abundance among rare earth elements, is famous for its simple preparation method, high oxygen storage capacity and stable chemical properties of the oxide form cerium oxide (CeO_2). CeO_2-based nanomaterials also have attracted extensive attention due to their unique luminescence, magnetic and electrical properties, which bring about remarkable advantages of high efficiency, non-toxicity, and low cost in photocatalytic degradation of industrial chemical pollutants. Actually, CeO_2-based materials have been in growing demand in various high-end technology industries all over the world, and in particular have made great strides of the production, application and export of CeO_2 in China.

In the last decade, CeO_2-based materials have received increasing attention in the field of photocatalysis, and can even be used as a substitute for traditional TiO_2 photocatalysts in applications of wastewater treatment, water splitting to produce hydrogen and oxygen. However, as a photocatalyst material, these recently created CeO_2 also presents some problems that need to be solved, such as high electron-hole pairs recombination rate, lack of active sites and weak absorption

capacity of visible light, which greatly hinder its application as a low-cost photocatalyst.

1.8 Purpose of this research

In this dissertation, different modification strategies are combinedly used to improve the photocatalytic efficiency of CeO_2-based materials. The performance improvement is generally attributed to two aspects: one is the modification itself and the other is the addition of other materials to make up for its own shortcomings. The former can be carried out in terms of morphology, specific surface area, active oxygen vacancy concentration and energy band structure. The latter is in terms of the addition of other components are usually designed to improve visible light absorption and inhibit photogenerated electron-hole pairs recombination. In this dissertation, several effective modification strategies for improving the photocatalytic efficiency of CeO_2-based materials, such as morphology control, element doping, noble metal deposition and heterogeneous structure construction, as well as the current mainstream application trend and mechanism research of photocatalysis are studied in detail. The traditional method of single photocatalytic performance regulation was abandoned, and a variety of modification strategies such as active crystal surface regulation, band gap regulation, surface plasmon resonance enhancement and heterojunction construction were combinedly applied to improve the performance of CeO_2-based photocatalysts.

Hence, the specific research contents mainly consist of the following three parts:

1. **Synthesis and mechanism investigation of enhanced photooxidation performance on broom-like (Sm, Y, La and Nd)-doped CeO_2 photocatalysts**

As previous reporter verified that morphology regulation and ion doping both have positive effects on the photocatalytic degradation performance of CH_3CHO toxic pollutants. Therefore, this chapter aims to further explore the influence of RE ions doping on the photocatalytic performance of

CeO_2, and these CeO_2 photocatalysts doped with different rare earth ions (RE = Sm, Y, La, Nd) were prepared by templated hydrothermal method. The results showed that Sm doped CeO_2 (SC) had better photooxidation activity, and the degradation activity of bisphenol A (BPA) and acetaldehyde (CH_3CHO) were 3.0 and 8.5 times of that of undoped CeO_2, respectively. The concentration of oxygen vacancy (Ov) in SC is highest, and abundant Ov can be used as the capture center of photogenerated electrons, forming doping transition states between conduction band (CB) and valence band (VB), effectively limiting the recombination rate of electrons and holes, and significantly improving the photooxidation performance. In addition, highly active hydroxyl radicals ($\cdot OH$) and superoxide radicals ($\cdot O_2^-$) are efficient intermediates with good oxidation capacity, and their production can further improve the photocatalytic activity finally.

2. Improving photocatalytic activity of waxberry-like CeO_2 via samarium doping and silver quantum dots anchoring

Although the samarium (Sm) ion doping strategy can effectively improve the performance of CeO_2 photocatalyst, it only responds well to UV light, and still has the problems of weak absorption of visible light and low utilization efficiency. Therefore, this chapter introduces Ag quantum dots for anchoring based on Sm ion doping strategy, we prepared waxberry-like CeO_2 photocatalyst by Sm doping and Ag quantum dot anchoring (named ASC) with visible-light-driven photocatalytic multifarious performance. The results showed that the activity of the ASC in CH_3CHO removal and H_2 production of H_2O reduction was 7.08-times and 6.83-times higher than that of pure CeO_2, respectively. In addition, the migration mechanism of photo-generated carriers is described by the transient photovoltage (TPV), surface photovoltage (SPV) and density functional theory (DFT) calculation. Sm doping reduces band gap and doping-related transition states can capture electrons. Then these captured electrons are further transferred to the co-catalytic site of the anchored Ag

quantum dots, which enhances the synchronous absorption and utilization efficiency of visible light.

3. Preparation of Y-doped CeO_2/PCN heterojunction photocatalyst with promoted photooxidation and photoreduction performance

Carbon nitride (PCN) materials have been widely used in various fields because of their advantages such as low cost, easy synthesis, suitable energy band structure, high chemical property and thermal stability. However, PCN still faces problems such as fast recombination rate of photogenerated electron-hole pairs, low specific surface area and limited active sites during photocatalysis.

In this chapter, Y-doped CeO_2 and PCN heterojunction (YCC) photocatalysts were prepared, and the photocatalytic performance of YCC was systematically evaluated by the degradation of RhB and H_2 production of H_2O reduction under visible light. Y-doped CeO_2 and PCN complement each other in performance enhancement thanks to their highly matched band structure positions and tight interfacial connections between the two components. So an effective internal electric field is established, and in this way, these electron-hole pairs are effectively separated and the recombination rate is greatly reduced. In this chapter, doping and heterostructural construction methods not only improve the optical utilization of visible light, but also effectively inhibit the recombination of photogenerated carriers, which is conducive to promoting the improvement of photoredox performance synergistically.

Reference

1. A. Trovarelli, J. Llorca, Ceria Catalysts at Nanoscale: How Do Crystal Shapes Shape Catalysis?, ACS Catalysis, 7 (2017) 4716-4735.
2. A.H. Mamaghani, F. Haghighat, C.-S. Lee, Photocatalytic oxidation technology for indoor environment air purification: The state-of-the-art, Applied Catalysis B: Environmental, 203 (2017) 247-269.
3. X. Yue, N.L. Ma, C. Sonne, R. Guan, S.S. Lam, Q. Van Le, X. Chen, Y. Yang, H. Gu, J. Rinklebe, W. Peng, Mitigation of indoor air pollution: A review of recent advances in adsorption materials and catalytic oxidation, J Hazard Mater, 405 (2021) 124138.
4. Y. Li, W. Shen, Morphology-dependent nanocatalysts: rod-shaped oxides, Chem Soc Rev, 43 (2014) 1543-1574.
5. D. Zhang, X. Du, L. Shi, R. Gao, Shape-controlled synthesis and catalytic application of ceria nanomaterials, Dalton Trans, 41 (2012) 14455-14475.
6. A. Kashyap, N.K. Singh, M. Soni, A. Soni, Deposition of thin films by chemical solution-assisted techniques, Chemical Solution Synthesis for Materials Design and Thin Film Device Applications, (2021), 79-117.
7. H. Yang, B. Xu, Q. Zhang, S. Yuan, Z. Zhang, Y. Liu, Z. Nan, M. Zhang, T. Ohno, Boosting visible-light-driven photocatalytic performance of waxberry-like CeO_2 by samarium doping and silver QDs anchoring, Applied Catalysis B: Environmental, 286 (2021).
8. J. Zhang, S. Ohara, M. Umetsu, T. Naka, Y. Hatakeyama, T. Adschiri, Colloidal Ceria Nanocrystals: A Tailor-Made Crystal Morphology in Supercritical Water, Advanced Materials, 19 (2007) 203-206.
9. C. Chen, M. Li, Y. Jia, R. Chong, L. Xu, X. Liu, Surface defect-engineered silver silicate/ceria p-n heterojunctions with a flower-like structure for boosting visible light photocatalysis with mechanistic insight, J Colloid Interface Sci, 564 (2020) 442-453.
10. C.H.T. Tseng, B.K. Paul, C.-H. Chang, M.H. Engelhard, Continuous precipitation of ceria nanoparticles from a continuous flow micromixer, The International Journal of Advanced Manufacturing Technology, 64 (2012) 579-586.
11. N.C. Strandwitz, G.D. Stucky, Hollow Microporous Cerium Oxide Spheres Templated by Colloidal Silica, Chemistry of Materials, 21 (2009) 4577-4582.
12. C. Tyrsted, K.M. Jensen, E.D. Bojesen, N. Lock, M. Christensen, S.J. Billinge, B. Brummerstedt Iversen, Understanding the formation and evolution of ceria nanoparticles under hydrothermal conditions, Angew Chem Int Ed Engl, 51 (2012) 9030-9033.
13. Z. Wang, R. Yu, Hollow Micro/Nanostructured Ceria-Based Materials: Synthetic Strategies and Versatile Applications, Adv Mater, 31 (2019) e1800592.
14. B. Xu, Q. Zhang, S. Yuan, S. Liu, M. Zhang, T. Ohno, Synthesis and photocatalytic performance of yttrium-doped CeO_2 with a hollow sphere structure, Catalysis Today, 281 (2017) 135-143.

15. P. Li, Y. Zhou, Z. Zhao, Q. Xu, X. Wang, M. Xiao, Z. Zou, Hexahedron Prism-Anchored Octahedronal CeO_2: Crystal Facet-Based Homojunction Promoting Efficient Solar Fuel Synthesis, J Am Chem Soc, 137 (2015) 9547-9550.

16. G. Spezzati, A.D. Benavidez, A.T. DeLaRiva, Y. Su, J.P. Hofmann, S. Asahina, E.J. Olivier, J.H. Neethling, J.T. Miller, A.K. Datye, E.J.M. Hensen, CO oxidation by Pd supported on CeO_2(100) and CeO_2(111) facets, Applied Catalysis B: Environmental, 243 (2019) 36-46.

17. B. Xu, Q. Zhang, S. Yuan, S. Liu, M. Zhang, T. Ohno, Synthesis and photocatalytic performance of yttrium-doped CeO_2 with a hollow sphere structure, Catalysis Today, 281 (2017) 135-143.

18. B. Xu, Q. Zhang, S. Yuan, M. Zhang, T. Ohno, Morphology control and photocatalytic characterization of yttrium-doped hedgehog-like CeO_2, Applied Catalysis B: Environmental, 164 (2015) 120-127.

19. B. Xu, H. Yang, Q. Zhang, S. Yuan, A. Xie, M. Zhang, T. Ohno, Design and Synthesis of Sm, Y, La and Nd-doped CeO_2 with a broom-like hierarchical structure: a photocatalyst with enhanced oxidation performance, ChemCatChem, 12 (2020) 2638–2646.

20. X. Xia, J. Li, C. Chen, Y.-P. Lan, X. Mao, F. Bai, Optimal rare-earth (La, Y and Sm) doping conditions and enhanced mechanism for photocatalytic application of ceria nanorods, Nanotechnology, 32 (2021).

21. P. Venkataswamy, D. Jampaiah, A.E. Kandjani, Y.M. Sabri, B.M. Reddy, M. Vithal, Transition (Mn, Fe) and rare earth (La, Pr) metal doped ceria solid solutions for high performance photocatalysis: Effect of metal doping on catalytic activity, Research on Chemical Intermediates, 44 (2017) 2523-2543.

22. A. Singhania, High Surface Area M (M = La, Pr, Nd, and Pm)-Doped Ceria Nanoparticles: Synthesis, Characterization, and Activity Comparison for CO Oxidation, Industrial & Engineering Chemistry Research, 56 (2017) 13594-13601.

23. A. Wang, Z. Zheng, H. Wang, Y. Chen, C. Luo, D. Liang, B. Hu, R. Qiu, K. Yan, 3D hierarchical H_2-reduced Mn-doped CeO_2 microflowers assembled from nanotubes as a high-performance Fenton-like photocatalyst for tetracycline antibiotics degradation, Applied Catalysis B: Environmental, 277 (2020) 119171.

24. Z. Shen, Q. Xia, Y. Li, C. Yin, Z. Ge, X. Li, Y. Wang, Adsorption-enhanced nitrogen-doped mesoporous CeO_2 as an efficient visible-light-driven catalyst for CO_2 photoreduction, Journal of CO_2 Utilization, 39 (2020) 101176.

25. J. Hao, W. Zhan, L. Sun, G. Zhuang, X. Wang, X. Han, Combining N, S-Codoped C and CeO_2: A Unique Hinge-like Structure for Efficient Photocatalytic Hydrogen Evolution, Inorg Chem, 59 (2020) 937-942.

26. W.H.M. Abdelraheem, M.K. Patil, M.N. Nadagouda, D.D. Dionysiou, Hydrothermal synthesis of photoactive nitrogen- and boron-codoped TiO_2 nanoparticles for the treatment of bisphenol A in wastewater: Synthesis, photocatalytic activity, degradation byproducts and reaction pathways, Applied Catalysis B: Environmental, 241 (2019) 598-611.

27. H. Shang, S. Huang, H. Li, M. Li, S. Zhao, J. Wang, Z. Ai, L. Zhang, Dual-site activation enhanced photocatalytic removal of no with Au/CeO_2, Chemical Engineering Journal, 386 (2020).

28. S. Song, X. Liu, J. Li, J. Pan, F. Wang, Y. Xing, X. Wang, X. Liu, H. Zhang, Confining the Nucleation of Pt to In Situ Form (Pt-Enriched Cage)@CeO_2 Core@Shell Nanostructure as Excellent Catalysts for Hydrogenation Reactions, Adv Mater, 29 (2017).

29. N. Zhang, Y.-J. Xu, Aggregation- and Leaching-Resistant, Reusable, and Multifunctional Pd@CeO_2 as a Robust Nanocatalyst Achieved by a Hollow Core–Shell Strategy, Chemistry of Materials, 25 (2013) 1979-1988.

30. D. Van Dao, T.T.D. Nguyen, H.-Y. Song, J.-K. Yang, T.-W. Kim, Y.-T. Yu, I.-H. Lee, Ionic liquid-assisted preparation of Ag-CeO_2 nanocomposites and their improved photocatalytic activity, Materials & Design, 159 (2018) 186-194.

31. B. Samai, S. Chall, S.S. Mati, S.C. Bhattacharya, Role of Silver Nanoclusters in the Enhanced Photocatalytic Activity of Cerium Oxide Nanoparticles, European Journal of Inorganic Chemistry, 2018 (2018) 3224-3231.

32. N. Tian, H. Huang, C. Liu, F. Dong, T. Zhang, X. Du, S. Yu, Y. Zhang, In situ co-pyrolysis fabrication of CeO_2/g-C_3N_4 n–n type heterojunction for synchronously promoting photo-induced oxidation and reduction properties, Journal of Materials Chemistry A, 3 (2015) 17120-17129.

33. W. Zou, B. Deng, X. Hu, Y. Zhou, Y. Pu, S. Yu, K. Ma, J. Sun, H. Wan, L. Dong, Crystal-plane-dependent metal oxide-support interaction in CeO_2/g-C_3N_4 for photocatalytic hydrogen evolution, Applied Catalysis B: Environmental, 238 (2018) 111-118.

34. A. Bahadoran, S. Ramakrishna, S. Masudy-Panah, J. Roshan De Lile, B. Sadeghi, J. Li, J. Gu, Q. Liu, Novel S-scheme WO_3/CeO_2 heterojunction with enhanced photocatalytic degradation of sulfamerazine under visible light irradiation, Applied Surface Science, 568 (2021).

35. C. Liu, D. Mao, J. Pan, J. Qian, W. Zhang, F. Chen, Z. Chen, Y. Song, Fabrication of highly efficient heterostructured Ag-CeO_2/g-C_3N_4 hybrid photocatalyst with enhanced visible-light photocatalytic activity, Journal of Rare Earths, 37 (2019) 1269-1278.

36. J. Nie, G. Zhu, W. Zhang, J. Gao, P. Zhong, X. Xie, Y. Huang, M. Hojamberdiev, Oxygen vacancy defects-boosted deep oxidation of NO by β-Bi_2O_3/$CeO_{2-\delta}$ p-n heterojunction photocatalyst in situ synthesized from Bi/Ce(CO_3)(OH) precursor, Chemical Engineering Journal, 424 (2021) 130327.

37. X. Ouyang, L. Tang, C. Feng, B. Peng, Y. Liu, X. Ren, X. Zhu, J. Tan, X. Hu, Au/CeO_2/g-C_3N_4 heterostructures: Designing a self-powered aptasensor for ultrasensitive detection of Microcystin-LR by density functional theory, Biosens Bioelectron, 164 (2020) 112328.

38. X. Liang, P. Wang, Y. Gao, H. Huang, F. Tong, Q. Zhang, Z. Wang, Y. Liu, Z. Zheng, Y. Dai, B. Huang, Design and synthesis of porous M-ZnO/CeO_2 microspheres as efficient plasmonic photocatalysts for nonpolar gaseous molecules oxidation: Insight into the role of oxygen vacancy defects and M=Ag, Au nanoparticles, Applied Catalysis B: Environmental, 260 (2020).

39. R. Ma, S. Zhang, T. Wen, P. Gu, L. Li, G. Zhao, F. Niu, Q. Huang, Z. Tang, X. Wang, A critical review on visible-light-response CeO_2-based photocatalysts with enhanced photooxidation of organic pollutants, Catalysis Today, 335 (2019) 20-30.

40. T. Montini, M. Melchionna, M. Monai, P. Fornasiero, Fundamentals and Catalytic Applications of CeO_2-Based Materials, Chem Rev, 116 (2016) 5987-6041.

41. S. Yuan, Q. Zhang, B. Xu, Z. Jin, Y. Zhang, Y. Yang, M. Zhang, T. Ohno, Porous cerium dioxide hollow spheres and their photocatalytic performance, RSC Adv., 4 (2014) 62255-62261.

42. H. Yang, B. Xu, S. Yuan, Q. Zhang, M. Zhang, T. Ohno, Synthesis of Y-doped CeO_2/PCN nanocomposited photocatalyst with promoted photoredox performance, Applied Catalysis B: Environmental, 243 (2019) 513-521.

43. S. Yuán, S. Liu, Q. Zhang, M. Zhang, B. Xu, T. Ohno, Effects of the Atmosphere in a Hydrothermal Process on the Morphology and Photocatalytic Activity of Cerium Oxide, ChemCatChem, 10 (2018) 4269-4273.

44. L. Yu, R. Peng, L. Chen, M. Fu, J. Wu, D. Ye, Ag supported on CeO_2 with different morphologies for the catalytic oxidation of HCHO, Chemical Engineering Journal, 334 (2018) 2480-2487.

45. X. Guan, Y. Zhan, L. Yang, J. Lan, J. Shang, S. Chen, W. Li, S. Lin, Durable and recyclable Ag/AgCl/CeO_2 coated cotton fabrics with enhanced visible light photocatalytic performance for degradation of dyes, Cellulose, 27 (2020) 6383-6398.

46. N. Keshvadi, A. Haghighatzadeh, B. Mazinani, Improvement in visible-light-induced photocatalytic activity of Ag–CeO_2 Schottky-type contact heterostructures, Applied Physics A, 126 (2020).

47. A. Krishnan, P.V. Vishwanathan, A.C. Mohan, R. Panchami, S. Viswanath, A.V. Krishnan, Tuning of Photocatalytic Performance of CeO_2-Fe_2O_3 Composite by Sn-doping for the Effective Degradation of Methlene Blue (MB) and Methyl Orange (MO) dyes, Surfaces and Interfaces, 22 (2021).

48. K. Wangkawong, S. Phanichphant, D. Tantraviwat, B. Inceesungvorn, Photocatalytic efficiency improvement of Z-scheme CeO_2/BiOI heterostructure for RHB degradation and benzylamine oxidation under visible light irradiation, Journal of the Taiwan Institute of Chemical Engineers, 108 (2020) 55-63.

49. N. Zhang, S. Liu, X. Fu, Y.-J. Xu, A Simple Strategy for Fabrication of "Plum-Pudding" Type Pd@CeO_2 Semiconductor Nanocomposite as a Visible-Light-Driven Photocatalyst for Selective Oxidation, The Journal of Physical Chemistry C, 115 (2011) 22901-22909.

50. L. Tan, J. Xu, X. Zhang, Z. Hang, Y. Jia, S. Wang, Synthesis of g-C_3N_4 /CeO_2 nanocomposites with improved catalytic activity on the thermal decomposition of ammonium perchlorate, Applied Surface Science, 356 (2015) 447-453.

51. Z. Albu, F. Alzaid, S. AlQahtani, N.A. Abass, F. Alenazey, I. Allehyani, B. AlOtaibi, Improving water oxidation performance by implementing heterointerfaces between ceria and metal-oxide nanoparticles, J Colloid Interface Sci, 587 (2021) 39-46.

52. Y.-C. Zhang, Y.-K. Liu, L. Zhang, X.-t.-f. E, L. Pan, X. Zhang, A. Fazal e, D.-R. Zou, S.-H. Liu, J.-J. Zou, DFT study on water oxidation on nitrogen-doped ceria oxide, Applied Surface Science, 452 (2018) 423-428.

53. T. Feng, J. Ding, H. Li, W. Wang, B. Dong, L. Cao, Amorphous $Fe(OH)_3$ Passivating CeO_2 Nanorods: A Noble-Metal-Free Photocatalyst for Water Oxidation, ChemSusChem, 14 (2021) 3382-3390.

54. S. Mansingh, D. Kandi, K.K. Das, K. Parida, A Mechanistic Approach on Oxygen Vacancy-Engineered CeO_2 Nanosheets Concocts over an Oyster Shell Manifesting Robust Photocatalytic Activity toward Water Oxidation, ACS Omega, 5 (2020) 9789-9805.

55. S. Fang, Y. Xin, L. Ge, C. Han, P. Qiu, L. Wu, Facile synthesis of CeO_2 hollow structures with controllable morphology by template-engaged etching of Cu_2O and their visible light photocatalytic performance, Applied Catalysis B: Environmental, 179 (2015) 458-467.

56. T. Li, X. Wang, Z. Jin, MoC quantum dots modified by CeO_2 dispersed in ultra-thin carbon films for efficient photocatalytic hydrogen evolution, Molecular Catalysis, 513 (2021).

57. A. Hezam, J. Wang, Q.A. Drmosh, P. Karthik, M. Abdullah Bajiri, K. Namratha, M. Zare, T.R. Lakshmeesha, S. Shivanna, C. Cheng, B. Neppolian, K. Byrappa, Rational construction of plasmonic Z-scheme Ag-ZnO-CeO_2 heterostructures for highly enhanced solar photocatalytic H_2 evolution, Applied Surface Science, 541 (2021).

58. W. Zou, Y. Shao, Y. Pu, Y. Luo, J. Sun, K. Ma, C. Tang, F. Gao, L. Dong, Enhanced visible light photocatalytic hydrogen evolution via cubic CeO_2 hybridized g-C_3N_4 composite, Applied Catalysis B: Environmental, 218 (2017) 51-5.

59. J. Liu, L. Zhang, Y. Sun, Y. Luo, Bifunctional Ag-Decorated CeO_2 Nanorods Catalysts for Promoted Photodegradation of Methyl Orange and Photocatalytic Hydrogen Evolution, Nanomaterials (Basel), 11 (2021).

60. A. Hezam, K. Namratha, Q.A. Drmosh, D. Ponnamma, J. Wang, S. Prasad, M. Ahamed, C. Cheng, K. Byrappa, CeO_2 Nanostructures Enriched with Oxygen Vacancies for Photocatalytic CO_2 Reduction, ACS Applied Nano Materials, 3 (2019) 138-148.

61. B. Saif, Q. Gu, P. Yang, The Synthesis of Protein-Encapsulated Ceria Nanorods for Visible-Light Driven Hydrogen Production and Carbon Dioxide Reduction, Small, 17 (2021) e2103422.

62. Q. Zhou, S. Ma, S. Zhan, Superior photocatalytic disinfection effect of Ag-3D ordered mesoporous CeO_2 under visible light, Applied Catalysis B: Environmental, 224 (2018) 27-37.

63. W. Zhao, T. She, J. Zhang, G. Wang, S. Zhang, W. Wei, G. Yang, L. Zhang, D. Xia, Z. Cheng, H. Huang, D.Y.C. Leung, A novel Z-scheme CeO_2/g-C_3N_4 heterojunction photocatalyst for degradation of Bisphenol A and hydrogen evolution and insight of the photocatalysis mechanism, Journal of Materials Science & Technology, 85 (2021) 18-29.

64. G. Murugadoss, J. Ma, X. Ning, M.R. Kumar, Selective metal ions doped CeO_2 nanoparticles for excellent photocatalytic activity under sun light and supercapacitor application, Inorganic Chemistry Communications, 109 (2019) 107577.

65. M.M. Khan, S.A. Ansari, J.H. Lee, M.O. Ansari, J. Lee, M.H. Cho, Electrochemically active biofilm assisted synthesis of Ag@CeO_2 nanocomposites for antimicrobial activity, photocatalysis and photoelectrodes, J Colloid Interface Sci, 431 (2014) 255-263.

Part 2.

Synthesis and mechanism investigation of enhanced photooxidation performance on broom-like (Sm, Y, La and Nd)-doped CeO_2 photocatalysts

Abstract: In this part, CeO_2 displayed a broom-like hierarchical morphology and doped with multiple rare earth (RE) ions, including Sm, Y, La and Nd ions, were successfully synthesized using a template-free hydrothermal method. Comparative tests showed that Sm-doped CeO_2 (SC) has superior photooxidation performance than others, respectively offering around 8.5 times and 3.0 times higher activities of acetaldehyde (CH_3CHO) degradation and bisphenol A (BPA) degradation than those of pure CeO_2. The photooxidation performance of other RE-doped products was also significantly better than that of pure CeO_2. The incorporation of RE ions causes those cations to partially replace the surface-exposed cerium ions, thus increasing the amount of oxygen vacancies (O_v) in RE-doped CeO_2. In order to create a doping-related transition state between the condition band (CB) and valence band (VB), the increased O_v can act as a center for trapping photo-generated electrons. This transition state can effectively lower the rate at which electrons and holes recombine and result in a notable improvement in photooxidation performance. Additionally, extremely reactive superoxide radicals ($\cdot O_2^-$) and hydroxyl radicals ($\cdot OH$) are effective intermediates with strong oxidation capabilities. And they can be produced to boost RE-doped CeO_2's photocatalytic activity even more. This work presents a practical approach for developing multitudinous RE-doped CeO_2-based photocatalysts with improved photooxidation performance.

Keywords: RE-doped CeO_2 • Oxygen vacancies • Transition state • Photocatalytic oxidation performance

2.1 Introduction

Environmental pollution has recently posed a severe threat to human health and ecosystems, mostly because of organic pollutants and hazardous gas wastes produced during industrialization processes [1-3]. Plenty of new photocatalytic materials have been created to remove multi-species contaminants from industrial streams [2-4]. However, there are certain issues with recently produced materials, such as low photochemical stability, a high rate of photogenerated electron and hole recombination, and limited visible light absorption all prevent them from being used as inexpensive semiconductor photocatalysts [2, 3].

One of the most significant rare earth metal oxides is cerium dioxide (CeO_2), which has gained attention for its exceptional qualities, including low toxicity, great chemical stability, safety, and resistance to photo-corrosion [4]. It can be used in many different fields, such as fuel cells, photocatalysts, electrolytes, sensors, and UV blockers [5]. CeO_2 also has photocatalytic characteristics that are comparable to those of TiO_2-based materials, such as a broad band gap (2.9 eV) and potent UV absorption. As a result, it offers a viable candidate for the photocatalytic destruction of harmful organic contaminants. Three typical methods for improving the photocatalytic activity of CeO_2-based materials have been demonstrated in earlier research: shape and size management, doping with different metal ions, and coupling heterojunction [5, 6]. Our research team has successfully created several high-performance CeO_2 photocatalysts with various morphologies and improved activities, such as porous broom-like, hedgehog-like, confeito-like, and hollow octahedral structures [7-9]. The morphology of CeO_2 plays a significant role in its photocatalytic performance. The particular surface area, active sites, and separation of redox crystal facets, which are connected to an enhancement in photocatalytic performance, can be determined by morphology

and size differences.

On the photocatalytic activity investigation of CeO_2, Choudhury investigated the effects of [Ce^{3+}] and oxygen vacancies [10]. The generation of active oxygen vacancies (O_V) is facilitated by the significant deviating stoichiometry of CeO_2, which also facilitates the reduction of cerium ions from tetravalent to trivalent [11-13]. In order to promote the creation of extended crystal-structured CeO_2-based products, which are more useful for electrical transmission, foreign metal ions are added, the effectiveness of pure CeO_2 can also be increased [14]. According to several research, the structure and optical properties of CeO_2 can be altered by the addition of different metal dopant ions as Ca^{2+}, Mn^{4+}, and Fe^{3+} [14, 15]. Additionally, researches have shown that metal ions increased the quantity of trivalent ceria ions and oxygen vacancies in the ceria lattice, which are essential for the photocatalytic oxidation of contaminants [8]. These methods' distinguishing characteristic is a fluctuation in the products' oxygen vacancy concentration, which can serve as electron-capture centers [9]. In turn, this improves the photocatalytic activity at the conclusion of the process by successfully preventing the recombination of electron-hole pairs with the as-formed oxygen vacancies [16-22]. In order to increase the activity of a CeO_2-based photocatalyst, foreign ions can be doped into the catalyst at a reasonable cost. To the best of our knowledge, doping CeO_2 with a variety of various RE ions and systematically analyzing the impacts on photocatalytic performance have not been reported since it is exceedingly difficult to inject diverse ions into the ceria lattice.

In this section, a template-less hydrothermal approach was used to create CeO_2 materials doped with a number of rare earth ions (Sm, Y, La, and Nd) that having a broom-like hierarchical morphology. By conducting studies on the degradation of BPA solution and the on CO_2 release from the CH_3CHO degradation, the photooxidation efficiencies of all the samples were assessed. To

ascertain the impact of doping, the morphology, structure, and photoelectrochemical characteristics were investigated. The photooxidation performance of RE-doped products was much superior than that of pure CeO_2 due to an increase in oxygen vacancies, and comparison investigations revealed that Sm-doped CeO_2 has the highest photooxidation activity. As a result, a photocatalyst doping with the right ions can indeed effectively increase its photocatalytic activity.

2.2 Experimental Sections

2.2.1 Materials

Sodium citrate dihydrate ($C_6H_5O_7Na_3 \cdot 2H_2O$), cerium nitrate hexahydrate ($Ce(NO_3)_3 \cdot 6H_2O$), urea, samarium nitrate hexahydrate ($Sm(NO_3)_3 \cdot 6H_2O$), yttrium nitrate hexahydrate ($Y(NO_3)_3 \cdot 6H_2O$), lanthanum nitrate hexahydrate ($La(NO_3)_3 \cdot 6H_2O$) and neodymium nitrate hexahydrate ($Nd(NO_3)_3 \cdot 6H_2O$) were used. All of the chemical reagents used of analytical quality of 99.9% were commercially accessible, and were utilized directly. The experiments were conducted with deionized water by ourselves in laboratory.

2.2.2 Preparation of different RE ion-doped ceria photocatalysts

Firstly, 140 ml of deionized water was used to dissolve 5.88 g of $C_6H_5O_7Na_3 \cdot 2H_2O$. The solution was then rapidly agitated at room temperature for 10 min. After that, 2.4 g of urea was added, and the mixture was agitated for 30 minutes. For later use, the mixture solution was made ready. Likewise, 20 ml of deionized water was used to dissolve 1.63 g of $Ce(NO_3)_3 \cdot 6H_2O$ and 0.144 g of rare-earth salts ($Sm(NO_3)_3 \cdot 6H_2O$, $Y(NO_3)_3 \cdot 6H_2O$, $La(NO_3)_3 \cdot 6H_2O$, and $Nd(NO_3)_3 \cdot 6H_2O$) during 30 minutes of rapid magnetic stirring. The aforesaid mixture solution was then added and agitated for 30 minutes, until the ceric and other RE salts aqueous solution took on a faint yellow. After that, the combined

solutions were put into a 200 ml Teflon-lined autoclave and heated to 120 °C for 36 hours. A white precipitate was extracted by centrifugation and rinsed with ethanol and deionized water at least three times each after naturally cooling to room temperature. Then, the precursor as made was calcined in air for 4 hours at 500 °C to obtain the final yellow product of RE ion-doped ceria. At last, Sm-doped CeO_2, Y-doped CeO_2, La-doped CeO_2, and Nd-doped CeO_2 samples are simplified as SC, YC, LC, and NC, respectively.

2.2.3 Characterization

On a Bruker-AXS X-ray focus, X-ray diffraction (XRD) was carried out using a Cu Ka radiation source (40 kV/40 mA). An In Via Laser Confocal Raman Spectrometer was used to obtain the Raman spectra. The products' morphology and elemental mapping were examined using FE-SEM (Hitachi, S-4800) and HR-TEM (FEI, Tecnai G^2 F30S-TWIN, 300 KV). A Varian Cary 5000 UV-vis spectrophotometer was used to measure diffuse reflectance spectra (DRS) in the UV-visible range. A Shimadzu KRATOS AXIS-NOVA system was used to perform X-ray photoelectron spectroscopy (XPS) at ambient temperature under 10^{-9} Pa utilizing Al K radiation and the C 1s peak (284.6 eV) as a reference. At room temperature, photoluminescence (PL) spectroscopy measurements were carried out using a fluoro-spectrophotometer (Hitachi F-4500) with an excitation wavelength of 310 nm. A Brucker EPR A200 spectrometer was used to record the electron paramagnetic resonance (EPR) radical signals.

2.2.4 Photocatalytic activity evaluation

2.2.4.1 Bisphenol A (BPA) degradation experiment

A 300 W UV lamp was used to photodegradation aqueous bisphenol A (BPA) pollution at a predetermined temperature of 25 °C and light intensity of 100 mW/cm^2. Before starting the

experiment, 120 mg of photocatalyst and 120.0 ml of BPA solution (20 mg/ml) were added to the reaction flask. After stirring for an hour in the dark, an adsorption-desorption equilibrium was then obtained. 4.0 mL of the suspension reaction liquid was then sporadically drained from the reaction flask while the UV lamp was turned on. Filtering was used to separate the BPA solution from the photocatalyst using two layers of cellulose acetate membrane with a 0.22 μm pore size. With a wavelength of 277 nm used to measure the elution, the BPA content and degradation products were measured using a high-performance liquid chromatograph (HPLC) equipped with a JASCO UVIDEC-100-VI optical detector and an Agilent eclipse XDB-C18 column (4.6×150 mm) with a 25 °C column temperature. Acetonitrile and water were combined together to create the eluent (1/1, v/v). The mobile phase flowed at a rate of 1 ml/min.

2.2.4.2 Acetaldehyde (CH_3CHO) decomposition experiment

Additionally evaluated photooxidation activity involved was the degradation of acetaldehyde (CH_3CHO). A glass dish had 100 mg of photocatalyst material sprinkled across the bottom before being sealed in a Tedlar bag (As One Co., Ltd.). This bag was then filled with 125 cm^3 of synthetic air and 500 ppm of CH_3CHO gas. The above-made bag was then left in a dark, room-temperature environment for 2 h in order to achieve an adsorption-desorption equilibrium. The light source was a light-emitting diode lamp (LED), whose intensity was controlled at 1.0 mW/cm^2, emitting light with a center wavelength of about 365 nm. A gas chromatograph that was online and fitted with OV1 and PLOT-Q columns (Agilent Technologies, 3000A Micro-GC, TCD detector) was used to measure the amount of CO_2 that was produced as a function of the amount of time exposed to radiation.

2.2.5 Active species trapping experiment

Typically, tert-butanol (TBA) was employed as a hydroxyl radical (•OH) scavenger, while 1, 4-

benzoquinone (BQ) was chosen as a superoxide radical ($\bullet O_2^-$) scavenger. Ethylenediaminetetraacetic acid disodium (EDTA-2Na) was chosen as a hole (h^+) scavenger, potassium persulfate (KPS) was used as electron (e^-) scavenger. For comparison's sake, a comparable experiment sans scavenger was also carried out. Using a different scavenger, the photocatalyst was dissolved in 120.0 ml of 20 mg/ml BPA solution (1 mM). Similar to the BPA photodegradation experiment described in experimental section **2.2.4.1**, the following approach was employed

2.2.6 Photoelectrochemical measurement experiment

The following steps was done to prepare a typical working electrode: after being dissolved in 30 mL of acetone, 30 mg of the photocatalyst underwent a 1-hour ultrasonic treatment. Then, to increase its ionic strength, one iodine (10 mg) was added, and the mixture was sonicated for 30 minutes. The mixture was then electroplated using an electrophoresis process with 15 V DC power for 5 min onto a 2×1 cm conductive glass (ITO). In order to create the film electrode, the ITO glass was finally dried at 60 °C for 10 hours. The electrolyte was an aqueous solution of Na_2SO_4 (0.1 M). A 100 mW/cm^2 intensity-controlled Xe arc lamp was used to illuminate the working electrode. Pt served as the counter electrode and Ag/AgCl served as the reference electrode during photoelectrochemical measurements on an electrochemical analyzer (CHI660D, Shanghai, Chenhua). In addition, the light source switch was controlled with the shutter every 20 seconds to test the time-photocurrent response.

2.2.7 DFT model and computational details

Utilizing the CASTEP module from Materials Studio 8.0, density functional theory (DFT) calculations were carried out (Accelrys Inc.-San Diego, USA). Generalized gradient approximation (GGA) and exchange-correlation functional of Perdew-Burke-Ernzerhof were utilized to enhance the bulk crystalline cells and atom positions of both the undoped and doped CeO_2 (PBE). The Monkhorst-

Pack k-point meshes were set to 2×2×5, the kinetic cut-off energy for the plane-wave basis set was set to 470 eV, and the ultrasoft pseudo-potential was used to describe the ion-electron interactions. The limits for energy change, maximum force, maximum stress, and maximum displacement were established at 2.0×10^{-5} eV/atom, 0.03 eV/Å, 0.05 GPa, and 0.001 Å, respectively, for the geometry optimization's convergence criteria. Due to the confined character of the 4f electron, accurate modeling of the electronic structure of rare elements is well-known to be a problem for normal DFT methodologies. Therefore, the DFT architecture should incorporate a configurable Hubbard type correction term: DFT + U. For Ce, Sm, Y, La, and Nd elements, U had a value of 6.0 eV. The super-cells that are used are fluorite cubic 2×2×1 cells with 48 atoms. When a single Ce atom is replaced, the elements Sm, Y, La, and Nd generate dopant concentrations of 6.25 percent.

2.3 Results and Discussion

2.3.1 Morphology characterization

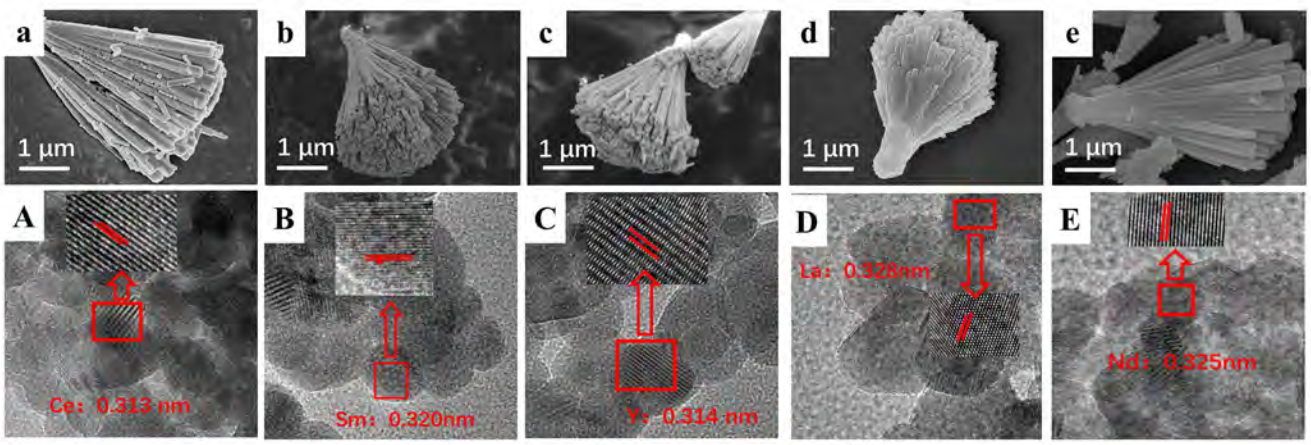

Figure 2-1. FE-SEM and HR-TEM images of (a, A) CeO_2, (b, B) SC, (c, C) YC, (d, D) LC and (e, E) NC samples.

By applying FE-SEM and HR-TEM tests, the morphology of the manufactured samples was examined. The morphology of pure CeO_2 resembles a hierarchical broom-like and with a single root measuring around 20 nm in diameter and 5 μm in length (**Figure 2-1a**). Clear lattice fringes with an

interplanar spacing of 0.313 nm are shown in **Figure 2-1A** and are connected to the CeO_2 (111) crystal plane. The products nevertheless retain the broom-like hierarchical morphology after doping with various RE ions (**Figure 2-1b-e**). However, there are noticeable variations in the nanorods' average diameter and length as well as the degree of surface smoothness. The lattice fringes in the RE-doped products are as follows and have interplanar spacing: SC (0.320 nm), YC (0.314 nm), LC (0.328 nm), and NC (0.325 nm) (**Figure 2-1B-E**). Although the cubic fluorite in ceria still retains its original crystal structure, the shift in lattice spacing implies that the rare earth ions have been successfully incorporated into CeO_2's internal lattice.

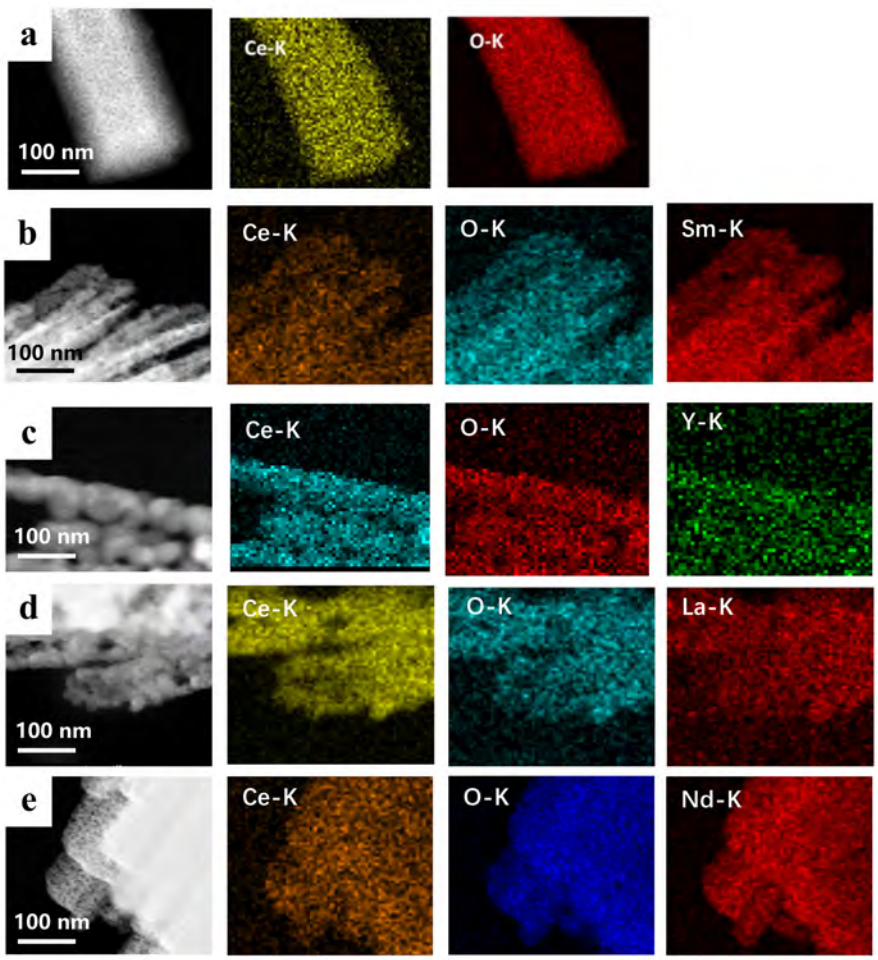

Figure 2-2. HAADF images and distribution of element mapping images: (a) CeO_2, (b) SC, (c) YC, (d) LC and (e) NC samples.

According to EDS mapping findings in **Figure 2-2**, the only elements that can be clearly

distinguished in pure CeO_2 and are evenly dispersed throughout the nanorods are oxygen and cerium. Except for Ce and O, doping elements also exhibit an excellent dispersion on the surface after the addition of RE ions (**Figure 2-2b-e**). According to the aforementioned findings, it is also possible to successfully manufacture photocatalysts doped with RE ions into CeO_2 using template-free hydrothermal treatment.

2.3.2 Structure characterization

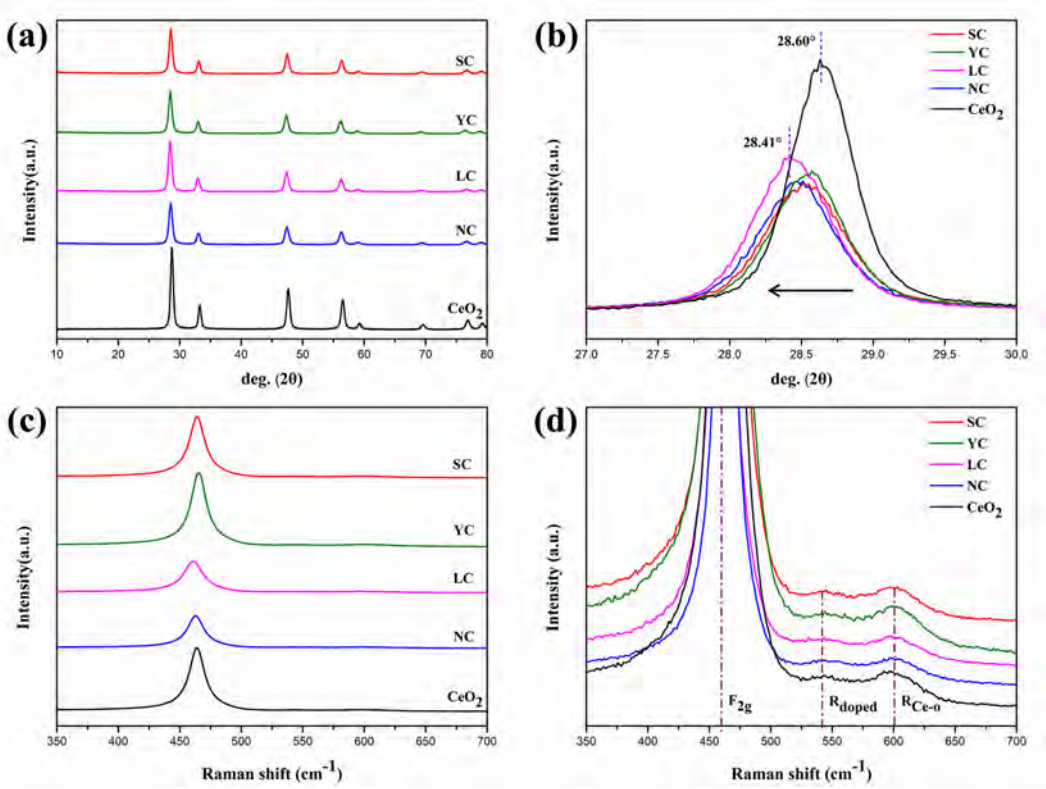

Figure 2-3. Structure characterization: (a) XRD patterns, (b) detailed view of the highest (111) peak patterns, (c) Raman spectra and (d) enlarged view of Raman spectra.

XRD patterns of as-fabricated samples are seen in **Figure 2-3a**. The crystal planes of (111), (200), (220), and (311), respectively, correspond to the typical diffraction peaks of CeO_2 at 28.60°, 33.27°, 47.71°, and 56.51° [22, 23]. The JCPDS card (No. 65-5923) contains standard information that can be used to assign all of the diffraction lines to the phase of ceria with a cubic fluorite structure (space group: Fm-3m (225)). While products lacking impurity peaks demonstrate that doping has no

effect on crystal formation, those with strong diffraction peaks indicate a high degree of crystallinity. The highest (111) peak's expanded XRD patterns (**Figure 2-3b**) show a clear shift to a lower angle following doping when compared to pure CeO_2. The presence of rare earth ions in the crystal structure is clearly responsible for this phenomenon [24]. These findings agree with the variations in lattice fringes seen in HR-TEM images.

Table 2-1. Summary for crystal phase, lattice parameters, calculated grain sizes, R_{wp}, R_p and GOF value from XRD patterns.

Samples	Lattice Parameters (Å)	Calculated Grain size (nm)	R_{wp}	R_p	GOF
SC	5.4182	20.6	5.66	5.75	1.13
YC	5.4190	20.4	5.26	5.48	1.12
LC	5.4219	19.8	7.89	5.39	1.11
NC	5.4211	19.4	7.65	5.25	1.12
CeO_2	5.4114	28.7	4.85	3.73	1.14

Additional Rietveld refinements was done, and **Table 2-1** provides a summary of the results. It is evident that RE-doped samples have lattice parameter values that are higher than those of pure CeO_2 (5.4114 Å). For SC, YC, LC, and NC samples, the values are 5.4182 Å, 5.4290 Å, 5.4219 Å, and 5.4211 Å, respectively. The increased lattice parameters can be attributable to the different rare earth element ions' (Sm^{3+}, Y^{3+}, La^{3+}, and Nd^{3+}) higher ionic radius when compared to Ce^{4+}. The substitution process is more likely to take place on cerium atoms towards the top and border of the crystal than in the body's core in the MO_8 crystal structure of ceria. The crystal lattice of CeO_2 would be significantly expanded after the RE ions have been added to it. It is commonly known that compared to a standard MO_8 crystal structure, an enlarged crystal structure is better for electronic

The detection of two faint Raman peaks at 540 and 600 cm^{-1} is attributed to extrinsic defects brought on by doping (R_{dopant}) and the intrinsic defect vibration of Ce-O (R_{Ce-O}), respectively [27-29]. **Figure 2-3d** depicts the Raman peaks in greater detail. Results from earlier investigations indicate that cerium ions partially exhibit a trivalent state rather than a tetravalent chemical valence in the defect lattice [30]. Surface oxygen would gradually escape from the structure in order to keep the particles in an electrically neutral condition, eventually leading to the creation of inherent oxygen vacancies (O_v) [31]. In the future, greater oxygen vacancies would promote charge carrier separation and slow down the rate of recombination of photo-generated carriers. It can obtain the relative concentrations from **Eq. (1)** and related values determine from the relativity Raman intensity of a of F_{2g}, R_{dopant}, and R_{Ce-O} [30, 31]:

$$\frac{O_V}{F_{2g}}\% = \frac{Aera_{RCe-O}+Aera_{Rdopant}}{Aera_{F_{2g}}} * 100\%, \quad (1)$$

Table 2-2 lists the calculated values in detail. After RE ion doping, the concentration of O_v noticeably rises when compared to pure CeO_2. And the value of O_v rises to a maximum of 12.50% with Sm doping, which is compatible with the findings of the XPS analysis displayed below.

By using XPS spectroscopy, **Figure 2-4a** displays the Ce3d electron core level as well as two group peaks (labeled as v and u) that were attained after deconvolution. The labels of (U, V), (U_2, V_2), and (U_3, V_3), which come from the final states of Ce ($3d^94f^0$) O ($2p^6$), Ce ($3d^94f^1$) O ($2p^5$), and Ce ($3d^94f^2$) O ($2p^4$), respectively, can be classified as Ce $3d_{5/2}$ and Ce $3d_{3/2}$ related to Ce^{4+}, according to past studies[36, 37]. Also, for the Ce 3d bond energy peak, Ce^{3+} can be attributed to two sets of doublets, (U_0, V_0) and (U_1, V_1), and the double lines correspond to Ce ($3d^94f^1$) O ($2p^6$) and Ce ($3d^94f^1$) O ($2p^5$), respectively [36, 37]. The peaks were deconvoluted in order to determine the concentration of Ce^{3+} in the majority of the samples, and **Table 2-2** displays the [Ce^{3+}] concentration of the as-

prepared samples. After RE ions were added, the surface Ce^{3+} ratio clearly increased, and the concentration of SC is 17.69%, which is significantly greater than that of other products. Additionally, these peaks exhibit a doping of ions into the CeO_2 lattice to create a chemical bond, which results in a considerable shift to a lower binding energy (**Figure 2-4b**). It is common knowledge that the existence of Ce^{3+} implies a flaw in CeO_2's lattice, which enables oxygen vacancies to balance out the charge produced by doping [7].

Table 2-2. Calculated [Ce^{3+}], [O_v] and [O_v/F_{2g}] concentrations from XPS and Raman spectra of as-prepared samples.

Samples	[Ce^{3+}]%	[O_v]%	[O_v/F_{2g}]%
SC	17.69	15.25	12.50
YC	16.53	14.81	10.30
LC	15.33	11.89	10.20
NC	14.04	10.64	8.60
CeO_2	1.10	6.73	6.80

Deconvolution of the O1s electron core level revealed three unique forms of oxygen species, identified as lattice oxygen (O_{lat}), oxygen vacancies (O_V), and active surface oxygen (O_{sur}), with binding energies of 528.76, 531.08, and 532.95 eV, respectively (**Figure 2-4c**) [38]. Following the doping of RE ions, these oxygen species' binding energies drastically shift in the direction of lower binding energies. However, the shift phenomenon of O_{lat}, O_V, and O_{sur} shows very diverse outcomes. After Sm doping, the binding energy value of O_v exhibits a shift of 0.33 eV when compared to pure CeO_2. O_{lat} and O_{sur}'s binding energy values only differ by 0.12 eV and 0.20 eV, respectively (**Figure 2-4d**). Therefore, the binding energy of O_v is mostly impacted by RE ion doping. **Table 2-2** shows the O_V ratio after multimodal separation and deconvolution. A similar occurrence shows for [Ce^{3+}],

RE-doped CeO_2 strategy have greater photocatalytic activity [38, 39]. It is noteworthy that [Ce^{3+}] and [O_v] concentrations in SC reach levels of 17.69% and 15.25%, respectively, both much greater than those of other samples.

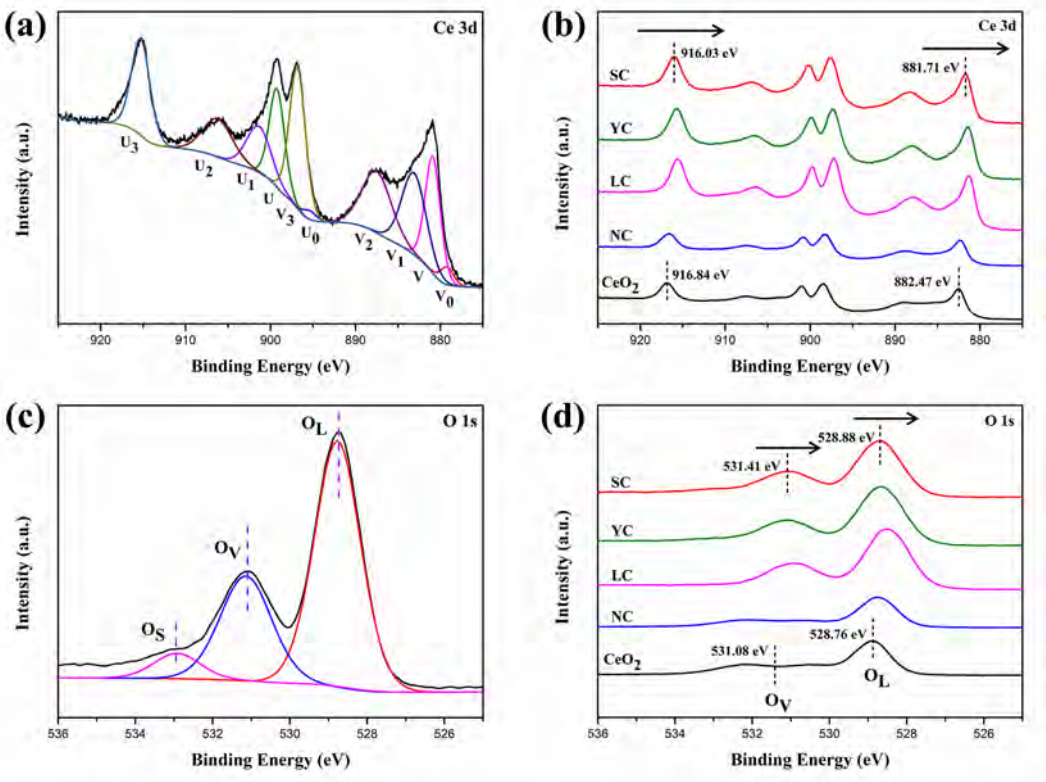

Figure 2-4. Separated peak curves of (a) Ce 3d, (c) O 1s, high-solution XPS spectra of (b) Ce 3d, and (d) O 1s of each product.

2.3.3 Photocatalytic activity analysis

2.3.3.1 Photocatalytic Bisphenol A degradation

First of all, the degradation of aqueous bisphenol A (BPA) was used to assess the photooxidation activities of the products. **Figure 2-5a** shows that under light irradiation for 6 hours, the SC achieves BPA removal rate of 98.76%, which is much higher than that of other samples. The poorest rate constant for BPA degradation activity on pure CeO_2 is a clearance rate of only 34.07%. According to the kinetic equation (**Figure 2-5b**), the rate constant for SC is 0.5145 h^{-1}. Compared to YC, LC, NC,

and pure CeO_2 samples, SC has 1.32, 3.31, 4.31, and 5.30-times more values, respectively.

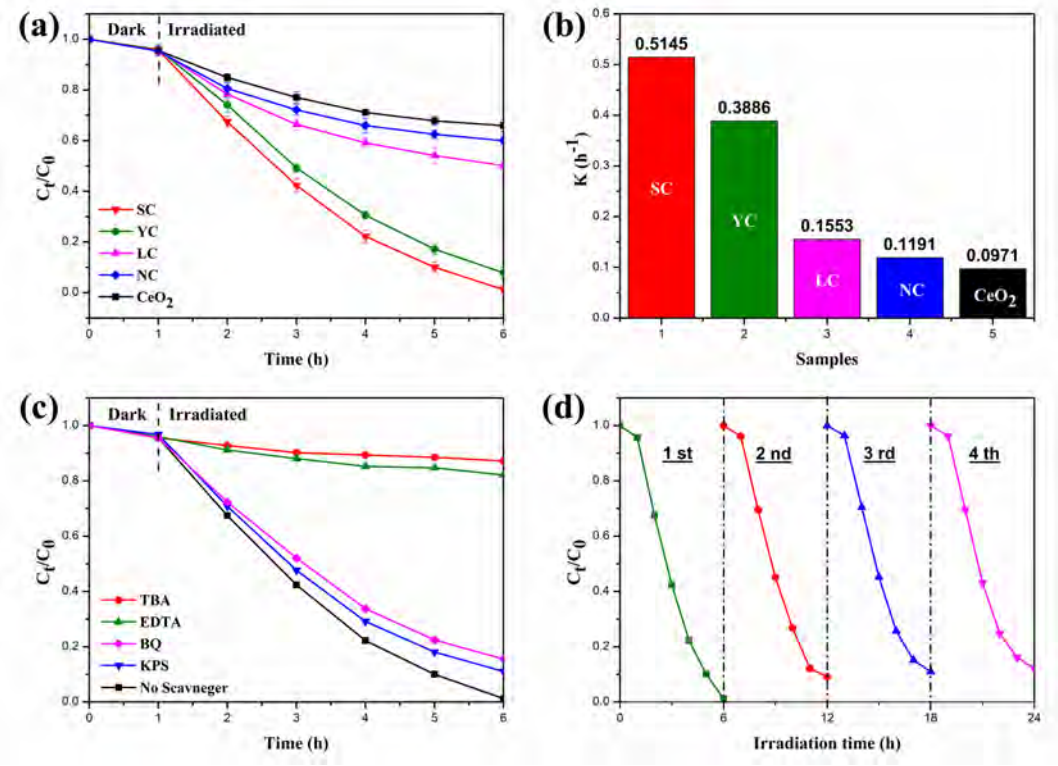

Figure 2-5. (a) BPA photooxidation degradation curves, (b) degradation kinetics constants, (c) degradation efficiency with the addition of scavengers and (d) stability test.

After numerical calculation, the rate constant shows that BPA degradation follows the Langmuir-Hinshelwood rate. Moreover, HPLC was utilized to examine the byproducts of each stage of the BPA photocatalytic degradation process. BPA is primarily responsible for the peak of retention time of 7.74 min, and the intensity of the peak steadily declines throughout the reaction process, showing that BPA is continually destroyed (**Figure 2-6**). After two hours of photodegradation, a new peak corresponding to p-hydroxyacetophenone with a retention time of 4.04 min develops, and the intensity steadily rises. As a result, it ought to be a significant degradation product. Furthermore, phenol has a faint peak at 5.09 min, whose intensity rises as the reaction time increases. According to HPLC analysis, phenol and p-hydroxyacetophenone are the two primary intermediates produced during the degradation of BPA. These by-products could undergo further oxidation and degradation

into final CO_2 and H_2O.

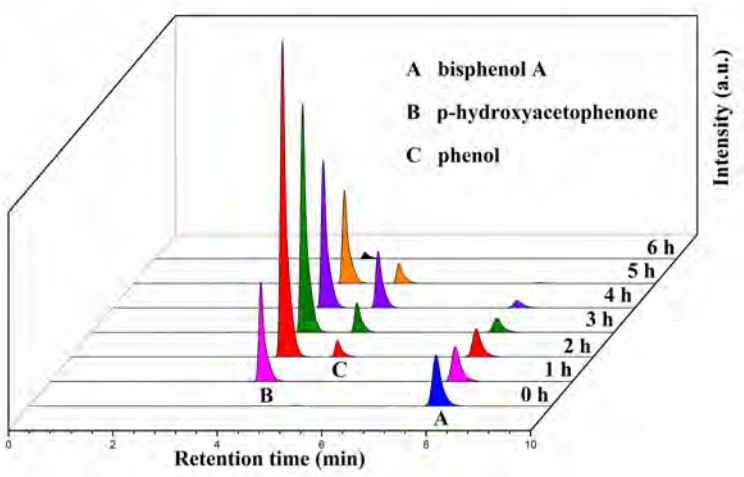

Figure 2-6. Main degradation products of BPA tested by HPLC.

The following reaction mechanisms are therefore proposed:

$$CeO_2 + h\nu \rightarrow CeO_2\ (h^+) + CeO_2\ (e^-) \quad (2)$$

$$OH^- + h^+ \rightarrow \cdot OH \quad (3)$$

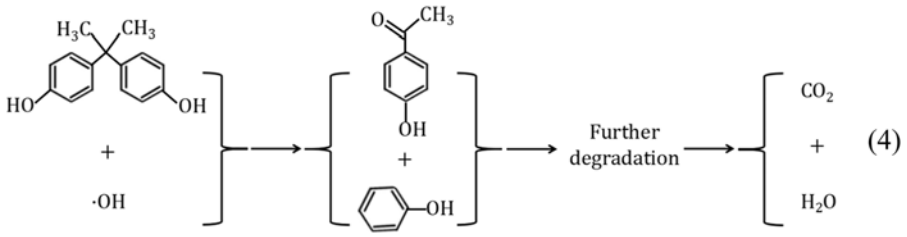

(4)

The BPA degradation pathways have previously been identified, and trapping experiments are required to determine the primary active ingredient in the degradation process [40, 41]. **Figure 2-5c** demonstrates that adding TBA produces a sharp decrease in the photodegradation efficiency of BPA from 98.76% to 12.83%, indicating that ·OH radicals are one of the process' main active species. The degradation efficiency was likewise decreased to 17.87% when EDTA was introduced, showing that h^+ is equally crucial to the photocatalytic oxidation process. However, after the addition of KPS (88.92%) and BQ (84.47%), the degradation efficiency of BPA is slightly decreased. Typically, a chemical has a considerable effect when there is a clear decrease in photocatalytic efficiency [39-41].

Consequently, the results of the active substance capture tests demonstrate that ·OH and h^+ are largely active, but e^- and $\cdot O_2^-$ have relatively little effects on the degradation of BPA in this RE-doped CeO_2 system. The exceptional photocatalytic durability of the SC photocatalyst as-fabricated is further shown by the fact that SC shows no apparent attenuation after four cycles of BPA photooxidation degradation (**Figure 2-5d**). In addition, YC, LC, NC and pure CeO_2 all preserve good reusability in the meanwhile.

2.3.3.2 Photocatalytic acetaldehyde decomposition

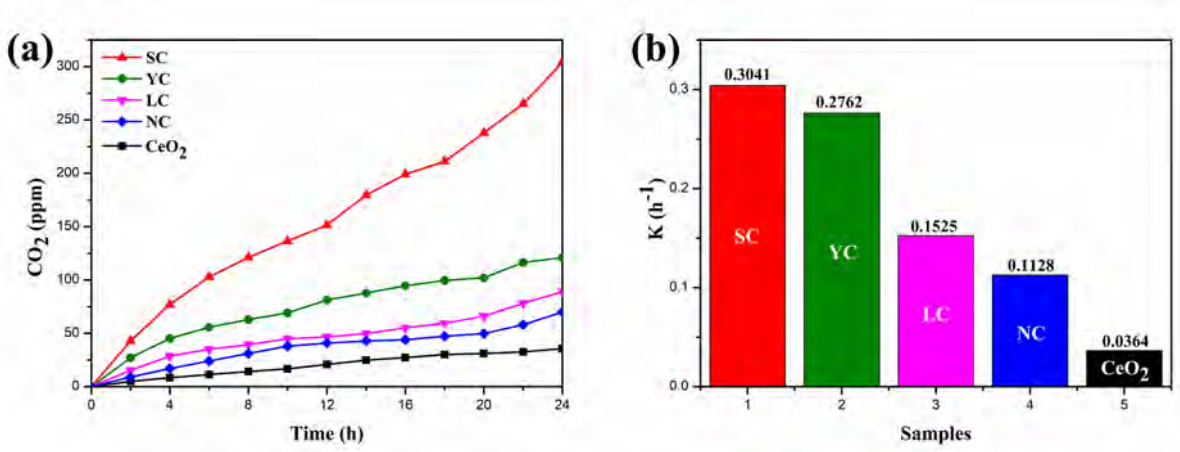

Figure 2-7. (a) Time course of CO_2 liberation from the degradation of CH_3CHO, and (b) kinetics curves for all products.

The photocatalytic degradation of gaseous acetaldehyde (CH_3CHO) by the reaction of $2CH_3CHO + 5O_2 \rightarrow 4CO_2 + 4H_2O$ was further examined to determine the photooxidation activities of the products. After RE ions doping, the photocatalytic activity is significantly increased as compared to pure CeO_2 (**Figure 2-7a**). The maximum CO_2 liberation when Sm doping is present of around 304.05 ppm, which reaches 8.50 times higher than that of pure CeO_2 (35.76 ppm). The excellent photocatalytic activity is attributed to the fact that the concentration of Ov on the surface peaked following Sm doping, as shown by the findings of Raman and XPS examinations. The first-order kinetic equation is what the CH_3CHO degradation process follows, as shown in **Figure 2-7b**.

According to the kinetic equation, the rate constant for SC is 0.3041 h^{-1}, which is significantly higher than the values for YC (0.2762 h^{-1}), LC (0.1525 h^{-1}), NC (0.1128 h^{-1}), and CeO2 (0.0364 h^{-1}). The SC used in this study has substantially higher activity for CH_3CHO oxidation than commercial metal oxide photocatalysts like P25 (21 ppm), S-doped TiO_2 (150 ppm), and WO_3 (200 ppm) [46, 47].

2.3.4 Proposed mechanism

Utilizing UV-vis absorption spectra, further evidence was provided to support the optical impact of dopant ion replacement into the CeO_2 lattice. (**Figure 2-8a**). The band's absorption edge for semiconductors is determined by **Eq. (5)** as follows:

$$(\alpha h\upsilon)^n = B\left(h\upsilon - E_g\right), \tag{5}$$

Where the discrete photon energy is hν, B is the material-related constant, E_g is the absorption bandgap, and α is the absorption coefficient [32], there n are different types of electronic transitions. The value of n is 2 since it has been demonstrated that CeO_2's electronic transition from the valence band to the conduction band is a direct transition [33, 34]. For calculating a semiconductor bandgap, the Schuster-Kubelka-Munk equation is regarded as trustworthy. According to calculations, the band gaps of CeO_2, SC, YC, LC, and NC are 2.87, 2.59, 2.65, 2.74, and 2.79 eV, respectively. The findings also show that CeO_2's band gap can be reduced via rare earth ion doping. The final photocatalytic performance is thought to be largely dependent on the reduced band gap energy (E_g) [48]. Cation doping can encourage the synthesis of trivalent cerium and increase the number of oxygen vacancies (O_v). Additionally, a local energy state that is nearer to the conduction band (CB) might emerge as O_v concentration rises, thus lowering the E_g value [35]. From a VB-XPS spectra, the potential of the valence band (VB) was ascertained. The results clearly showed that the rare earth dopant had been absorbed into the CeO_2 crystal lattice, altering the electrical properties of the RE ions doping products

[32-35].

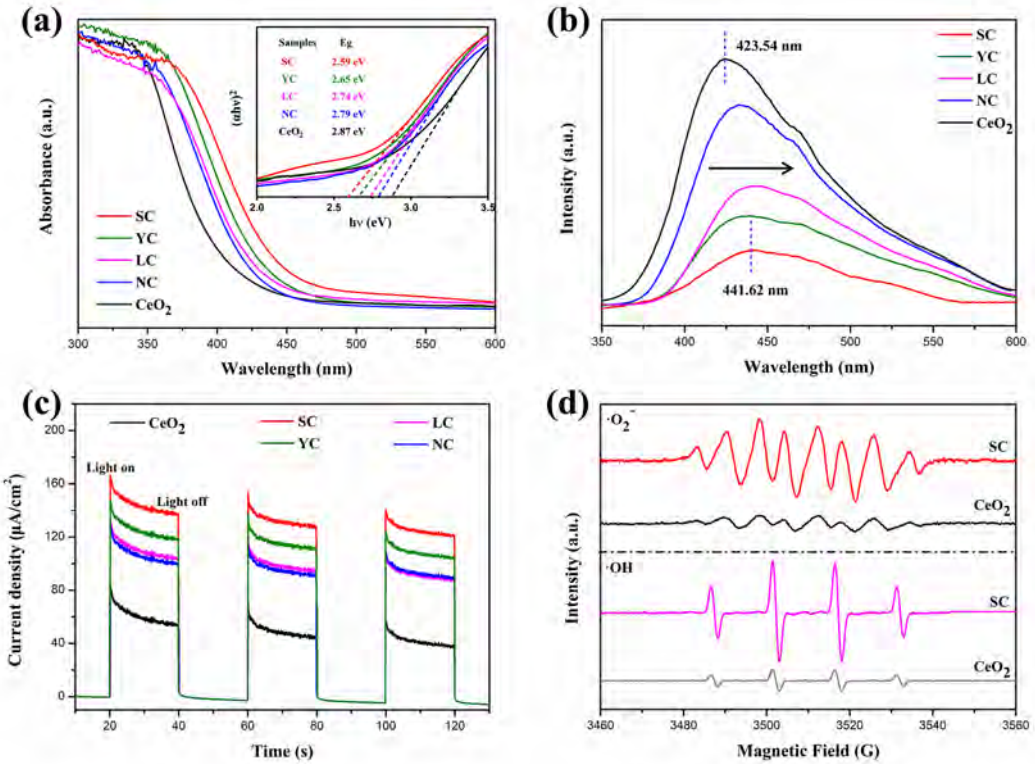

Figure 2-8. Photoelectrochemical characterization: (a) UV-vis diffuse reflectance spectra, (b) PL spectra, (c) transient photocurrent response curves, and (d) EPR spectra.

The rate of recombination of electrons and holes (e^- and h^+) has also frequently been determined using photoluminescence (PL) technologies [44]. A high typical PL peak for pure CeO_2 can be seen at around 423.54 nm, while a lesser peak can be seen at about 441.62 nm (**Figure 2-8b**). Surface defects, which are typically accommodated between the O_{2p} valence band and the Ce_{4f} conduction band, are responsible for both of the two peaks. It is widely known that oxygen vacancies are the main type of surface defects in CeO_2 [45]. The emission spectra of the doped-CeO_2 samples had the same number of peaks. But for CeO_2 doped with various RE ions, the emission band's strength was lessened. And the RE-doped CeO_2 samples with the lowest PL intensity were found in SC. This demonstrates how efficiently promoting the separation of electron pairs and holes can enhance photocatalytic activity [45].

Figure 2-8c displays the results of a photocurrent-time response test used to look at the kinetics

of charge separation at the interface. The photocurrent response curves demonstrate that, when the light source is turned on and off, the photocurrent intensity of all samples abruptly increases and declines respectively, revealing their inherent semiconductor properties [42, 43]. The photocurrent intensities of RE ion-doped samples, such as SC (142.83 μA/cm^2), YC (124.58 μA/cm^2), LC (104.68 μA/cm^2), and NC (109.08 μA/cm^2), are all higher than those of pure CeO_2 (61.21 μA/cm^2). It's noteworthy to notice that SC has a greater maximum photocurrent intensity than pure CeO_2, by a factor of 2.33 times. As the photocurrent intensity increases, it is possible that the charge carriers produced by photons in SC are more successfully segregated than those in other samples. In general, a higher photogenerated electron and hole transfer efficiency translates into a bigger photocurrent intensity, which is favorable for the photocatalytic reactions and leads to improved photocatalytic performance [43].

The key active species were further identified by the EPR data (**Figure 2-8d**). According to the findings, the intensity of ·OH after Sm doping is higher than that of pure CeO_2, which is compatible with the results of the experiments on active species trapping. The resulting ·OH is actually a very powerful intermediate with the capacity to further boost the oxidation photocatalytic activity. As a result, SC can significantly improve photooxidation performance.

The characteristics of the predicted electronic density of states (DOS) are in agreement with earlier DFT + U results, and stoichiometric CeO_2 is known to be an insulator. Additionally, it can be utilized to shed light on changes in electrical structure and light absorption mechanisms. When compared to pure CeO_2, it is clear that the conduction bands of structures with RE ion doping are shifted from a higher energy level to a lower energy level. In the meantime, SC and NC's doping energy level was clearly visible. This suggests that a reduced photo-electron transition energy may result from a smaller band gap. Doping will simultaneously efficiently expand CeO_2's absorption edge

toward the visible light range and control the energy band structure [49]. The energy band structures for fluorite-type pure CeO_2 and RE-doped CeO_2 are presented in **Figure 2-9**. UV-vis observations support similar band gap values, and the energy band topologies of YC and LC are similar to those of pure CeO_2. It was discovered that the new features in the band gaps of SC and NC are caused by the overlap of energy levels between the states of the dopants (Sm and Nd) and the O, which leads to the dopants and O binding. Band structures and band gaps are significantly affected by impurity energy levels, which also increases light yield.

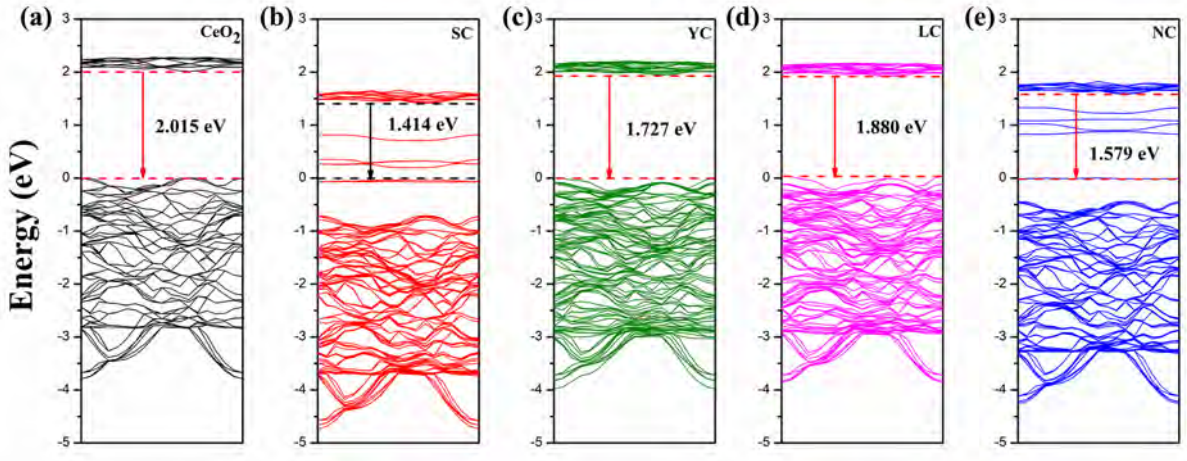

Figure 2-9. Energy band structures of (a) SC, (b) YC, (c) LC, (d) NC, and (e) CeO_2.

Based on the results of photocatalytic assessment studies and the observed characterization data, a feasible reaction mechanism of RE ion-doped CeO_2 is presented (**Figure 2-10**). CeO_2's cubic fluorite structure is susceptible to changes in its crystal structure when RE ions are added. The integration of RE ions causes those cations to partially replace the surface-exposed cerium ions, increasing the lattice's quantity of oxygen vacancies (Ov). By successfully grabbing more electrons on the conduction band (CB), more Ov will be able to slow down the rate of recombination of photogenerated carriers. Additionally, the interaction between holes on the valence band (VB) can efficiently produce a lot of reactive hydroxyl radicals (·OH) on CeO2's surface. The produced ·OH is

a very effective intermediate with the ability to further boost photocatalytic activity, improving the efficiency of photooxidation finally.

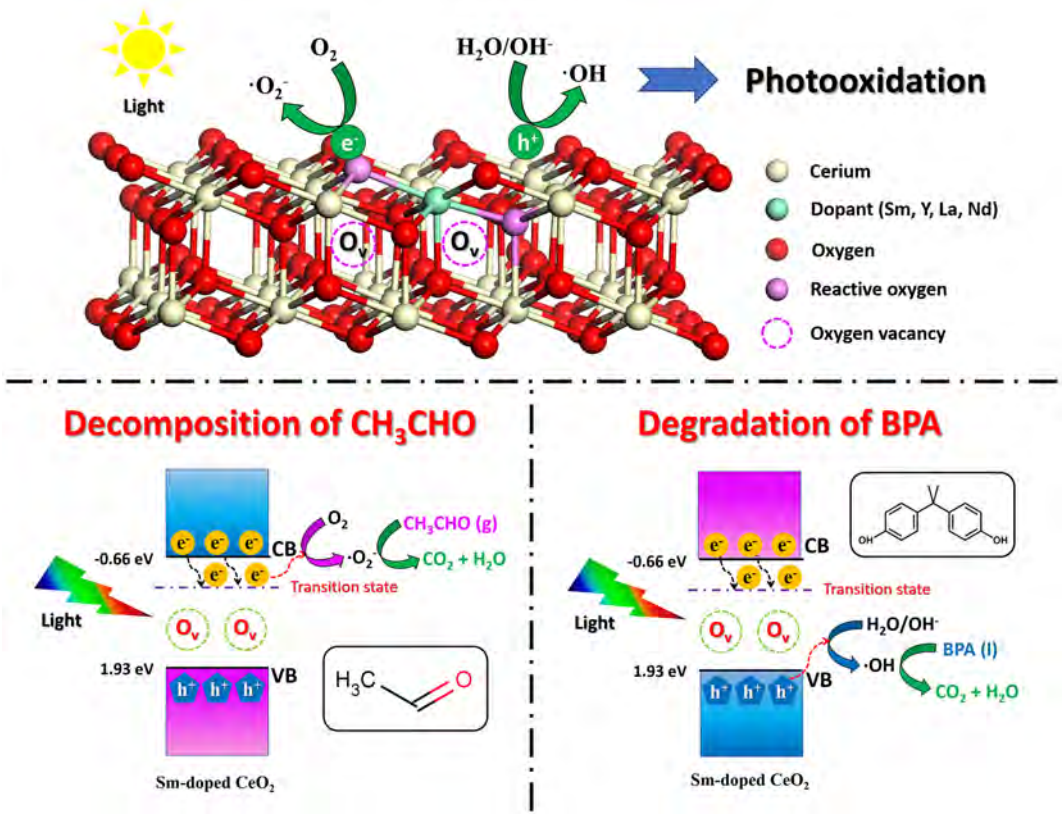

Figure 2-10. A possible mechanism for improving the efficiency of photocatalysis.

We may conclude that SC has the highest photooxidation activity for two main reasons based on the outcomes of experiments on BPA degradation and CH_3CHO degradation. One explanation is because Sm^{3+} and Ce^{4+} have ionic radii that are closer together, which makes it easier for ions to enter the lattice's interior. The other reason is the presence of Sm's two variable valence states of +2 and +3, which each have two oxygen vacancies, serves as a second justification (**Table. 2-3**). In this part, we suggest that the oxygen vacancies (O_v) will act as a transitional state in between the CB and VB. Obviously, O_v in RE ion doping products can also successfully collect photo-generated electrons and limit the recombination of electrons as compared to pure CeO_2.

Table 2-3. Summary of ionic radius of Ce and doping elements with different valence states.

Elements	Ce	Sm		Y	La	Nd	
Valence states	+4	+2	+3	+3	+3	+2	+3
Ionic radius (Å)	0.97	1.27	1.079	1.019	1.16	1.29	1.109

2.4 Conclusions

In conclusion, template-free hydrothermal treatment was successful in producing CeO_2 photocatalysts doped with various RE ions. It is inexpensive to develop and synthesize materials using this approach, and it is easily modified to produce more RE ion-doped inorganic semiconductor materials. FE-SEM and HR-TEM images demonstrated that doped CeO_2 is composed of many nanorods and has a hierarchical morphology like a broom. The doped-CeO_2 has the benefit of having abundant active oxygen vacancies, which are according to Raman and XPS analyses. It was also found that SC exhibits excellent photooxidation performance in comparison to other doped products, offering approximately 3.0-times and 8.5-times greater activity for BPA degradation and CH_3CHO removal, respectively, than those of pure CeO_2 under light irradiation. As a result, our work paves the way for the production of different unique RE ion-doped photocatalysts for environmental friendly remediation applications.

Reference

1. Patel, N., R. Jaiswal, T. Warang, G. Scarduelli, Alpa Dashora, B. L. Ahuja, D. C. Kothari, and A. Miotello. "Efficient Photocatalytic Degradation of Organic Water Pollutants Using V–N-codoped TiO_2 Thin Films." Applied Catalysis B: Environmental 150-151 (2014): 74-81. https://dx.doi.org/10.1016/j.apcatb.2013.11.033.
2. Wang, Yuan, Hamidreza Arandiyan, Jason Scott, Ali Bagheri, Hongxing Dai, and Rose Amal. "Recent Advances in Ordered Meso/Macroporous Metal Oxides for Heterogeneous Catalysis: A

Review." Journal of Materials Chemistry A 5, no. 19 (2017): 8825-46. https://dx.doi.org/10.1039/c6ta10896b.

3. Xu, Haomiao, Zan Qu, Chenxi Zong, Wenjun Huang, Fuquan Quan, and Naiqiang Yan. "MnO_x/Graphene for the Catalytic Oxidation and Adsorption of Elemental Mercury." Environ Sci Technol 49, no. 11 (Jun 2 2015): 6823-30. https://dx.doi.org/10.1021/es505978n.

4. Kim, Hyung Jun, Geonhee Lee, Myeong Gon Jang, Kyung-Jong Noh, and Jeong Woo Han. "Rational Design of Transition Metal Co-Doped Ceria Catalysts for Low-Temperature CO Oxidation." ChemCatChem 11 (2019): 2288–96. https://dx.doi.org/10.1002/cctc.201600xx.

5. Gnanamani, Muthu Kumaran, Gary Jacobs, Wilson D. Shafer, and Burtron H. Davis. "Dehydration of 2-octanol over Ca-Doped CeO_2 catalysts." ChemCatChem 9, no. 3 (2017): 492-98. https://dx.doi.org/10.1002/cctc.201601076.

6. Chen, Beibei, Xiaomin Li, Ruijin Zheng, Ruiping Chen, and Xuan Sun. "Bimetallic (Au–Cu Core)@(Ceria Shell) Nanotubes for Photocatalytic Oxidation of Benzyl Alcohol: Improved Reactivity by Cu." Journal of Materials Chemistry A 5, no. 26 (2017): 13382-91. https://dx.doi.org/10.1039/c7ta02047c.

7. Yuán, Sàisài, Sixiao Liu, Qitao Zhang, Ming Zhang, Bin Xu, and Teruhisa Ohno. "Effects of the Atmosphere in a Hydrothermal Process on the Morphology and Photocatalytic Activity of Cerium Oxide." ChemCatChem 10, no. 19 (2018): 4269-73. https://dx.doi.org/10.1002/cctc.201800659.

8. Yuan, Saisai, Qitao Zhang, Bin Xu, Zhengyuan Jin, Ya Zhang, Yin Yang, Ming Zhang, and Teruhisa Ohno. "Porous Cerium Dioxide Hollow Spheres and Their Photocatalytic Performance." RSC Adv. 4, no. 107 (2014): 62255-61. https://dx.doi.org/10.1039/c4ra12127a.

9. Xu, Bin, Qitao Zhang, Saisai Yuan, Ming Zhang, and Teruhisa Ohno. "Morphology Control and Characterization of Broom-Like Porous CeO_2." Chemical Engineering Journal 260 (2015): 126-32. https://dx.doi.org/10.1016/j.cej.2014.09.001.

10. Choudhury, Biswajit, Pawan Chetri, and Amarjyoti Choudhury. "Oxygen Defects and Formation of Ce^{3+} Affecting the Photocatalytic Performance of CeO_2nanoparticles." RSC Adv. 4, no. 9 (2014): 4663-71. https://dx.doi.org/10.1039/c3ra44603d

11. Huang, Yongchao, Yirui Lu, Ying Lin, Yanchao Mao, Gangfeng Ouyang, Hong Liu, Shanqing Zhang, and Yexiang Tong. "Cerium-Based Hybrid Nanorods for Synergetic Photo-Thermocatalytic Degradation of Organic Pollutants." Journal of Materials Chemistry A 6, no. 48 (2018): 24740-47. https://dx.doi.org/10.1039/c8ta06565a.

12. Mandal, Bappaditya, Aparna Mondal, Sirsendu Sekhar Ray, and Amar Kundu. "Sm Doped Mesoporous CeO_2 Nanocrystals: Aqueous Solution-Based Surfactant Assisted Low Temperature Synthesis, Characterization and Their Improved Autocatalytic Activity." Dalton Trans 45, no. 4 (Jan 28 2016): 1679-92. https://dx.doi.org/10.1039/c5dt03688g

13. Dvořák, F., O. Stetsovych, M. Steger, E. Cherradi, I. Matolínová, N. Tsud, M. Škoda, T. Skála, J. Mysliveček, and V. Matolín. "Adjusting Morphology and Surface Reduction of CeO_2 (111) Thin Films on Cu(111)." The Journal of Physical Chemistry C 115, no. 15 (2011): 7496-503. https://dx.doi.org/10.1021/jp1121646.

14. Qian, Li-Wu, Xin Wang, and He-Gen Zheng. "Controlled Synthesis of Three-Fold Dendrites of $Ce(OH)CO_3$ with Multilayer Caltrop and Their Thermal Conversion to CeO_2." Crystal Growth & Design 12, no. 1 (2011): 271-80. https://dx.doi.org/10.1021/cg201040c.

15. Channei, D., B. Inceesungvorn, N. Wetchakun, S. Ukritnukun, A. Nattestad, J. Chen, and S. Phanichphant. "Photocatalytic Degradation of Methyl Orange by CeO_2 and Fe-Doped CeO_2 Films under Visible Light Irradiation." Sci Rep 4 (Aug 29 2014): 5757. https://dx.doi.org/10.1038/srep05757.

16. Huang, Yongchao, Bei Long, Minni Tang, Zebao Rui, Muhammad-Sadeeq Balogun, Yexiang Tong, and Hongbing Ji. "Bifunctional Catalytic Material: An Ultrastable and High-Performance Surface Defect CeO_2 Nanosheets for Formaldehyde Thermal Oxidation and Photocatalytic Oxidation." Applied Catalysis B: Environmental 181 (2016): 779-87. https://dx.doi.org/10.1016/j.apcatb.2015.08.047.

17. Zhou, Xia, Jun Ling, Weilin Sun, and Zhiquan Shen. "Fabrication of Homogeneously Cu^{2+}/La^{3+}-doped CeO_2 nanosheets and Their Application in CO Oxidation." Journal of Materials Chemistry A 5, no. 20 (2017): 9717-22. https://dx.doi.org/10.1039/c7ta00924k.

18. Truffault, Laurianne, Minh-Tri Ta, Thierry Devers, Konstantin Konstantinov, Valérie Harel, Cyriaque Simmonard, Caroline Andreazza, Ivan P. Nevirkovets, Alain Pineau, Olivier Veron, and Jean-Philippe Blondeau. "Application of Nanostructured Ca Doped CeO_2 for Ultraviolet Filtration." Materials Research Bulletin 45, no. 5 (2010): 527-35. https://dx.doi.org/10.1016/j.materresbull.2010.02.008.

19. Saranya, Jayapalan, Kugalur Shanmugam Ranjith, Padmanaban Saravanan, Devanesan Mangalaraj, and Ramasamy Thangavelu Rajendra Kumar. "Cobalt-doped Cerium Oxide Nanoparticles: Enhanced Photocatalytic Activity under UV and Visible Light Irradiation." Materials Science in Semiconductor Processing 26 (2014): 218-24. https://dx.doi.org/10.1016/j.mssp.2014.03.054.

20. Siriwong, C., N. Wetchakun, B. Inceesungvorn, D. Channei, T. Samerjai, and S. Phanichphant. "Doped-Metal Oxide Nanoparticles for Use as Photocatalysts." Progress in Crystal Growth and Characterization of Materials 58, no. 2-3 (2012): 145-63. https://dx.doi.org/10.1016/j.pcrysgrow.2012.02.004.

21. Jampaiah, Deshetti, Katie M. Tur, Samuel J. Ippolito, Ylias M. Sabri, James Tardio, Suresh K. Bhargava, and Benjaram M. Reddy. "Structural Characterization and Catalytic Evaluation of Transition and Rare Earth Metal Doped Ceria-Based Solid Solutions for Elemental Mercury Oxidation." Rsc Advances 3, no. 31 (2013). https://dx.doi.org/10.1039/c3ra41441h.

22. Sasmaz, Erdem, Chao Wang, Michael J. Lance, and Jochen Lauterbach. "In Situ Spectroscopic Investigation of a Pd Local Structure over Pd/CeO_2 and Pd/MnO_x-CeO_2 During CO Oxidation." Journal of Materials Chemistry A 5, no. 25 (2017): 12998-3008. https://dx.doi.org/10.1039/c7ta00696a.

23. Wang, W. L, W. Y. Liu, X. L. Weng, Y. Shang, J. J. Chen, Z. G. Chen, and Z. B. Wu. "Organic-Free Synthesis and Ortho-Reaction of Monodisperse Ni Incorporated CeO_2 Nanocatalysts." Journal of Materials Chemistry A 6, no. 3 (2018): 866-70. https://dx.doi.org/10.1039/c7ta08872h.

24. Zhang, Xiaodong, Xiao Xie, Hui Wang, Jiajia Zhang, Bicai Pan, and Yi Xie. "Enhanced

Photoresponsive Ultrathin Graphitic-Phase C3n4 Nanosheets for Bioimaging." J Am Chem Soc 135, no. 1 (Jan 9 2013): 18-21. https://dx.doi.org/10.1021/ja308249k.

25. Lee, Youjin, Guanghui He, Austin J. Akey, Rui Si, Maria Flytzani-Stephanopoulos, and Irving P. Herman. "Raman Analysis of Mode Softening in Nanoparticle $CeO_{2-\delta}$ and Au-$CeO_{2-\delta}$ During CO Oxidation." J Am Chem Soc 133, no. 33 (Aug 24 2011): 12952-5. https://dx.doi.org/10.1021/ja204479j.

26. Chang, Sujie, Mo Li, Qing Hua, Lijuan Zhang, Yunsheng Ma, Bangjiao Ye, and Weixin Huang. "Shape-Dependent Interplay between Oxygen Vacancies and Ag–CeO_2 Interaction in Ag/ CeO_2 Catalysts and Their Influence on the Catalytic Activity." Journal of Catalysis 293 (2012): 195-204. https://dx.doi.org/10.1016/j.jcat.2012.06.025.

27. Dohčević-Mitrovi, Z. D., M. Grujić-Brojčin, M. Šćepanović, Z. V. Popović, S. Bošković, B. Matović, M. Zinkevich, and F. Aldinger. "$Ce_{1-x}Y(Nd)_xO_{2-\delta}$ nanopowders: Potential Materials for Intermediate Temperature Solid Oxide Fuel Cells." Journal of Physics: Condensed Matter 18, no. 33 (2006): S2061-S68. https://dx.doi.org/10.1088/0953-8984/18/33/s22.

28. Tovt, Andrii, Luigi Bagolini, Filip Dvořák, Nguyen-Dung Tran, Mykhailo Vorokhta, Klára Beranová, Viktor Johánek, Matteo Farnesi Camellone, Tomáš Skála, Iva Matolínová, Josef Mysliveček, Stefano Fabris, and Vladimír Matolín. "Ultimate Dispersion of Metallic and Ionic Platinum on Ceria." Journal of Materials Chemistry A 7, no. 21 (2019): 13019-28. https://dx.doi.org/10.1039/c9ta00823c.

29. Ma, Lei, Dingsheng Wang, Junhua Li, Bingyang Bai, Lixin Fu, and Yadong Li. "Ag/CeO_2 Nanospheres: Efficient Catalysts for Formaldehyde Oxidation." Applied Catalysis B: Environmental 148-149 (2014): 36-43. https://dx.doi.org/10.1016/j.apcatb.2013.10.039.

30. Yoon, Minjoong, Mijung Seo, Cheoljin Jeong, Joon Hee Jang, Ki Seok, Jeon. "Synthesis of Liposome-Templated Titania Nanodisks. " Chemistry of Materials 17 (2005): 6069–6079. https://dx.doi.org/10.1021/cm0515855

31. Ma, Rory, M. Jahurul Islam, D. Amaranatha Reddy, and Tae Kyu Kim. "Transformation of CeO_2 into a Mixed Phase CeO_2/Ce_2O_3 Nanohybrid by Liquid Phase Pulsed Laser Ablation for Enhanced Photocatalytic Activity through Z-Scheme Pattern." *Ceramics International* 42, no. 16 (2016): 18495-502. https://dx.doi.org/10.1016/j.ceramint.2016.08.186.

32. Hu, Shichao, Feng Zhou, Lingzhi Wang, and Jinlong Zhang. "Preparation of Cu_2O/CeO_2 Heterojunction Photocatalyst for the Degradation of Acid Orange 7 under Visible Light Irradiation." Catalysis Communications 12, no. 9 (2011): 794-97. https://dx.doi.org/10.1016/j.catcom.2011.01.027.

33. Islam, M. Jahurul, D. Amaranatha Reddy, Jiha Choi, and Tae Kyu Kim. "Surface Oxygen Vacancy Assisted Electron Transfer and Shuttling for Enhanced Photocatalytic Activity of a Z-Scheme CeO_2–Agi Nanocomposite." Rsc Advances 6, no. 23 (2016): 19341-50. https://dx.doi.org/10.1039/c5ra27533d.

34. Huang, Ze'ai, Qiong Sun, Kangle Lv, Zehui Zhang, Mei Li, and Bing Li. "Effect of Contact Interface between TiO_2 and g-C_3N_4 on the Photoreactivity of g-C_3N_4/ TiO_2 Photocatalyst: (001) Vs (101) Facets of Tio2." Applied Catalysis B: Environmental 164 (2015): 420-27. https://dx.doi.org/10.1016/j.apcatb.2014.09.043.

35. Dumrongrojthanath, Phattharanit, Titipun Thongtem, Anukorn Phuruangrat, and Somchai Thongtem. "Hydrothermal Synthesis of Bi_2WO_6 Hierarchical Flowers with Their Photonic and Photocatalytic Properties." Superlattices and Microstructures 54 (2013): 71-77. https://dx.doi.org/10.1016/j.spmi.2012.11.001.

36. Deng, Fang, Yin Liu, Xubiao Luo, Dezhi Chen, Shaolin Wu, and Shenglian Luo. "Enhanced Photocatalytic Activity of Bi_2WO_6/TiO_2 Nanotube Array Composite under Visible Light Irradiation." Separation and Purification Technology 120 (2013): 156-61. https://dx.doi.org/10.1016/j.seppur.2013.09.032.

37. Kondo, Kentaro, Naoya Murakami, Chen Ye, Toshiki Tsubota, and Teruhisa Ohno. "Development of Highly Efficient Sulfur-Doped TiO_2 Photocatalysts Hybridized with Graphitic Carbon Nitride." Applied Catalysis B: Environmental 142-143 (2013): 362-67.

    https://dx.doi.org/10.1016/j.apcatb.2013.05.042.

38. Jina, Zhengyuan, Naoya Murakamia, Toshiki Tsubotaa, and Teruhisa Ohno. "Complete Oxidation of Acetaldehyde over a Composite Photocatalyst of Graphitic Carbon Nitride and Tungsten(VI) Oxide under Visible-Light Irradiation." Applied Catalysis B: Environmental 150-151 (2014): 479-85. https://dx.doi.org/10.1016/j.apcatb.2013.12.048.

39. Patsalas, P., S. Logothetidis, L. Sygellou, and S. Kennou. "Structure-Dependent Electronic Properties of Nanocrystalline Cerium Oxide Films." Physical Review B 68, no. 3 (2003). https://dx.doi.org/10.1103/PhysRevB.68.035104.

40. Jampaiah, Deshetti, Samuel J. Ippolito, Ylias M. Sabri, Benjaram M. Reddy, and Suresh K. Bhargava. "Highly Efficient Nanosized Mn and Fe Codoped Ceria-Based Solid Solutions for Elemental Mercury Removal at Low Flue Gas Temperatures." Catalysis Science & Technology 5, no. 5 (2015): 2913-24. https://dx.doi.org/10.1039/c5cy00231a.

41. Hu, Shichao, Feng Zhou, Lingzhi Wang, and Jinlong Zhang. "Preparation of Cu_2O/CeO_2 Heterojunction Photocatalyst for the Degradation of Acid Orange 7 under Visible Light Irradiation." Catalysis Communications 12, no. 9 (2011): 794-97. https://dx.doi.org/10.1016/j.catcom.2011.01.027.

42. Yang, Hui, Bin Xu, Saisai Yuan, Qitao Zhang, Ming Zhang, and Teruhisa Ohno. "Synthesis of Y-Doped CeO_2/PCN Nanocomposited Photocatalyst with Promoted Photoredox Performance." Applied Catalysis B: Environmental 243 (2019): 513-21. https://dx.doi.org/10.1016/j.apcatb.2018.10.057.

43. Liu, Wei, Linlin Cao, Weiren Cheng, Yuanjie Cao, Xiaokang Liu, Wei Zhang, Xiaoli Mou, Lili Jin, Xusheng Zheng, Wei Che, Qinghua Liu, Tao Yao, and Shiqiang Wei. "Single-Site Active Cobalt-Based Photocatalyst with a Long Carrier Lifetime for Spontaneous Overall Water Splitting." Angew Chem Int Ed Engl 56, no. 32 (Aug 1 2017): 9312-17. https://dx.doi.org/10.1002/anie.201704358.

44. Tian, Na, Hongwei Huang, Chengyin Liu, Fan Dong, Tierui Zhang, Xin Du, Shixin Yu, and Yihe Zhang. "In Situ co-Pyrolysis Fabrication of $CeO_2/g\text{-}C_3N_4$ n–n Type Heterojunction for Synchronously Promoting Photo-Induced Oxidation and Reduction Properties." Journal of Materials Chemistry A 3, no. 33 (2015): 17120-29. https://dx.doi.org/10.1039/c5ta03669k.

45. Ji, Pengfei, Jinlong Zhang, Feng Chen, and Masakazu Anpo. "Study of Adsorption and Degradation of Acid Orange 7 on the Surface of CeO_2 under Visible Light Irradiation." Applied Catalysis B: Environmental 85, no. 3-4 (2009): 148-54. https://dx.doi.org/10.1016/j.apcatb.2008.07.004.

46. Xue, Yufei, Dong Tian, Dexin Zhang, Chunhua Zeng, Yunchang Fu, Kongzhai Li, Hua Wang, and Yafang Tian. "The Mechanism of Photocatalyst and the Effects of co-Doping CeO_2 on Refractive Index and Reflectivity from DFT Calculation." Computational Materials Science 158 (2019): 197-208. https://dx.doi.org/10.1016/j.commatsci.2018.11.003.

Part 3.

Improving photocatalytic activity of waxberry-like CeO_2 via samarium doping and silver quantum dots anchoring

Abstract: This section performs the development of a waxberry-like CeO_2 photocatalyst via Sm doping and Ag quantum dots (QDs) anchoring (designated ASC) employing with significant visible-light-driven photocatalytic capabilities for multiple reaction processes. For instance, the CH_3CHO removal and H_2 production activities of the as-fabricated ASC were 7.08 and 6.83 times higher than

those of its pure CeO_2 counterpart, respectively. Analysis of the transient photovoltage (TPV), surface photovoltage (SPV), and density functional theory (DFT) calculations provided a thorough explanation of the charge carriers transmission and the possible reaction mechanism. Significantly**,** Sm doping increases the amount of oxygen vacancies (Ov) in CeO_2, which causes the bandgap of the Sm-doped CeO_2 (SC) to become narrower. The generated Ov can efficiently stop photo-excited electrons and holes from recombining by capturing photo-excited electrons and forming a doping-related transition state between the conduction band (CB) and the valence band (VB) when exposed to visible light. Further due to swiftly transferring to the co-catalytic sites of the anchored Ag QDs, these captured electrons can improve the synchronized absorption of visible light. Our research is intended to help in the design of noble metal quantum dot modified metal oxide semiconductors as well as to efficiently ease their applications in other photocatalytic domains.

Keywords: Photocatalytic performance • Sm-doped CeO_2 • Doping-related transition state • Ag quantum dots • Heterogeneous interface

3.1 Introduction

One of the requirements for solar-driven reactions, which are distinct instances of sustainable chemistry, is the creation of inexpensive materials with outstanding sun-trapping and solar energy conversion efficiency [1-3]. As a result, efficient photocatalysts that respond to visible light are in

high demand for efficient photocatalytic processes. Due to the distinctive structural characteristics of CeO_2, characteristics as its strong skeleton, fluorite-like structure, and unique ability to store oxygen through adaptable conversion between the tetravalent and trivalent valence states of cerium [4-7], its photocatalytic applications have attracted increasing interest over the past few decades. CeO_2 with a spherical form has been found to have the highest surface area and best adsorption properties, making it the most beneficial for photocatalytic processes [8-10]. In the past, our lab had produced CeO_2 successfully with a variety of morphologies to enhance its photocatalytic efficacy. CeO_2's exceptionally low visible-light absorption is caused by its huge bandgap, which further obviously limits its potential applications [11, 12].

Numerous techniques have been used to increase the capacity of ceria to absorb visible light, but effective heterogeneous photocatalyst production stands out for its broad light response range, stability, and reusability [13, 14]. Because of the interfacial contact between the active metal species and CeO_2, it has been found that the CeO_2 semiconductor matrix can react to sunlight more strongly when noble metals like Au, Pt, and Pd are added [14, 15]. For instance, Carltonbird et al. and Ye et al. revealed synthetic techniques for the creation of rod-shaped Au/CeO_2 products with better photocatalytic activity under visible light as well as gold/ceria with varied and coordinated morphologies [16, 17]. As a result, it is important to look into the interactions between noble metals and metal oxides for heterostructure photocatalysts [13–19].

Numerous articles have discussed the usage of CeO_2 modified with various noble metals as photocatalysts. Most noble-metal based catalysts, however, are too expensive to be used in real-world applications. Among them, silver (Ag) has many uses because it is non-toxic, economically priced, and stable when compared to the other noble metals [20, 21]. Furthermore, it is remarkable to find that when lit with visible light, Ag manifests the unmistakable localized surface plasmon resonance

(LSPR) phenomenon [22]. To strengthen the interfacial contacts between the noble metals and the metal oxide, activation is necessary during the high-temperature sintering and impregnation steps that are utilized to make metal oxide supported catalysts. The catalytic activity is greatly diminished as a result of the inevitable reunion of the noble metal particles and the oxide support during this high-temperature annealing procedure [23]. Additionally, some of the described hydrothermal techniques involve numerous steps or the addition of dangerous substances. Noble metal quantum dots with incredibly small sizes and homogeneous distribution can be used to anchor to the support under mild reaction conditions and avoid problems. As a result of improved interfacial contacts, this may lead to greater catalytic performance. Additionally, the performance of pure CeO_2 can be significantly enhanced by doping with rare earth (RE) metal ions [24, 25]. Samarium (Sm) is a better choice among the several RE metals because it has bulk ionic conductors that are more similar to cerium in their crystal structure, which is crucial for improving ionic conductivity in doping heterostructures [26]. Creating CeO_2 with larger crystal structures that are simpler for electronic transmission is benefit [27].

Here, a hydrothermal technique without any template was used to create Sm-doped CeO_2 photocatalyst that anchoring by Ag QDs (ASC). This ASC photocatalyst having a waxberry-like shape can provide a large number of active sites for a variety of photocatalytic applications including removing acetaldehyde and bisphenol A from gaseous and aqueous environments, as well as water oxidation to generate hydrogen. Due to the interfacial contacts between Ag and Sm-CeO_2 can be easily changed; it is possible to significantly improve the heterogeneous photocatalytic capabilities. Numerous cutting-edge spectroscopic techniques were used to analyze the morphology, crystal and optical characteristics, as well as the separation mechanism of charge carriers. This work prompts us to develop a successful plan to improve the photocatalytic efficiency of the other heterogeneous CeO_2-based photocatalysts.

3.2 Experimental Details

3.2.1 Synthesis of Ag@Sm-CeO_2 photocatalyst

First of all, an aqueous of ethanol (40 mL), glycol (80 mL), and deionized water (20 mL) was used to dissolve 4.0 mmol of cerium nitrate hexahydrate ($Ce(NO_3)_3 \cdot 6H_2O$, 1.737 g), 0.4 mmol of samarium nitrate hexahydrate ($Sm(NO_3)_3 \cdot 6H_2O$, 0.178 g), and 0.8 mmol polyvinyl pyrrolidone (PVP). The mixture was then stirred for one hour at room temperature. Then 3 wt% silver nitrate ($AgNO_3$, 0.052 g) was added to the solution and stirred for another two hours. The aforementioned mixture was then added to a 200 mL Teflon-lined reaction kettle and heated to 180 °C for 20 hours. The new sediment was collected by centrifugal separation and rinsed with a solution of deionized water and ethanol (1:1, volume ratio) three times, as the temperature naturally dropped. After that, it was dried for 12 hours at 70 °C in the oven to obtain the yellow precursor. The precursors were calcined at 500 °C for four hours to create the finished product, commonly known as silver quantum dots modified samarium-doped CeO_2 (Ag@Sm-CeO_2, ASC).

The as-fabricated pure CeO_2, samarium-doped CeO_2, and silver quantum dot modified CeO_2 materials were also manufactured under the same conditions for comparison investigations. The final products were simply referred to as CeO_2, SC, and AC, respectively.

3.2.2 Characterization

FE-SEM (Hitachi, S-4800) and HR-TEM were used to examine morphology and elemental mapping (FEI, Tecnai G^2 F30S-TWIN, 300 KV). On a Bruker-AXS X-ray focus, X-ray diffraction (XRD) was carried out using a Cu Ka radiation source (40 kV/40 mA). An In Via Laser Confocal The Raman spectra were obtained using a Raman spectrometer. A Shimadzu KRATOS AXIS-NOVA

system was used to perform X-ray photoelectron spectroscopy (XPS) at ambient temperature under 10^{-9} Pa utilizing Al K radiation and the C 1s peak (284.6 eV) as a reference. A Varian Cary 5000 UV-vis spectrophotometer was used to measure diffuse reflectance spectra (DRS) in the UV-visible range. At room temperature, photoluminescence (PL) spectroscopy measurements were carried out using a fluoro-spectrophotometer (Hitachi F-4500) with an excitation wavelength of 290 nm. The as-produced powder samples' time-resolved photoluminescence spectra (TRPL) were captured using a 450 W Xe lamp and a 290 nm nanosecond laser on an Edinburg Instruments FLS920 spectrofluorometer at room temperature. A Brucker EPR A200 spectrometer was used to record the electron paramagnetic resonance (EPR) radical signal. The degradation products were measured using a high-performance liquid chromatograph (HPLC) equipped with a JASCO UVIDEC-100-VI optical detector and an Agilent eclipse XDB-C18 column (4.6 × 150 mm) with a 25 °C column temperature. On equipment that was described in a recent study (*J Colloid Interface Sci.* 2011, 354, 175-180), the TPV and SPV spectrum were conducted.

3.2.3 Photocatalytic activity tests

3.2.3.1 Acetaldehyde decomposition experiment

Decomposition of gaseous acetaldehyde (CH_3CHO) was used to measure the photooxidation activity. A glass dish with a diameter of 3 cm was first filled with 100 mg of photocatalyst powder, and the glass dish was then set inside a polycarbonate reactor (5 × 5 × 5 cm). In the meantime, 0.1 ml of liquid CH_3CHO was artificially pumped into the reactor. The reactor was then left at room temperature in the dark for 2 hours in order to achieve an adsorption-desorption equilibrium. The light source was a light-emitting diode lamp (LED), whose intensity was controlled at 1.0 mW/cm^2, emitting light with a central wavelength of about 445 nm. The temperature of the reaction was

maintained at room temperature. An online gas chromatograph (Fuli, GC9097 Plus, two FID detectors) outfitted with OV1 and PLOT-Q columns was used to monitor the concentration of generated CO_2 as a function of irradiation time.

3.2.3.2 Hydrogen evolution experiment

A bottom-irradiation vessel connected to an all-glass automated on-line trace gas circulation system was used to conduct photocatalytic hydrogen evolution reactions (HER) (Beijing Perfectlight Co. Ltd, Labsolar-6A). 20 mg of the photocatalyst powder was combined with 50 mL of an aqueous solution containing 10 vol% triethanolamine (TEOA) as a sacrificial agent. In the previously described 50 mL reaction solution, H_2PtCl_6 was dissolved to produce the 3 wt% Pt deposition as a reducing co-catalyst, which was then in-situ photo-deposited for an hour. A condensation water circulation system was used to maintain the reaction temperature at or below 15 °C. The light source was a 300 W Xenon lamp source with a 420 nm filter cutoff made by Beijing Perfectlight Co. Ltd. Online gas chromatography was used to measure the amount of produced H_2 (Fuli GC9790 Plus, TCD detector). The system was completely degassed and Ar was added as a carrier gas before the photocatalytic performance could be observed.

3.2.3.3 Bisphenol A photooxidation experiment

The degradation of liquid bisphenol A (BPA) in the GHX-2 photocatalytic reactor using a 250 W Xe lamp with a 100 mW/cm^2 light output and temperature control at 25 °C was also employed to assess the performance of photooxidation. A reaction flask containing 100 mg of photocatalyst and 100 ml of BPA solution (20 mg/L) was then stirred for 1 hour while it was dark to reach an equilibrium between adsorption and desorption. 4 mL of the suspension reaction liquid was then gradually withdrawn from the reaction flask while the Xe lamp was turned on. Filtering was used to separate

the BPA solution from the photocatalyst using two layers of cellulose acetate membrane with a 0.22 μm pore size. With a wavelength of 273 nm, a UV-vis spectrophotometer was used to determine the BPA content. A high-performance liquid chromatograph (HPLC) with a JASCO UVIDEC-100-VI optical detector and an Agilent eclipse XDB-C18 column (4.6 × 150 mm) with a 25 °C column temperature was used to measure the degradation products. Acetonitrile and water were combined together to create the eluent (1/1, v/v). The mobile phase flowed at a rate of 1 ml/min. And 273 nm was used to measure the elution.

3.2.4 Active species trapping experiment

Potassium persulfate (KPS) was used as an electron (e^-) scavenger, tert-butanol (TBA) was employed as a hydroxyl radical (•OH) scavenger, ethylene diamine tetraacetic acid disodium (EDTA-2Na) was chosen as a hole (h^+) scavenger, and 1, 4-benzoquinone (BQ) was chosen as a superoxide radical ($•O_2^-$). A similar experiment was also run without a scavenger for comparison's sake. In the BPA degradation solution, a photocatalyst with a separate scavenger (1 mM) was disseminated. The procedure that comes next is comparable to the BPA degradation experiment that is detailed in experimental section **3.2.3.3**.

3.2.5 Photoelectrochemical measurement

The following was done to prepare a typical working electrode: After being dissolved in 30 mL of acetone, 30 mg of the photocatalyst underwent a 1-hour ultrasonic treatment. Then, to increase its ionic strength, one iodine (10 mg) was added, and the mixture was sonicated for 30 minutes. The next was then electroplated onto a 6 × 1 cm piece of conductive glass using an electrophoresis method and 15 V DC power for 5 minutes (ITO). Finally, the ITO glass was dried for 12 hours at 60 °C to produce

the film electrode. The electrolyte was an aqueous solution of Na_2SO_4 (0.1 mM). The working electrode received illumination from a 420 nm filter cutoff Xenon lamp source (Beijing Perfectlight Co. Ltd., PLS-SXE300D), with a regulated intensity of 100 mW/cm^2. Pt served as the counter electrode and Ag/AgCl served as the reference electrode during photoelectrochemical measurements on an electrochemical analyzer (CHI660D, Shanghai, Chenhua). In addition, the light source switch was controlled with the shutter every 20 seconds to test the time-photocurrent response.

3.2.6 DFT model and computational details

The Vienna ab initio simulation program's implementation of density functional theory (DFT) (VASP), served as the foundation for all theoretical calculations. The bulk models are optimized using the exchange-correlation functional of the Perdew-Burke-Ernzerhof (PBE) functional and the generalized gradient approximation (GGA). The O $2s^2 2p^4$ and Ce $4f^1 5s^2 5p^6 5d^1 6s^2$ electrons are regarded as valence electrons. With cutoff energies of 400 eV, plane-wave basis sets were used to characterize the valence orbitals. The Monkhorst-Pack approach was used to generate the k-point sample with a (2×2×1) mesh. Utilizing the conjugate gradient method (CG), the atomic coordinates are completely loosened. The conditions for force convergence and electronic self-consistent iteration were set to 10^{-4} eV and 0.02 eV/Å, respectively. And 15 Å vacuum gap was chosen. Spin polarization is used in every computation.

For the unit cell Ag@Sm-CeO_2 (space group: Fm-3m), the optimized lattice constants, which are in good agreement with the experimental observation, are: a = b = c = 5.4217 Å. To reduce the image interactions, a supercell of 3×3×1 is constructed. 5.44 at% is the approximate Sm doping concentration, which is also near to the experimental measurement. On the exposed surface of the CeO_2 (111) crystal plane, one Sm atom (pink color) has taken the place of one Ce atom. The crystal

plane of CeO_2 (111) is chosen to make contact with the Ag atoms. In addition, an Ag cluster is constructed using radium 2.8 Å, and thirteen Ag atoms have been observed by HR-TEM images. On the CeO_2 (111)/Ag interface, an Ag-O bond with a length of 2.65 Å and an angle of 92.5° was formed.

The $(2\sqrt{3}\times 3)$ CeO_2 (111) as was selected as our module because it is the surface in the low crystal index surface that is most stable when exposed to bridging oxygen. The thickness of the vacuum layer is changed to 12 Å to prevent z-axis atom interactions. The bottom three layers of atoms are fixed, whereas the top three layers of atoms were relaxed. To illustrate Sm-doped CeO_2, one Sm atom is replaced for a Ce atom on the surface. An Ag cluster is indicated by two Ag atoms. The following equation of **Eq. (1)** defines the adsorption energy:

$$E_{ads}\ (Ha) = E_{adsorbate/slab} - (E_{adsorbate} + E_{slab}) \quad \textbf{(1)}$$

This slab model including an adsorbate has a total energy of $E_{adsorbate/slab}$, $E_{adsorbate}$, and E_{slab}, which are the energies of the isolated adsorbate and slab, respectively. And E_{ads} stands for adsorption energy. CeO_2 that has been doped with Sm is designated as SC, and Ag-loaded slabs are designated as AC and ASC, respectively.

3.3 Results and Discussion

3.3.1 Morphology characterization

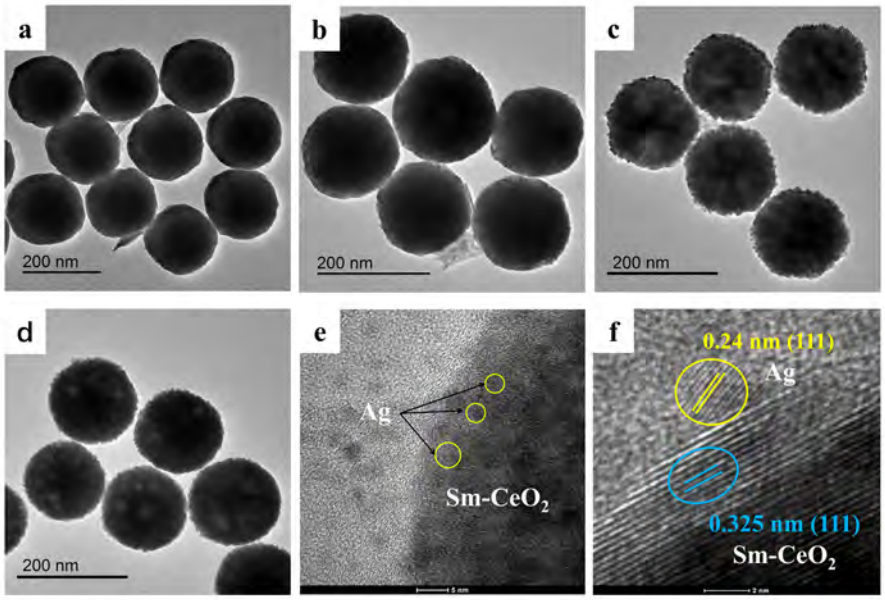

Figure 3-1. TEM images of (a) CeO_2, (b) SC, (c) AC, (d) ASC, (e) HR-TEM images of ASC, and (f) lattice fringe in ASC.

Using HR-TEM and SEM technologies, the morphological data of the prepared photocatalysts was expressed. With a diameter of about 200 nm, smooth microspheres are observed in pure CeO_2 (**Figure 3-1a**). The SC continues to have a comparable diameter and a spherical shape (**Figure 3-1b**). However, the rough waxberry-like shape has undergone a marked alteration in AC and ASC (**Figure 3-1c-d**). The attachment of the Ag QDs (about 2 nm) with a nice distribution on the surface of the SC microspheres is responsible for this phenomenon (**Figure 3-1e**). Lattice fringes of face-centered cubic CeO_2 (111) crystal plane and cubic Ag (111) crystal plane, respectively, with inter-planar lengths of 0.325 nm and 0.240 nm, are clearly discernible in ASC (**Figure 3-1f**). The EDS-mapping images show that the elements Ag, Ce, O, and Sm are present and uniformly dispersed on the waxberry-like ASC microspheres. Most of the photocatalyst in ASC was created using a template-free solvothermal approach, according to the analysis above.

3.3.2 Structural characterization

The XRD patterns were used to determine the samples' as-formed structural information and crystal phase. Both ASC and AC may display the cubic phases of Ag (JCPDS. No. 65-2871) and CeO_2 (JCPDS. No. 43-1002) at the same time (**Figure 3-2a**) [21, 28]. The typical diffraction peaks of silver, which are attributed to its (111), (200), and (220) crystal faces, are situated at 37.99°, 44.18°, and 64.35°, respectively. At the same time, the typical ceria peaks of CeO_2 located at angles of 28.54°, 33.07°, 47.48°, and 56.36°, respectively, correspond to the crystal faces of (111), (200), (220), and (311) [29]. Generally speaking, all of the samples' acuminate diffraction peaks show high levels of crystallinity and purity. It may be inferred that the addition of these samarium ions has no impact on the crystal structure of the doped photocatalysts because the peaks for AC and ASC are comparable.

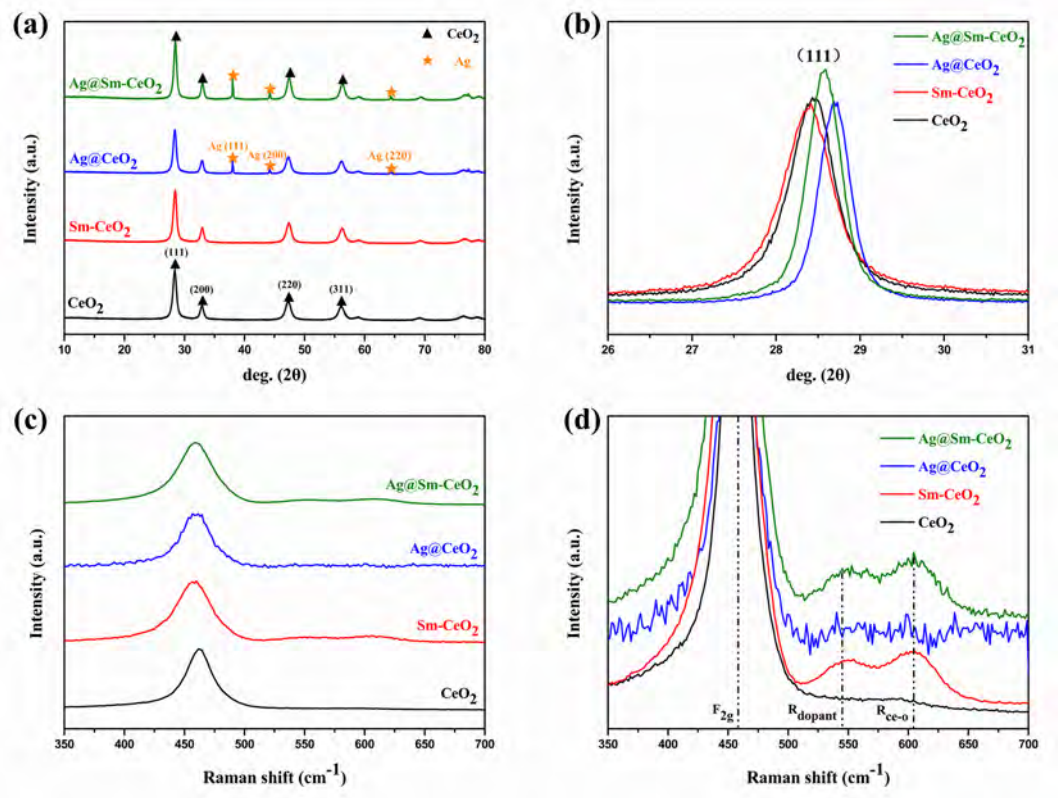

Figure 3-2. (a) XRD patterns, (b) detailed view of the highest (111) peak patterns, (c) Raman spectra and (d) enlarged view of Raman spectra.

In contrast to pure CeO_2, the peak corresponding to the (111) plane in the ASC changes once Sm ions are doped, moving from 28.45° to a lower angle of 28.40° (detail inset in **Figure 3-2b**). This finding shows that the doping of Sm into the SC crystal lattice is what causes lattice expansion [28]. The peak for the (111) peak in the sample ASC, on the other hand, shifts to a greater angle of 28.70° after Ag addition. It indicates that the Ag nanoparticles loaded on the surface of CeO_2 are preventing the CeO_2 crystal seed from growing further, which prevents the crystal lattice in AC from contracting. The center position of (111) peak on ASC sample, which is between CeO_2 (28.45°) and AC (28.70°), can therefore be rationally explained.

Table 3-1. Summary for crystal phase, lattice parametres, calculated grain sizes, R_wp, R_p and GOF of all samples.

Samples	Crystal phase	Lattice parameters (Å)	Calculated grain size (nm)	R_{wp}	R_p	GOF
CeO_2	CeO_2	5.4100	23.7	3.92	3.05	1.15
SC	CeO_2	5.4217	6.7	4.56	3.64	1.26
AC	CeO_2	5.4134	38.5	3.96	3.03	1.12
	Ag	4.0569	4.5	3.96	3.03	1.12
ASC	CeO_2	5.4209	35.4	4.76	3.54	1.37
	Ag	4.1356	5.2	4.76	3.54	1.37

Additionally, Rietveld refinements calculations were performed in order to ascertain the true information about these Sm ions' doping [8, 9, 29]. The lattice parameter (a) of SC is changed to a numerical value of 5.4217 Å compared to pure CeO_2 (5.4100 Å). (**Table 3-1**). A greater value of (a) indicates that Sm was successful in accessing the CeO_2 lattice, which led to the enlargement of the CeO_2 crystal lattice [8, 28]. Additionally, ASC has a smaller lattice parameter (5.4209 Å) than SC,

which has a perfect fit with the results of the aforementioned XRD patterns.

Raman spectra are a useful tool for characterizing structural defects. According to fluorite phase CeO_2, a potent F_{2g} symmetry mode is blamed for an apparent peak at 462 cm^{-1} (**Figure 3-2**). With varying Sm doping concentrations, the two additional faint peaks of 540 cm^{-1} and 600 $cm^{-}1$ were also seen. These two peaks are related to partial Ce-O (R_{Ce-O}) bond symmetry stretch and doping-induced extrinsic oxygen vacancies, respectively [9, 29]. The MO_8 structure of CeO_2 is also well preserved because the position of the F_{2g} peak displays the same Raman shift even with different Ag anchoring concentrations. External oxygen vacancies result from the replacement of some of the cerium atoms with samarium. The relative concentration ratios of (Ov) are calculated from **Eq. (2)**:

$$O_V\% = \frac{\text{Area}[R_{Ce-O}+R_{dopant}]}{\text{Area}(F_{2g})} * 100\%, \qquad \textbf{(2)}$$

Table 3-2 displays the conclusions of the pertinent calculations. The value of (O_v) in ASC reaching 16.89% is substantially greater than in the other samples. This result is also compatible with the results of the XPS O1s study, which is covered below.

Table 3-2. Calculated [Ce^{3+}], [O_S] and [O_V] concentrations from XPS and Raman spectra of as-prepared samples.

Samples	[Ce^{3+}]%	[O_S]%	[O_V]%
CeO_2	20.98	22.25	5.60
SC	24.06	31.16	17.04
AC	24.71	20.65	8.75
ASC	25.22	30.81	16.89

Also by using XPS analysis, it was possible to identify the element interactions, chemical states, and surface makeup of the elements. The survey spectra of the ASC photocatalyst provide evidence of Ce, O, Ag, and Sm, and it is well congruent with the findings from EDX mapping. According to the Gaussian-Lorentzian function, the matching Ce 3d spectra can be deconvoluted and fitted into ten peaks (**Figure 3-3a**). The typical Ce^{4+} peaks in CeO_2 are given the designations of (U, V), (U_2, V_2), and (U_3, V_3) based on the results of the previous investigation. The typical Ce^{3+} peaks can be divided into two groups of U_0, V_0, and U_1, V_1, respectively. **Table 3-2** also included the values obtained from **Eq. (3)**'s corresponding values [9, 30], the quantified values of Ce^{3+} concentration are as follows:

$$\left[Ce^{3+}\right]\% = \frac{\text{Area}[V_0+V_1+U_0+U_1]}{\text{Total Area}} * 100\%, \qquad \textbf{(3)}$$

In addition, in ASC as opposed to other samples, the creation of a heterojunction that affects the electron density of cerium is indicated by a decrease in the binding energy (BE) of Ce 3d. Additionally, the peaks at 528.48 and 531.35 eV that correspond to the BE of the lattice oxygen (O_L) and active surface oxygen (O_S), respectively, can be seen clearly in **Figure 3-3d** [8, 29]. Similar to other samples, the BE of ASC administered to O_L and O_S shifts to a significantly lower value (**Figure 3-3e**). **Table 3-2** lists each type of oxygen ratio after deconvolution and multimodal separation. ASC has Ce^{3+} and O_S concentrations that are remarkably greater than those in other samples, at 25.22% and 30.81%, respectively. It is well-known that the presence of trivalent cerium ions suggests a structural fault in CeO_2 and increases the number of oxygen vacancies (Ov), which enables active surface oxygen to balance out the charges caused by doping. While this is going on, compensated migration has the potential to speed up oxygen diffusion and promote the production of highly reactive radicals, which are capable of efficiently oxidizing organic materials. So, it stands to reason that ASC would have greater photocatalytic activity.

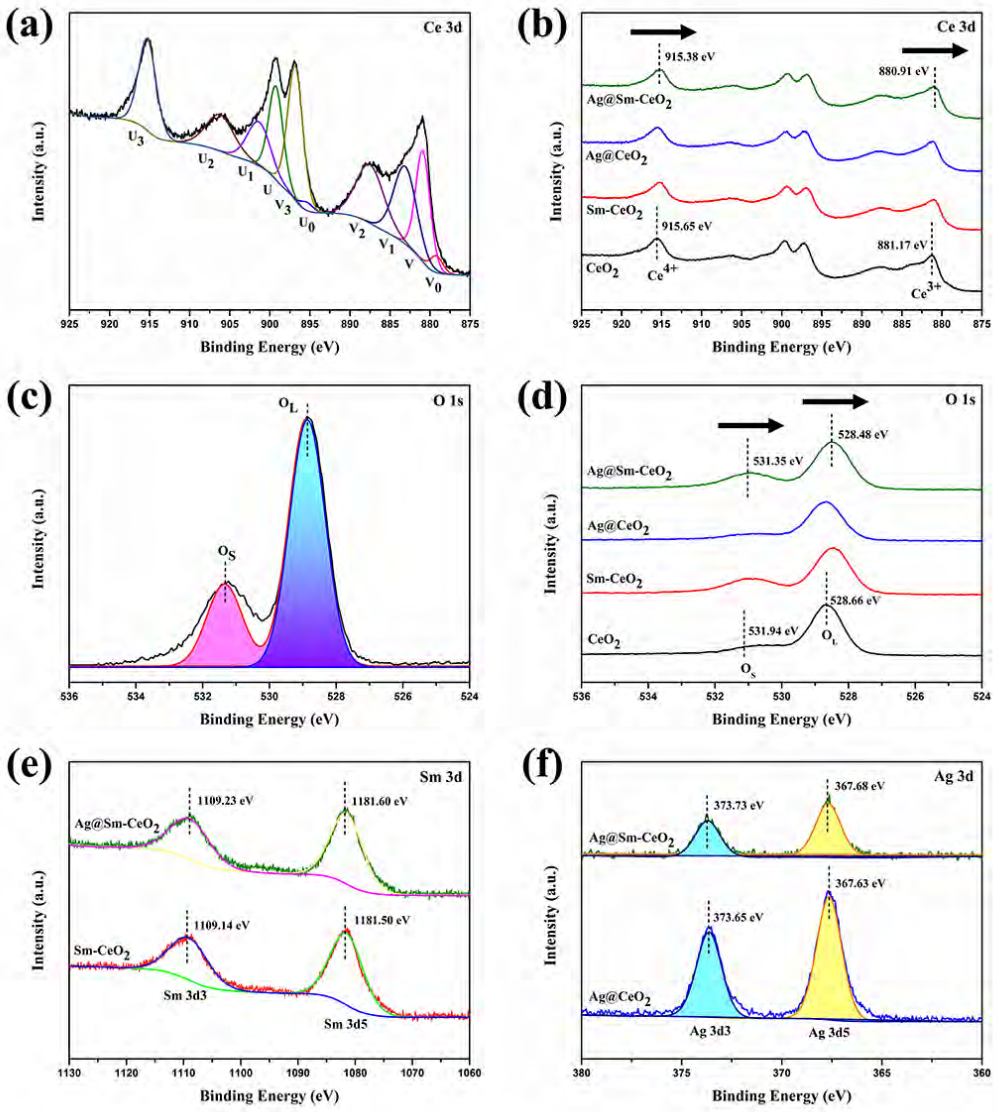

Figure 3-3. Separated peak curves of (a) Ce 3d, (d) O 1s, high-solution XPS spectra of (b) Ce 3d, (c) Ag 3d, (e) O 1s and (d) Sm 3d of each product.

The two ASC peaks at 368.68 eV and 373.73 eV, which are attributed to metallic silver [21, 22], correspond to the BE of silver's $3d_{5/2}$ and $3d_{3/2}$, respectively. **Figure 3-3c** shows the typical high-resolution XPS spectra of Ag 3d. The attachment of the Ag particles to the CeO_2 is responsible for a little shift in the BE when compared to the value of Ag metal (about 368.20 eV). A heterogeneous interface between the Ag QDs and SC emerged, as evidenced by the formation of a new energy level in the ASC. It can demonstrably show that the ASC photocatalyst was successfully synthesized.

Following deconvolution and separation, the BE of Sm 3d5 and Sm 3d3 can be attributed to the two peaks at BE of 1081.60 eV and 1109.23 eV, respectively (**Figure 3-3f**) [28]. A stronger interaction between SC and the Ag QDs is further suggested by the higher BE of Sm in ASC compared to SC.

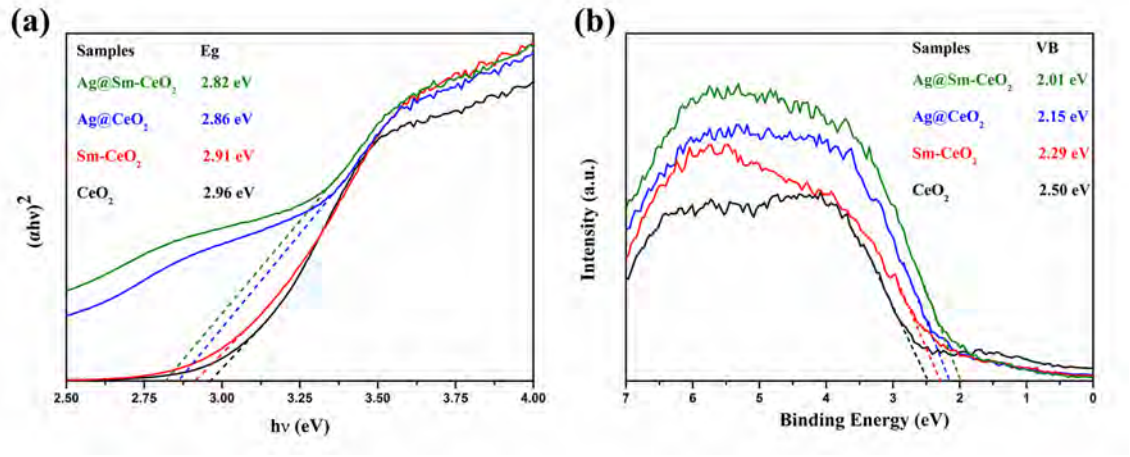

Figure 3-5. (a) Kubelka-Munk spectra, and (b) Valence band XPS spectra of samples.

The optic properties of these items can be verified using UV-Vis diffuse reflectance (DRS) spectra. As depicted in **Figure 3-4a**, the existence of the 438 nm absorption peak in ASC and AC, which is lacking in pure CeO_2 and SC, indicating that the addition of Ag can boost the capacity for response and extend the spectral response range. Additionally, the band's absorption margin for semiconductor photocatalysts is given by **Eq. (4)** [28, 31]:

$$(\alpha h\upsilon)^n = B\,(h\upsilon - E_g), \qquad \textbf{(4)}$$

For CeO_2, SC, AC, and ASC, the estimated bandgap values were 2.96, 2.91, 2.86, and 2.82 eV, respectively (**Figure 3-5a**), showing that the doping of Sm can reduce the bandgap of CeO_2. One of the crucial factors in determining the photocatalytic activity is narrow bandgap energy [9, 32]. Trivalent cerium ions can be produced more readily when Sm ions are doped, which results in more oxygen vacancies (Ov). The more Ov that form, the closer the transition state goes to the CB and the

narrower the bandgap of related products. From their VB-XPS spectra, the potential of the VB was further ascertained (**Figure 3-5b**). These findings demonstrate that noble metal deposition and doping do affect the samples' optical characteristics.

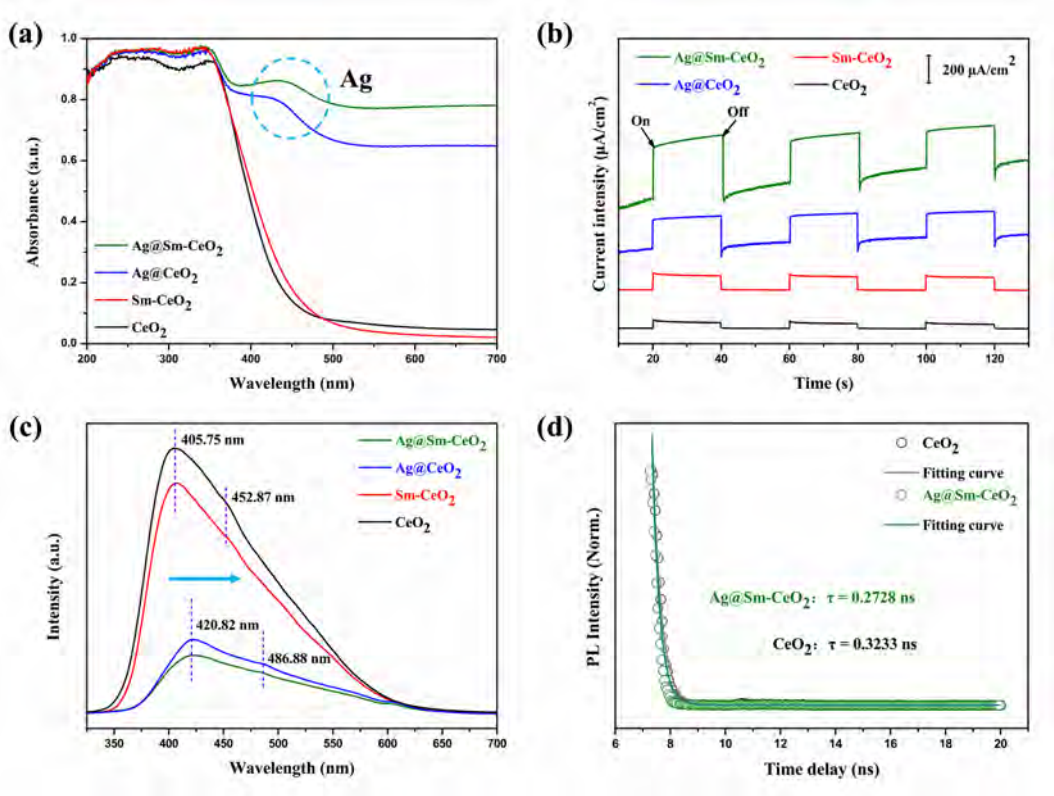

Figure 3-4. (a) UV diffuse reflectance spectra, (b) transient photocurrent response, (c) PL spectra of samples and (d) TRPL spectra of ASC and CeO_2.

The photo-electrochemical response of each sample was measured in order to assess the kinetics of interfacial charge separation. Every product's photocurrent curves sharply changed after the illuminating light was turned on and off, indicating a unique characteristic of semiconductor-typed photocatalysts (**Figure 3-4b**) [8, 33]. Higher photoexcited electron and hole separation efficiency is typically associated with stronger photocurrent intensity. ASC has photocurrent densities of 402.95 $\mu A/cm^2$, which is around 11.23, 4.66, and 1.93-times higher in compared to CeO_2, SC, and AC. The fact that the comparable numerical values are just 35.97, 86.52, and 208.34 $\mu A/cm^2$ is notable. Additionally, compared to other counterparts, the photogenerated carriers are separated considerably

more successfully in ASC, which will result in the production of more separated photoinduced charges during the photocatalytic reaction, enhancing photocatalytic performance.

Analysis of the photoluminescence (PL) spectrum was done to find out how quickly electrons (e^-) and holes (h^+) recombine. A greater peak for the typical photoluminescence emission can be seen in the CeO_2 product at 405.75 nm, while a less intense peak is visible at 452.87 nm (**Figure 3-4c**). The similarities in surface defects between the VB of O_{2p} and the CB of Ce_{4f} [8, 33] may be to blame. The oxygen vacancies are regarded to be the main surface defects in CeO_2. Peak PL spectra locations are identical in the SC sample. However, the emission band's intension is reduced, proving that Sm doping stops the recombination of electron and hole pairs. It is noteworthy that the typical peaks of ASC and AC have a redshift to roughly 420.82 nm and a lesser peak at 486.88 nm, indicating a stronger responsiveness to visible light. Additionally, the lower radiative recombination of the photoexcited carriers (e^- and h^+) is suggested by the lower PL intensity of the AC and ASC, which can significantly improve the photocatalytic performance.

Results from time-resolved photoluminescence (TRPL) lifetime measurements show that the carriers can be extracted by the carrier transport layer. The more powerful the carrier transfer ability, the shorter the TRPL lifetime appears [34]. ASC displays the fastest TRPL decay in accordance with the PL spectra's findings, with a lifetime of 0.2728 ns (**Figure 3-4d**), which is smaller than that of pure CeO_2 (0.3233 ns) and other samples. The reduced exciton population implied by the shorter TRPL lifetime of ASC further implies an enhanced charge separation mechanism and constrains photoinduced electron-hole’s recombination. The TRPL result thus supports the claim that ASC can increase the number of charge trapping sites, which can lead to an increase in photocatalytic activity.

3.3.3 Photocatalytic evaluation

3.3.3.1 Acetaldehyde decomposition ability

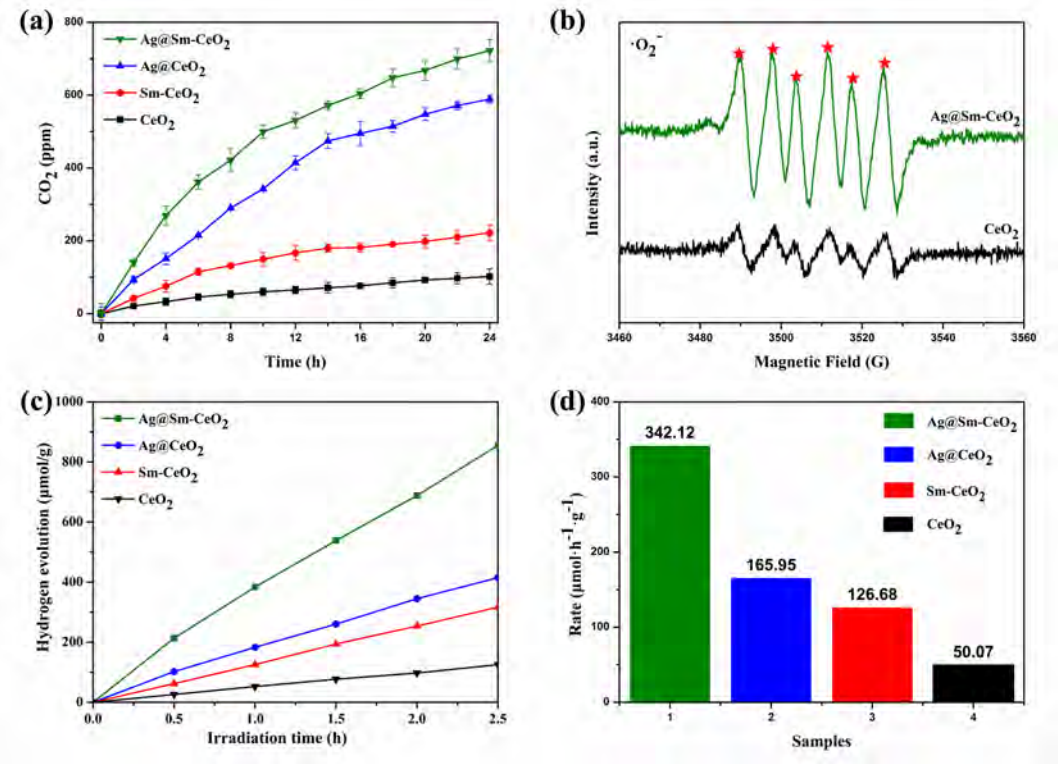

Figure 3-6. (a) Time course of CO_2 liberation from CH_3CHO decomposition and (b) EPR spectra of $\cdot O_2$- in ASC and CeO_2, (c) Time course of H_2 liberation from water splitting and (d) evolution rate curve of samples.

The removal of gaseous CH_3CHO was used to test the photooxidation activity of these photocatalysts, which can be explained by the reaction of **Eq. (5)** of $CH_3CHO + 2O_2 \rightarrow 2CO_2 + 2H_2O$. The amount of released CO_2 for ASC reaches a maximum value of about 722.45 ppm, which is 7.08 times larger than that of the pure CeO_2 (101.96 ppm). This is readily clear from **Figure 3-6a**. Furthermore, ASC greatly improves the amount of CO_2 released compared to SC (221.96 ppm) and AC (589.16 ppm). The principal active component of the investigated photocatalytic material is $\cdot O_2^-$, they are essential for photocatalytic reactions because they serve as extremely effective intermediates. This is further supported by the fact that pure CeO_2 has a weaker EPR intensity than $\cdot O_2^-$ in ASC

(**Figure 3-6b**). Thus, a higher concentration of O_v and active oxygen species can be attributed to the increased photocatalytic activity, and this finding is in line with the results of the Raman and XPS analyses. When compared to commercially available metal oxide photocatalysts like P25 (21 ppm), sulfur-doped TiO_2 (150 ppm), and tungsten oxide (200 ppm), ASC created for this work demonstrates greater CH_3CHO oxidation activity.

3.3.3.2 Hydrogen evolution performance

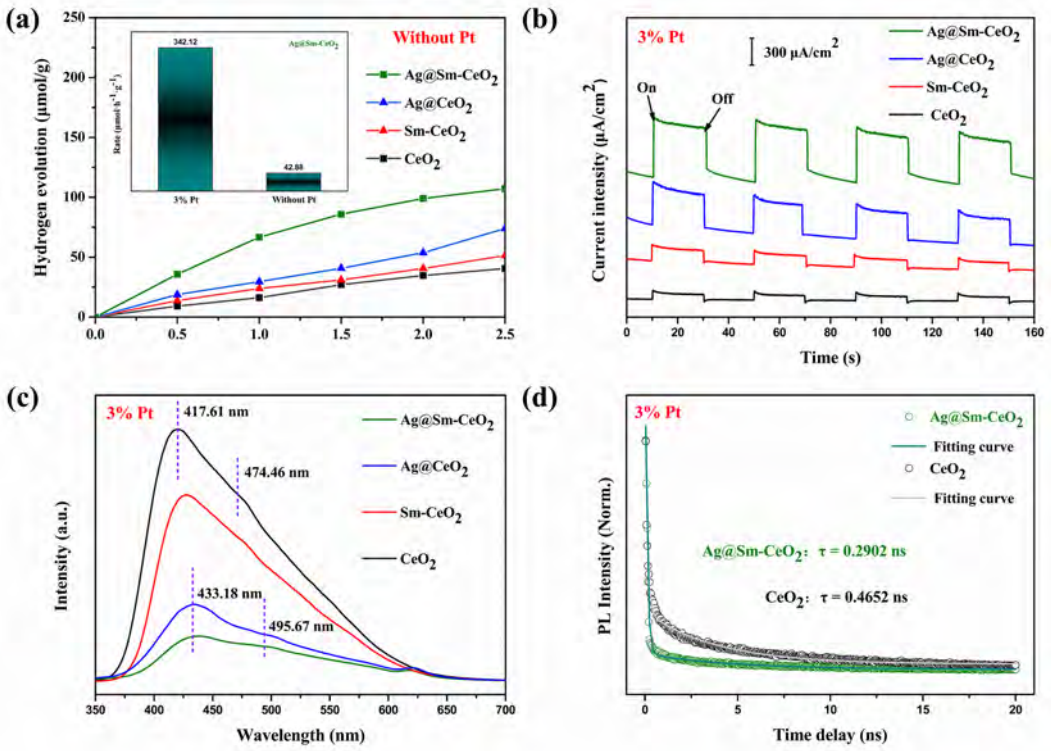

Figure 3-7. (a) PL spectra, (b) TRPL spectra, (c) transient photocurrent response of samples with 3% Pt loading, and (d) time course of H_2 liberation from water splitting without Pt loading.

Furthermore, **Figure 3-6c** depicts the photoreduction activity of the synthesized photocatalysts. The amount of hydrogen (H_2) created by water splitting increases linearly over time for all samples. After 2.5 hours of visible light exposure, the H_2 liberation rate of ASC reaches 342.12 mol•g^{-1}•h^{-1}, which is 6.83 times greater than CeO_2's value (50.07 mol•g^{-1}•h^{-1}) (**Figure 3-6d**). Additionally, the H_2 production rates of SC and AC are 126.68 mol•g^{-1}•h^{-1} and 165.95 mol•g^{-1}•h^{-1}, respectively.

Importantly, ASC is significantly more recyclable than AC, demonstrating that the presence of Sm ions improves the structural stability of the CeO_2 anchored Ag QDs.

In general, it's crucial to describe the products with Pt particles loading using transient photocurrent, PL, and TRPL data in order to confirm the radiative recombination rate of the photogenerated electrons and holes (**Figure 3-7**). The H_2 liberation rate from water splitting without Pt loading of ASC is lower and only achieves 42.88 $mol \bullet g^{-1} \bullet h^{-1}$, despite the fact that the activity of pure CeO_2 with 3% Pt loading is only 50.07 $mol \bullet g^{-1} \bullet h^{-1}$. Therefore, the products with 3% Pt loading must also be characterized. ASC's photocurrent density is 559.62 $\mu A/cm^2$ and is approximately 1.39 times higher than its photocurrent density (402.95 $\mu A/cm^2$) when ASC is not loaded with Pt.

This behavior indicates that photogenerated carriers are separated in ASC significantly more effectively than their counterparts, which will lead to more separated photoinduced charges during the photocatalytic reaction. The value of the other products is also higher than it would have been without the Pt addition. ASC also stands out because it has the lowest PL intensity, which suggests that recombination of the photogenerated electrons and holes will happen the least frequently. Additionally, the TRPL lifetime of ASC (0.2902 ns) is shorter than that of other products, which points to a reduction in the exciton population and, consequently the performance of the photocatalytic system is enhanced by an enhancement in the charge separation process and a restriction on the recombination of photoinduced electrons and holes.

3.3.3.3 Bisphenol A photooxidation performance

The ASC photocatalyst performs improved photocatalytic efficiency in the liquid pollution, such as the oxidation of bisphenol A (BPA) (**Figure 3-8**). The degradation of BPA is almost imperceptible without the use of a photocatalyst. After 6 hours, ASC's BPA removal rate was 98.76%, which is much

higher than other companies' rates. For pure CeO_2, only 32.28% was the lowest rate constant for photocatalytic degradation activity. Additionally, the tendency of -Ln (C_t/C_0) as a function of irradiation duration follows the first-order kinetic equation (**Figure 3-8b**). It shows the linear relationship between -Ln (C_t/C_0) and irradiation time, where C_t is the concentration of BPA at a particular time and C_0 is the beginning concentration. The rate constant after numerical computation shows that the Langmuir-Hinshelwood rate governs the degradation of BPA, which is in line with first-order kinetics. The kinetic equation estimates that ASC's rate constant to be 0.5193 h^{-1}. The noteworthily fact that the ASC's value is nearly 1.63, 6.36, and 7.50 times higher than that of AC, SC, and pure CeO_2. This phenomenon shows that the best photocatalytic degradation activity belongs to ASC sample.

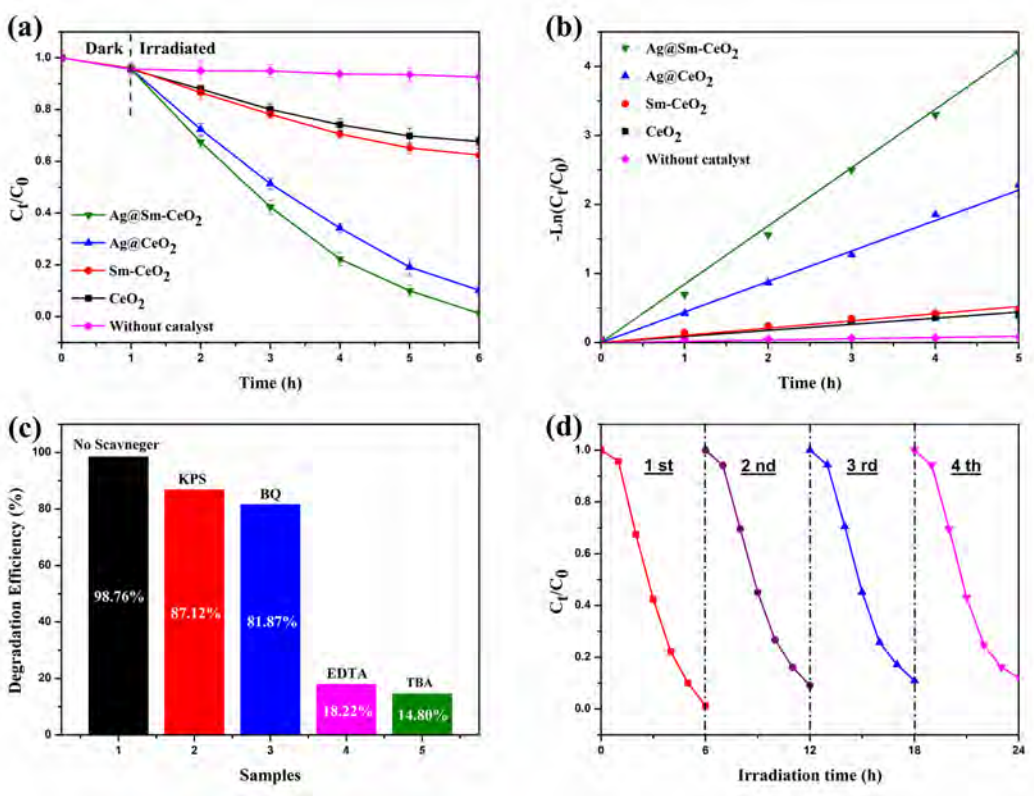

Figure 3-8. (a) Photocatalytic oxidation of aqueous BPA solution, (b) estimation of the kinetics constants, (c) photocatalytic degradation with the addition of BQ, EDTA, TBA or KPS scavengers on ASC, and (d) cycling test of ASC sample.

After confirming the progress of BPA degradation, it is crucial to identify the main active species in this process. The photodegradation efficiency of BPA decreases significantly from 98.76 to 14.80% when TBA scavenger is added (**Figure 3-8c**), showing that one of the primary active species throughout the degradation process is ·OH radicals. The degradation efficiency dropped to 18.22% when EDTA scavenger was introduced, demonstrating that h^+ is also crucial to the photooxidation reaction. After the addition of KPS (87.12%) scavenger and BQ (81.87%) scavenger, respectively, the degradation efficiency of BPA is somewhat decreased. The findings of the trapping investigations show that the main active constituents are ·OH and h^+, whereas $\cdot O_2^-$ and e^- have only little impacts on the decomposition of BPA pollution. Significantly, the rate of photodegradation has not changed after four cycles of photooxidation, indicating that ASC photocatalyst maintains excellent photocatalytic stability (**Figure 3-8d**).

Table 3-3. Results of first principal calculation of all as-prepared samples.

Samples	Energy (Ha)	$Energy_{ads}$ (Ha)	$Distance_{Ag\text{-}slab}$ (Å)
Ag cluster	-369.5306		
CeO_2	-5228.5118		
AC	-5598.0838	-0.0414 (-1.126 eV)	2.21
SC	-5214.9219		
ASC	-5584.4994	-0.04690 (-1.276 eV)	1.64

The reason for the stability of silver loaded in SC is intriguing, even though loading silver on the surface of a semiconductor is generally unstable. As a result, the first principal approach was investigated to learn more about the mechanism, and the findings are compiled in **Table 3-3**. Since SC has a higher overall energy than pure CeO_2, this shows that CeO_2 can be activated by Sm doping.

Positive effect of Ag loading on both materials is indicated by the negative adsorption energy values of ASC and AC. The creation of oxygen vacancies can be the cause of the ASC having more negative E_{ads} than the AC sample [36-38]. Because the silver cluster and slab in ASC are closer together, the oxygen vacancies can trap the silver clusters and further stabilize the system.

3.3.4 Theoretical calculations and proposed photocatalytic mechanism

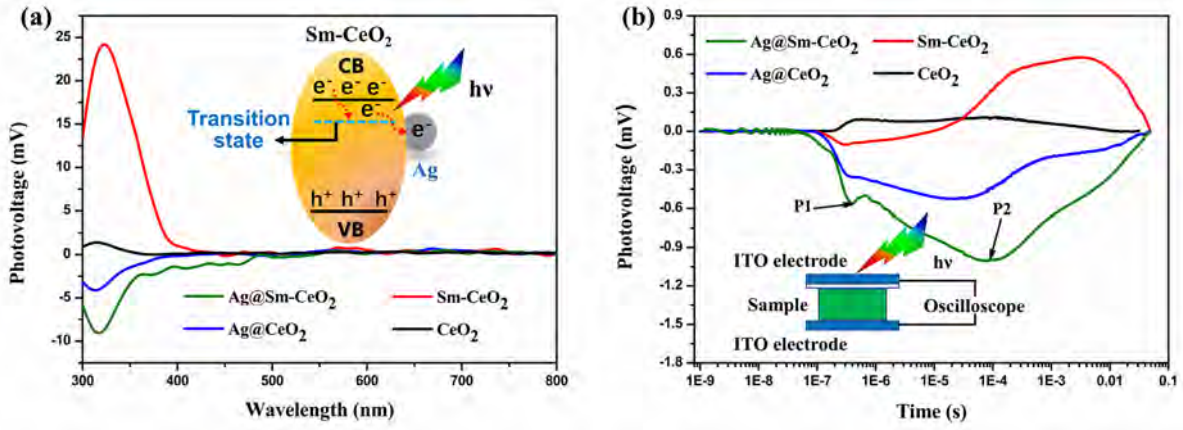

Figure 3-9. (a) SPV spectra and (b) TPV spectra of as-prepared samples. The wavelength and intensity of excitation pulse are 355 nm and 50 μJ, respectively. Inset: schematic setup of TPV measurement.

The SPV approach was used to ascertain the direction in which the charges were transferred between Ag QDs and CeO_2 microspheres (**Figure 3-9a**). A band-to-band transition of photogenerated excitons in intrinsic CeO_2 may be the cause of the largest broadband, which is seen in the SPV spectra of all synthetic materials at 325 nm [39]. In particular, the positive signal of CeO_2 and SC demonstrates that holes transfer to the photocatalysts' illumination side mainly, which is explained by the bandgap transition [40]. On the other hand, the negative reaction of AC and ASC shows that electrons are preferentially transported to the exposed side's surface. Additionally, the SPV intensity of ASC was significantly higher than that of other samples, which might be because more electrons were moving to the CeO_2 surface and generating photovoltage. The reduction co-catalyst function of

silver in the visible range is assumed to be represented by the SPV signal for ASC, which has discrete peaks at 400-500 nm [41, 42]. After the metallic Ag QDs and CeO_2 create a heterogeneous interface, the Fermi energy levels of the two components can converge. The separation of electrons and holes is then accomplished effectively by the injection of Sm-CeO_2's conduction band electrons into the Ag surface under the influence of visible light [43, 44].

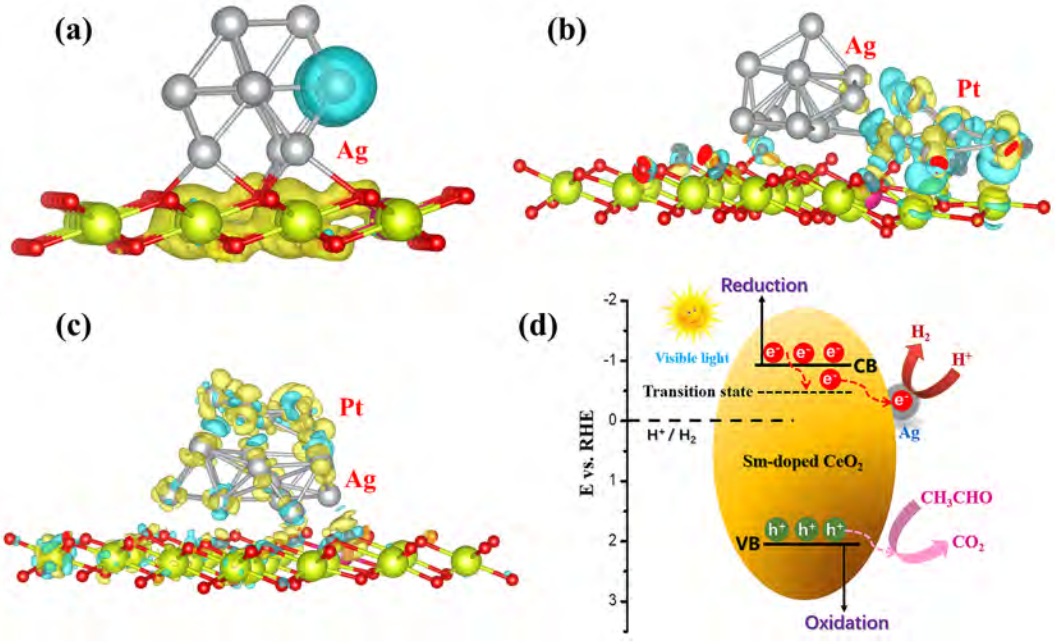

Figure 3-10. Calculated cross view charge density differences of (a) ASC, (b) Ag and Pt particles co-loaded on the surface of the ASC, (c) Pt particles loaded on the surface of the Ag particle, (Color: Ce, yellow; O, red; Sm, rose; Ag, gray; Pt, argent) and (d) proposed mechanism for enhanced photocatalytic performance of CH_3CHO decomposition and water splitting.

The separation and recombination of those photo-generated charges in photocatalysts can also be revealed via TPV technology (**Figure 3-9b**). Firstly, the ASC's TPV signal is negative, indicating that the photoexcited electrons are moving more quickly than the holes [42, 45]. It is mostly related to Ag's lower potential barrier and better capacity to receive electronic signals. The rate at which those photoexcited electrons and holes recombine is decreased by the quick electron transport from CeO_2 to Ag. The TRPL results are likewise consistent with the increased TPV intensity brought on by the

considerable absorption of ASC compared to any other samples, which suggests rapid diffusion of charge carriers. Second, the TPV response of the ASC exhibits two response peaks. The peak period of P1 was reported to be less than 10^{-6} s due to the photogenic charge produced by laser irradiation on the ASC and the charge separation produced by the electric field in the surface charge area [42, 46]. As a result, the diffusion voltage may cause the P2 peak to last longer than 10^{-4} s. The diffusion PV is principally governed by the concentration of photoexcited charges and the correlative diffusion rate of electrons and holes [45, 46].

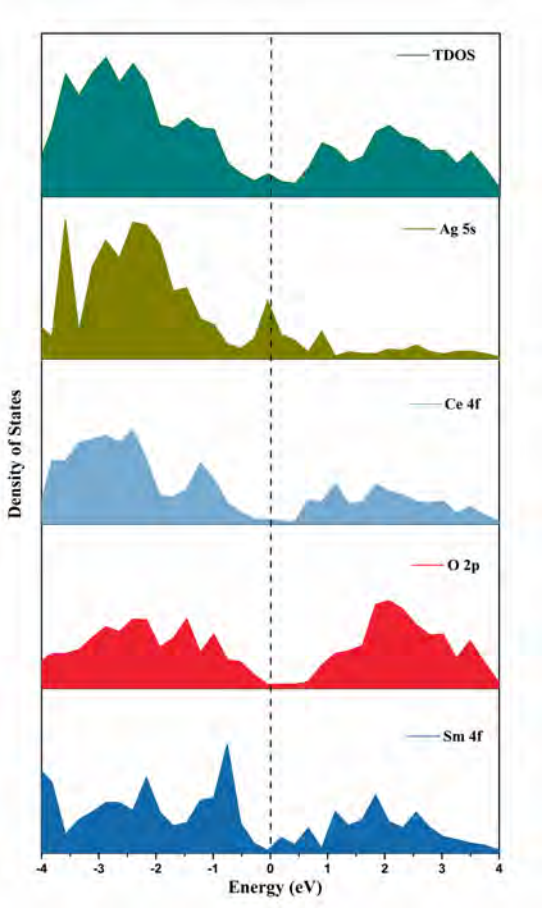

Figure 3-11. The total and partial density of states (DOS) of ASC.

Density functional theory was used to calculate the heterogeneous interface between the SC and the metallic silver in more detail (DFT). According to the difference in charge density shown in **Figure 3-10a**, the electrons move from the SC (yellow region) to the metallic silver side (cyan area),

which is compatible with the results of the experimental SPV and TPV tests.

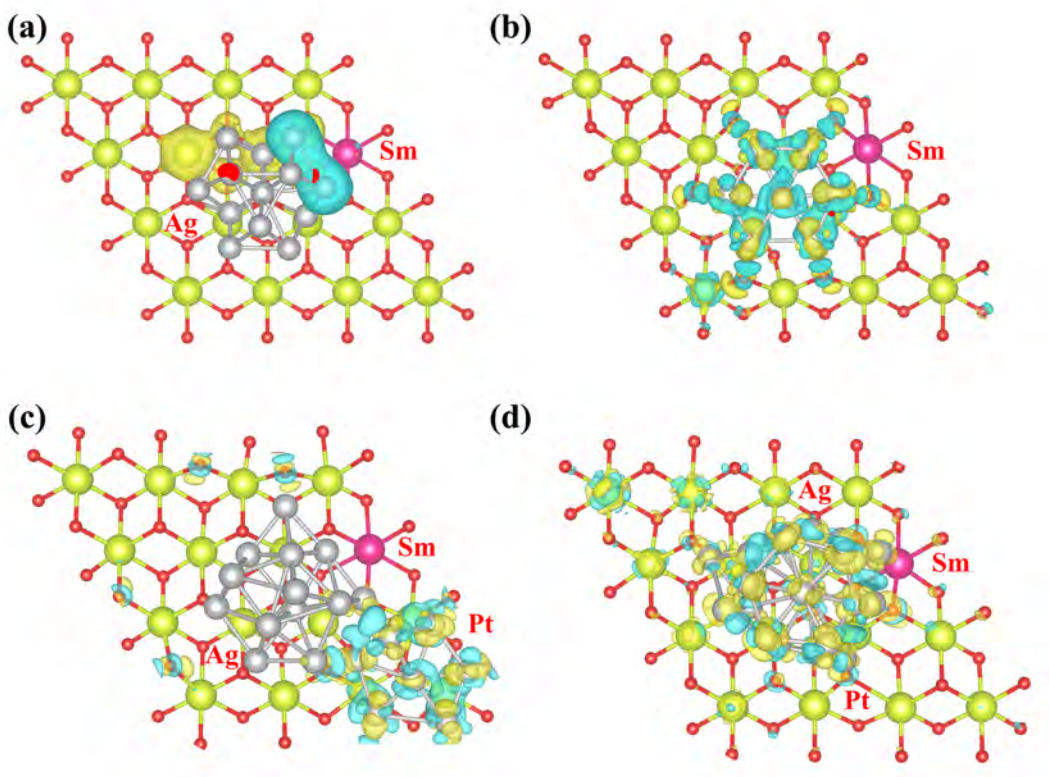

Figure 3-12. Calculated top view charge density differences of (a) ASC, (b) Ag and Pt particles co-loaded on the surface of the ASC, (c) Pt particles loaded on the surface of the Ag particle, and (d) Pt particles loaded on the surface of pure CeO_2. (Color: Ce, yellow; O, red; Sm, rose; Ag, gray; Pt, argent)

Figure 3-11 shows the total and partial density of states (DOS) of the ASC. Ag 5s, Ce 4f, and Sm 4f orbitals dominate the valence-band maximum (VBM) of the ASC, whereas O 2p orbitals dominate the conduction-band minimum (CBM). The charge transfer in the Pt particle and Ag particle co-loaded Sm-doped CeO_2 (PASC) systems was further investigated (**Figure 3-10b-c**). Since Ag had a considerably stronger electron affinity than CeO_2, Pt particles frequently load right next to Ag particles (**Figure 3-12**). The earlier research suggested that Pt particles might work well as a co-catalyst in the hydrogen evolution reaction. The performance of the HER might be greatly enhanced by the increased charge transfer from ASC to Pt [47]. Since electron accumulation benefits from the co-catalyst Pt addition, the photocatalytic H_2 development process considerably benefits from this

development.

Reactive oxygen species play a crucial part in photocatalysis; hence it is essential to investigate how they interact with the catalyst. The findings are compiled in **Table 3-4**. Negative adsorption energy values for all the materials imply that there are positive interactions between oxygen and the CeO_2 based photocatalysts, with the order of the interaction energy being: ASC-O > CeO_2-O > SC-O. It suggests that the most reactive photocatalyst is oxygen absorbed on the ASC [36-38]. The capacity of the photocatalyst to adsorb oxygen is directly reflected by the adsorption energy. The findings demonstrate that ASC and SC have higher adsorption energies than CeO_2, indicating that oxygen can be stabilized by oxygen vacancies (many theoretical results have confirmed this hypothesis). The consequence is a significantly shorter distance between the surface of the photocatalysts and the oxygen. It is remarkable that only 0.065 Å separates oxygen from ASC. It is amazing how close one oxygen atom comes to filling the oxygen vacancy. The oxygen bond distance is the most important variable since it reveals the makeup of the adsorbed oxygen. The initial O-O bond length of 1.225 Å varies as oxygen is adsorbed on the photocatalyst. It is obvious that the interaction between the oxygen and CeO_2 is just physical adsorption since the oxygen bond length on the surface of CeO_2 is virtually identical to its starting value. Since the link between the oxygen and SC's surface is longer than 1.3 Å, superoxide ($\cdot O_2^-$) is naturally formed as a result of the interaction between the two substances. Because of the oxygen vacancy, there is now less space between the oxygen and the photocatalyst surface. This causes the adjacent Ce^{3+} to lose one electron, which is subsequently transferred to the adsorbed oxygen and forms O_2^-. When Ag was applied to the surface of the SC, the oxygen's bond length rose to 1.434 Å, indicating the formation of peroxide species ($\cdot O_2^{2-}$). The O-O bond and the distance between oxygen and ASC are both prolonged by the addition of Ag. We hypothesize that the peroxide anion receives one electron from Ce^{3+} close to the oxygen

vacancy and the other electron from Ag. The photocatalytic processes will be accelerated by the reactive oxygen species created.

Table 3-4. Calculation of the formation of reactive oxygen species.

Samples	Energy (Ha)	$Energy_{ads}$ (Ha)	$Distance_{O\text{-}slab}$ (Å)	$Distance_{O\text{-}O}$ (Å)
O_2	-150.2492			1.225
CeO_2-O1	-5378.7633	-0.0023 (-0.063 eV)	2.697	1.225
CeO_2-O2	-5378.7634	-0.0024 (-0.065 eV)	3.188	1.226
SC-O1	-5365.2085	-0.0374 (-1.017 eV)	0.502	1.319
SC-O2	-5365.2140	-0.0429 (-1.167 eV)	0.494	1.340
ASC-O1	-5734.7516	-0.003 (-0.0816 eV)	2.973	1.230
ASC-O2	-5734.7922	-0.0436 (-1.186 eV)	0.065	1.434

***CeO_2-O1: O2 is close to Ce atom; CeO_2-O2: O2 is far from Ce atom; SC-O1: O2 is close to oxygen vacancy; SC-O2: O2 is far from oxygen vacancy; ASC-O1: O2 is perpendicular to oxygen vacancy; ASC-O2: O2 is parallel to oxygen vacancy.**

Consequently, a logical explanation for the improved photocatalytic capability of ASC is put forth (**Figure 3-10d**). The bandgap is reduced by the production of a transition energy state that is nearer to the conduction band (CB) and leads to a transition energy state with a higher concentration of oxygen vacancies (Ov). The doping-related transition state in Sm-doped CeO_2 can successfully halt the recombination of the photoinduced electron-hole pairs by trapping the photoexcited electrons when exposed to visible light. Afterward, through the heterogeneous interface between the SC and metallic silver, these trapped electrons were transported to the Ag QDs, where Ag simultaneously

increased the capacity to absorb visible light. During the photocatalytic reaction, transferred electrons on the silver will act as active sites for oxygen activation and water reduction splitting. Notably, the photo-induced separation of the holes will increase, which is good for the production of reactive oxygen species. Additionally, for complex photocatalytic redox reactions, they are powerful photocatalytic oxidizers and efficient intermediates. In comparison to those traditional semiconductor photocatalysts, the visible-light-driven CeO_2 generated by Sm doping and Ag QDs anchoring in this paper is certain to boost the photocatalytic performance.

3.4 Conclusions

In conclusion, a one-step hydrothermal method was used to successfully create a Sm-doped CeO_2 photocatalyst that was modified with silver quantum dots. This method is effective, repeatable, and extensible to the creation of additional ceria-based inorganic nanomaterials. By using XRD, HR-TEM and FE-SEM technologies, the structural and morphological data of ASC were characterized. Raman, UV-vis, XPS, PL, and TRPL equipment were used to evaluate the characteristics of optics, defects, and chemical states. For instance, compared to untreated CeO_2, ASC offers respectively skills of reducing water to make hydrogen and converting CH_3CHO to CO_2, that achieves 7.08-times and 6.83-times higher values. Additionally, the photocatalytic activity of the ASC for the photooxidation of BPA solution also shows similar improvements. The increased concentration of Sm ions in ASC is always related to doping, and it can cause the lower bandgap energy (E_g) and restrict the recombination of photoexcited electrons and holes. Additionally, Ag QDs' enhanced visible light reactivity demonstrates that they play an equally important part in the photocatalytic process. Therefore, the development of more economical photocatalysts for a number of possible applications can be facilitated by this study's elaborated ASC heterogeneous photocatalyst.

Reference

1. Montini, T., M. Melchionna, M. Monai, and P. Fornasiero. "Fundamentals and Catalytic Applications of CeO_2-Based Materials." Chem Rev 116 (2016): 5987-6041. https://doi.org/10.1021/acs.chemrev.5b00603.

2. Hanif, Mahadi Abdul, Ye Lin, Fairclough Simon M., Qu Jin, Wu Simson, Chen Wei, Papaioannou Evangelos I., et al. "Beyond Surface Redox and Oxygen Mobility at Pd-Polar Ceria (100) Interface: Underlying Principle for Strong Metal-Support Interactions in Green Catalysis." Applied Catalysis B: Environmental 270 (2020). https://doi.org/10.1016/j.apcatb.2020.118843.

3. Pan, Lun, Minhua Ai, Chenyu Huang, Li Yin, Xiang Liu, Rongrong Zhang, Songbo Wang, et al. "Manipulating Spin Polarization of Titanium Dioxide for Efficient Photocatalysis." Nat Commun 11, (2020): 418. https://doi.org/10.1038/s41467-020-14333-w.

4. Naghavi, S. Shahab, Antoine A. Emery, Heine A. Hansen, Fei Zhou, Vidvuds Ozolins, and Chris Wolverton. "Giant Onsite Electronic Entropy Enhances the Performance of Ceria for Water Splitting." Nat Commun 8, (2017): 285. https://doi.org/10.1038/s41467-017-00381-2.

5. Wang, Zumin, and Ranbo Yu. "Hollow Micro/Nanostructured Ceria-Based Materials: Synthetic Strategies and Versatile Applications." Adv Mater 31, no. 38 (Sep 2019): e1800592. https://doi.org/10.1002/adma.201800592.

6. Shang, Huan, Shun Huang, Hao Li, Meiqi Li, Shengxi Zhao, Jiaxian Wang, Zhihui Ai, and Lizhi Zhang. "Dual-Site Activation Enhanced Photocatalytic Removal of No with Au/ CeO_2." Chemical Engineering Journal 386 (2020). https://doi.org/10.1016/j.cej.2020.124047.

7. Hammond, Oliver S., Karen J. Edler, Daniel T. Bowron, and Laura Torrente-Murciano. "Deep Eutectic-Solvothermal Synthesis of Nanostructured Ceria." Nat Commun 8 (Jan 25 2017): 14150. https://doi.org/10.1038/ncomms14150.

8. Yang, Hui, Bin Xu, Saisai Yuan, Qitao Zhang, Ming Zhang, and Teruhisa Ohno. "Synthesis of Y-Doped CeO_2/PCN Nanocomposited Photocatalyst with Promoted Photoredox Performance." Applied Catalysis B: Environmental 243 (2019): 513-21. https://doi.org/10.1016/j.apcatb.2018.10.057.

9. Xu, Bin, Qitao Zhang, Saisai Yuan, Ming Zhang, and Teruhisa Ohno. "Morphology Control and Characterization of Broom-Like Porous CeO_2." Chemical Engineering Journal 260 (2015): 126-32. https://doi.org/10.1016/j.cej.2014.09.001.

10. Yuan, Saisai, Qitao Zhang, Bin Xu, Zhengyuan Jin, Ya Zhang, Yin Yang, Ming Zhang, and Teruhisa Ohno. "Porous Cerium Dioxide Hollow Spheres and Their Photocatalytic Performance." RSC Adv. 4, (2014): 62255-61. https://doi.org/10.1039/c4ra12127a.

11. Zhang, Sai, ZhengQing Huang, Yuanyuan Ma, Wei Gao, Jing Li, Fangxian Cao, Lin Li, Chun-Ran Chang, and Yongquan Qu. "Solid Frustrated-Lewis-Pair Catalysts Constructed by Regulations on Surface Defects of Porous Nanorods of CeO_2." Nat Commun 8 (May 18 2017):

15266. https://doi.org/10.1038/ncomms15266.

12. Mofarah, Sajjad S., Esmaeil Adabifiroozjaei, Yin Yao, Pramod Koshy, Sean Lim, Richard Webster, Xinhong Liu, et al. "Proton-Assisted Creation of Controllable Volumetric Oxygen Vacancies in Ultrathin $CeO_{(2-X)}$ for Pseudocapacitive Energy Storage Applications." Nat Commun 10, no. 1 (Jun 13 2019): 2594. https://doi.org/10.1038/s41467-019-10621-2.

13. Yang, Can, Run Li, Kai A.I. Zhang, Wei Lin, Katharina Landfester, and Xinchen Wang. "Heterogeneous Photoredox Flow Chemistry for the Scalable Organosynthesis of Fine Chemicals." Nat Commun 11, no. 1 (Mar 6 2020): 1239. https://doi.org/10.1038/s41467-020-14983-w.

14. Pan, Fuping, Xianmei Xiang, Zichen Du, Erik Sarnello, Tao Li, and Ying Li."Integrating Photocatalysis and Thermocatalysis to Enable Efficient CO_2 Reforming of Methane on Pt Supported CeO_2 with Zn Doping and Atomic Layer Deposited MgO Overcoating." Applied Catalysis B: Environmental 260 (2020). https://doi.org/10.1016/j.apcatb.2019.118189

15. Song, Shuyan, Kai Li, Jing Pan, Fan Wang, Junqi Li, Jing Feng, Shuang Yao, et al. "Achieving the Trade-Off between Selectivity and Activity in Semihydrogenation of Alkynes by Fabrication of (Asymmetrical Pd@Ag Core)@(CeO_2 Shell) Nanocatalysts Via Autoredox Reaction." Adv Mater 29, no. 8 (Feb 2017). https://doi.org/10.1002/adma.201605332.

16. Pan, Fuping, Xianmei Xiang, Zichen Du, Erik Sarnello, Tao Li, and Ying Li. "Effect of the Exposed Ceria Morphology on the Catalytic Activity of Gold/Ceria Catalysts for the Preferential Oxidation of Carbon Monoxide.". Chemical Engineering Journal 344 (Jul 15 2018): 545-55. https://doi.org/10.1016/j.cej.2018.03.111.

17. Ye, Lin, Xinping Duan, Simson Wu, Tai-Sing Wu, Yuxin Zhao, Alex W. Robertson, Hung-Lung Chou, et al. "Self- Regeneration of Au/CeO_2 Based Catalysts with Enhanced Activity and Ultra-Stability for Acetylene Hydrochlorination." Nat Commun 10, no. 1 (Feb 22 2019): 914. https://doi.org/10.1038/s41467-019-08827-5

18. Peng, Honggen, Tao Dong, Li Zhang, Caili Wang, Wenming Liu, Jiafeng Bao, Xiang Wang, et al. "Active and Stable Pt-Ceria Nanowires@Silica Shell Catalyst: Design, Formation Mechanism and Total Oxidation of Co and Toluene." Applied Catalysis B-Environmental 256 (Nov 5 2019). https://doi.org/10.1016/j.apcatb.2019.117807

19. Kwak, No Woo, Seung Jin Jeong, Han Gil Seo, Siwon Lee, YeonJu Kim, Jun Kyu Kim, Pilgyu Byeon, Sung-Yoon Chung, and WooChul Jung. "In Situ Synthesis of Supported Metal Nanocatalysts through Heterogeneous Doping." Nat Commun 9, no. 1 (Nov 16 2018): 4829. https://doi.org/10.1038/s41467-018-07050-y.

20. Jiang, Ruibin, Benxia Li, Caihong Fang, and Jianfang Wang. "Metal/Semiconductor Hybrid Nanostructures for Plasmon-Enhanced Applications." Adv Mater 26, no. 31 (Aug 20 2014): 5274-309. https://doi.org/10.1002/adma.201400203

21. Yu, Lian, Ruosi Peng, Limin Chen, Mingli Fu, Junliang Wu, and Daiqi Ye. "Ag Supported on

CeO_2 with Different Morphologies for the Catalytic Oxidation of Hcho.". Chemical Engineering Journal 334 (Feb 15 2018): 2480-87. https://doi.org/10.1016/j.cej.2017.11.121.

22. Grabchenko, M.V., G.V. Mamontov, V.I. Zaikovskii, V. La Parola, L.F. Liotta, and O.V. Vodyankina. "The Role of Metal-Support Interaction in Ag/CeO_2 Catalysts for Co and Soot Oxidation." Applied Catalysis B-Environmental 260 (Jan 2020): 118148. https://doi.org/10.1016/j.apcatb.2019.118148

23. Pereira-Hernández, Xavier Isidro, Andrew DeLaRiva, Valery Muravev, Deepak Kunwar, Haifeng Xiong, Berlin Sudduth, Mark Engelhard, et al. "Tuning Pt-CeO_2 Interactions by High-Temperature Vapor-Phase Synthesis for Improved Reducibility of Lattice Oxygen." Nat Commun 10, no. 1 (Mar 25 2019): 1358. https://doi.org/10.1038/s41467-019-09308-5

24. Wang, Anqi, Qian Wang Zheng, Hui Wang, Yuwen Chen, Chenghui Luo, Dingjun Liang, Bowen Hu, Rongliang Qiu, and Kai Yan. "3D Hierarchical H_2-Reduced Mn-Doped CeO_2 Microflowers Assembled from Nanotubes as a High-Performance Fenton-Like Photocatalyst for Tetracycline Antibiotics Degradation." Applied Catalysis B: Environmental 277 (2020). https://doi.org/10.1016/j.apcatb.2020.119171

25. Gopal, Chirranjeevi Balaji, Farid El Gabaly, Anthony H. McDaniel, and William C. Chueh. "Origin and Tunability of Unusually Large Surface Capacitance in Doped Cerium Oxide Studied by Ambient-Pressure X-Ray Photoelectron Spectroscopy." Advanced Materials 28 (2016): 4692–97. https://doi.org/10.1002/adma

26. Yang, Sang Mo, Shinbuhm Lee, Jie Jian, Wenrui Zhang, Ping Lu, Quanxi Jia, Haiyan Wang, et al. "Strongly Enhanced Oxygen Ion Transport through Samarium-Doped CeO_2 Nanopillars in Nanocomposite Films." Nat Commun 6 (2015): 8588. https://doi.org/10.1038/ncomms9588

27. Zhu, He, Chao Yang, Qiang Li, Yang Ren, Joerg C. Neuefeind, Lin Gu, Huibiao Liu, et al. "Charge Transfer Drives Anomalous Phase Transition in Ceria." Nat Commun 9, no. 1 (Nov 29 2018): 5063. https://doi.org/10.1038/s41467-018-07526-x.

28. Bin, Xu, Yang Hui, Zhang Qitao, Yuan Saisai, Xie An, Zhang Ming, and Ohno Teruhisa. "Design and Synthesis of Sm, Y, La and Nd-Doped CeO_2 with a Broom-Like Hierarchical Structure: A Photocatalyst with Enhanced Oxidation Performance." ChemCatChem 12, no. 9 (2020): 2638-46. https://doi.org/10.1002/cctc.201902309.

29. Xu, Bin, Qitao Zhang, Saisai Yuan, Ming Zhang, and Teruhisa Ohno. "Synthesis and Photocatalytic Performance of Yttrium-Doped CeO_2 with a Porous Broom-Like Hierarchical Structure." Applied Catalysis B: Environmental 183 (2016): 361-70. https://doi.org/10.1016/j.apcatb.2015.10.021

30. O'Neill, Devin B., Daniel Prezgot, Anatoli Ianoul, Cees Otto, Guido Mul, and Annemarie Huijser. "Silver Nanocubes Coated in Ceria: Core/Shell Size Effects on Light-Induced Charge Transfer." ACS Appl Mater Interfaces 12, (Jan 8 2020): 1905-12. https://doi.org/10.1021/acsami.9b18393

31. Jampaiah, Deshetti, Samuel J. Ippolito, Ylias M. Sabri, Benjaram M. Reddy, and Suresh K. Bhargava. "Highly Efficient Nanosized Mn and Fe Codoped Ceria-Based Solid Solutions for

Elemental Mercury Removal at Low Flue Gas Temperatures." Catalysis Science & Technology 5 (2015): 2913–24.
https://doi.org/10.1039/c0xx00000x

32. Perala Venkataswamy, Deshetti Jampaiah, Ahmad Esmaielzadeh Kandjani, Ylias M. Sabri, Benjaram M. Reddy, and M. Vithal. "Transition (Mn, Fe) and Rare Earth (La, Pr) Metal Doped Ceria Solid Solutions for High Performance Photocatalysis: Effect of Metal Doping on Catalytic Activity." Research on Chemical Intermediates 44, no. 4 (2017): 2523-43.
https://doi.org/10.1007/s11164-017-3244-5

33. Zhang, Qitao, Saisai Yuan, Bin Xu, Yangsen Xu, Kuanhong Cao, Zhengyuan Jin, Chuntian Qiu, et al. "A Facile Approach to Build $Bi_2O_2CO_3$/PCN Nanohybrid Photocatalysts for Gaseous Acetaldehyde Efficient Removal." Catalysis Today 315 (2018): 184-93.
https://doi.org/10.1016/j.cattod.2018.03.071

34. Mansingh, S., D. K. Padhi, and K. M. Parida. "Enhanced Visible Light Harnessing and Oxygen Vacancy Promoted N, S Co-Doped CeO_2 Nanoparticle: A Challenging Photocatalyst for Cr(Vi) Reduction." Catalysis Science & Technology 7, no. 13 (2017): 2772-81.

https://doi.org/10.1039/c7cy00499k

35. Jina, Zhengyuan, Naoya Murakamia, Toshiki Tsubotaa, and Teruhisa Ohno. "Complete Oxidation of Acetaldehyde over a Composite Photocatalyst of Graphitic Carbon Nitride and Tungsten(Vi) Oxide under Visible-Light Irradiation." Applied Catalysis B: Environmental 150-151 (2014): 479-85.
https://doi.org/10.1016/j.apcatb.2013.12.048.

36. Zhao, Li, Yangwen Wu, Jian Han, Qiang Lu, Yongping Yang, and Laibao Zhang. "Mechanism of Mercury Adsorption and Oxidation by Oxygen over the CeO_2 (111) Surface: A Dft Study." Materials (Basel) 11, no. 4 (Mar 23 2018). https://doi.org/10.3390/ma11040485

37. Kyoichi, Sawabe, Yoshikawa Yukio, and Satsuma Atsushi. "Density-Functional Theoretical Study on the Role of Lewis and Brønsted Acid Sites on CeO_2(110) Surfaces for Nitrile Hydration." Topics in Catalysis 57, no. 10-13 (2014): 1094-102.
https://doi.org/10.1007/s11244-014-0274-8

38. Zhang, Yong-Chao, Zheng Li, Lei Zhang, Lun Pan, Xiangwen Zhang, Li Wang, Aleem Fazal e, and Ji-Jun Zou. "Role of Oxygen Vacancies in Photocatalytic Water Oxidation on Ceria Oxide: Experiment and Dft Studies." Applied Catalysis B: Environmental 224 (2018): 101-08.
https://doi.org/10.1016/j.apcatb.2017.10.049

39. Zhang, Nannan, Guangshe Li, Tengfeng Xie, and Liping Li. "Amorphous Tantalum Oxyhydroxide Homojunction: In Situ Construction for Enhanced Hydrogen Production." J Colloid Interface Sci 525 (Sep 1 2018): 196-205. https://doi.org/10.1016/j.jcis.2018.04.066

40. Fang, Siman, Songsong Li, Lei Ge, Changcun Han, Ping Qiu, and Ping Qiu. "Synthesis of Novel CoO_x Decorated CeO_2 Hollow Structures with an Enhanced Photocatalytic Water Oxidation Performance under Visible Light Irradiation." Dalton Trans 46, no. 32 (Aug 15 2017): 10578-85.
https://doi.org/10.1039/c6dt04682g

41. Wang, Xinyan, Tongshun Wu, Huan Wang, and Xingguang Su. "Interesting Electron Storage

Phenomenon in the Spherical Ag/TiO_2 Nanocomposites and Its Application for the Decomposition of Acetaldehyde in the Dark." Materials Research Bulletin 73 (2016): 423-28. https://doi.org/10.1016/j.materresbull.2015.10.001

42. Mu, Zhao, Weiping Yan, Rusong Zhao, and Yanhong Lin. "Study on the Photogenerated Charge Transfer and Photoelectrocatalytic Performance of Ag/ZnO Nanorod Arrays under the Irradiation of Simulated Sun Light." Materials Research Express 2, no. 6 (2015). https://doi.org/10.1088/2053-1591/2/6/065008

43. Zhou, Qixing, Shuanglong Ma, and Sihui Zhan. "Superior Photocatalytic Disinfection Effect of Ag-3D Ordered Mesoporous CeO_2 under Visible Light." Applied Catalysis B: Environmental 224 (2018): 27-37. https://doi.org/10.1016/j.apcatb.2017.10.032

44. Ouyang, Xilian, LinTang, Chengyang Feng, Bo Peng, Yani Liu, Xiaoya Ren, Xu Zhu, Jisui Tan, and Xingxin Hu. "Au/CeO_2/g-C_3N_4 Heterostructures: Designing a Self-Powered Aptasensor for Ultrasensitive Detection of Microcystin-Lr by Density Functional Theory." Biosens Bioelectron 164 (Sep 15 2020): 112328.

https://doi.org/10.1016/j.bios.2020.112328

45. Zhang, Lijing, Shuo Li, Bingkun Liu, Dejun Wang, and Tengfeng Xie. "Highly Efficient CdS/WO_3 Photocatalysts: Z-Scheme Photocatalytic Mechanism for Their Enhanced Photocatalytic H_2 Evolution under Visible Light." ACS Catalysis 4 (2014): 3724–29. https://doi.org/10.1021/cs500794j

46. Mahsa, Moradi, Moussavi Gholamreza, Yaghmaeian Kamyar, Yazdanbakhsh Ahmadreza, Srivastava Varsha, and Sillanpää Mika. "Synthesis of Novel Ag-Doped S-MgO Nanosphere as an Efficient UVA/LED-Activated Photocatalyst for Non-Radical Oxidation of Diclofenac: Catalyst Preparation and Characterization and Photocatalytic Mechanistic Evaluation." Applied Catalysis B: Environmental 260 (2020). https://doi.org/10.1016/j.apcatb.2019.118128

47. Wang, Qian, and Kazunari Domen. "Particulate Photocatalysts for Light-Driven Water Splitting: Mechanisms, Challenges, and Design Strategies." Chem Rev 120, no. 2 (Jan 22 2020): 919-85. https://doi.org/10.1021/acs.chemrev.9b00201

Part 4.

Preparation of Y-doped CeO_2/PCN heterojunction photocatalyst with promoted photooxidation and photoreduction performance

Abstract: In this section, Y-doped CeO_2/PCN (YCC) heterojunction photocatalyst was established by adding yttrium-doped CeO_2 by a one-step hydrothermal reaction onto polymeric carbon nitride (PCN). The morphology of each product was examined using HR-TEM and SEM technologies. Besides, XRD, FT-IR, and Raman analyses were applied to describe the products' structural characteristics. Also, UV-vis, PL and VB-XPS spectra were tested to investigate optical absorption and band energy properties. Importantly, according to the XPS data, the surface-active oxygen and trivalent cerium concentration of the YCC photocatalyst were much higher than their in pure CeO_2 and PCN counterparts. In comparison to pure CeO_2, the photooxidation and photoreduction performance of the YCC photocatalyst achieves respectively 5.73-times and 3.74-times better for RhB degradation and H_2O splitting to create H_2 under visible light irradiation. The Y-doping and heterojunction coupling with PCN strategies used in this section not only improves the optical efficiency of visible light, but also effectively prevents the recombination of photogenerated charge carriers, both of which contribute to a synergistic improvement in photoredox performance.

Keywords: Y-doped CeO_2/PCN • Heterojunction photocatalyst • Photoredox performance • Synergistic effect

4.1 Introduction

Recently, scientists have been actively working on the creation of photocatalytic materials with a narrow band gap that react to visible light [1-3]. Several traditional metal oxide semiconductor materials only react weakly to visible light. Simply said, when exposed to UV radiation, they have more photocatalytic activity in the areas of water and organic pollutant degradation. One of the most important rare earth metal oxides is cerium oxide (CeO_2). There are several uses for this material, including solar cells, UV blockers, polishing agents, catalysts, electrolytes, and sensors, have made extensive use of it. The main reasons for this include a number of superb qualities like low toxicity, good thermal and chemical stability, and resistance to photo-corrosion [4-7]. The prevalence of CeO_2 material is primarily caused by the substantial stoichiometric deviation it exhibits due to the simple reduction of Ce^{4+} ions to Ce^{3+} ions, which results in the production of numerous oxygen vacancies (O_v) [8, 9]. Additionally, it has been shown that the production of superoxide radicals during photocatalytic dye degradation is greatly facilitated by larger oxygen vacancy concentrations and improved visible light absorption, both of which are brought about by the presence of more Ce^{3+} ions. [10, 11]. As a result, whether or not oxygen vacancies produced during the synthesis process obviously affect the photocatalytic performance is promoted [12, 13].

The polymeric carbon nitride, also known as PCN, a yellow powder semiconductor, is the most stable of the seven C_3N_4 allotrope phases at room temperature [14]. An interesting polymer photo (electro)catalyst is PCN, which exhibits several remarkable benefits, including great optical and electrical properties, low manufacturing costs, good physical-chemistry stability, and many more. PCN still faces a number of difficult problems, including a high rate of photoinduced electron-hole pair recombination, a small specific surface area, and a finite number of active sites. To get around

these restrictions, a variety of techniques have been devised, including making various PCN nanostructures, doping with metal or non-metal, and fabricating PCN-based heterojunction composites [15-17]. Despite the fact that PCN materials now have a poor quantum efficiency, they offer a fresh, worthwhile research that satisfies the sustainable development approach. Because PCN has a moderate capacity for visible-light absorption, it is frequently used as a good substrate to combine with inorganic nanoparticles to improve their sensitivity to visible light [18, 19]. Strengthening the interfacial contact between PCN and inorganic material is essential to create an effective heterojunction for complex catalytic processes rather than just a simple physical mixing of the two materials.

We therefore created a Y-doped CeO_2/PCN (YCC) heterojunction photocatalyst in this part by easily growing Y-doped CeO_2 on PCN surface. Oxygen vacancy content and CeO_2's ability to absorb visible light can be increased economically by Y-doping and PCN coupling. Insofar as we are aware, here for the first time, YCC heterojunction photocatalyst was produced, clearly setting it apart from the vast majority of past discoveries based on pure CeO_2 photocatalyst. By degrading RhB and producing H_2 when illuminated by visible light, the photocatalytic abilities of YCC were methodically evaluated. In more detail, while the electrons produced by PCN photo-excitation smoothly migrated to the conduction band of Y-doped CeO_2, the photo-induced holes on the valence band of the Y-doped CeO_2 flowed to the valence band of the PCN component. The electron and hole pairs are successfully separated as a result, and the rate of recombination is also considerably decreased. In Conclusion, the matchable band topologies and close interfacial osculation between the two components may be responsible for the YCC hybridized photocatalyst's considerably better photoredox performance than that of its single component.

4.2 Experimental Sections

4.2.1 Materials

Melamine, sodium phosphate, cerium nitrate hexahydrate ($Ce(NO_3)_3 \cdot 6H_2O$) and yttrium nitrate hexahydrate ($Y(NO_3)_3 \cdot 6H_2O$). All of the chemical reagents employed in the experiment were analytical grade, readily accessible in the market, and had a 99.9% purity level. The entire experiment was conducted with deionized water.

4.2.2 Preparation methods

4.2.2.1 Preparation of PCN photocatalyst

A little modification to the previously described procedure was used to prepare the sample PCN [18]. Firstly, 15.0 g of melamine were transferred to a quartz crucible and calcined at a rate of 5 °C/min for 4 hours in an atmosphere of 550 °C. The product was collected after cooling to room temperature and named PCN.

4.2.2.2 Preparation of Y-doped CeO_2 photocatalyst

The typical synthetic processes were illustrated as follows, and the synthesis steps had already been covered [20]. Firstly, 150 ml of deionized water was dissolved simultaneously with 1.74 g of $Ce(NO_3)_3 \cdot 6H_2O$ and 0.16 g of $Y(NO_3)_3 \cdot 6H_2O$ precursors using vigorous magnetic stirring at room temperature for 30 min. The solution was then given 0.015 g of Na_3PO_4 and continuously stirred for 30 minutes. After that, the solution was put into a 200 ml Teflon-lined stainless-steel autoclave and heated for 24 hours at 200 °C. The light-yellow products were obtained by centrifugation, cooled to room temperature, and then washed with ethanol and deionized water at least three times each to

obtain the product of Y-doped CeO_2.

4.2.2.3 Preparation of Y-doped CeO_2/PCN photocatalyst

With the exception of a different dissolution procedure, Y-doped CeO_2/PCN heterojunction photocatalyst was typically synthesized under the same conditions as Y-doped CeO_2. In addition, 0.16 g of $Y(NO_3)_3 \cdot 6H_2O$ precursors and 0.2 g of PCN were simultaneously dissolved in deionized water with $Ce(NO_3)_3 \cdot 6H_2O$. The remaining procedures are the same, and the finished Y-doped CeO_2/PCN (YCC) product is obtained.

4.2.3 Characterization

On a Bruker-AXS X-ray focus, X-ray diffraction (XRD) was carried out using a Cu Ka radiation source (40 kV/4 mA). On KBr-pressed pellets, the samples' Fourier transform infrared spectroscopy (FT-IR) measurements were taken between 400 and 400 cm1. The In Via Laser Confocal Raman Spectrometer was used to calculate the Raman spectra. The products' morphology and elemental mapping were examined using a FE-SEM (Hitachi, S-4800) and HR-TEM (FEI, Tecnai G^2 F30S-TWIN, 300 KV). A Varian Cary 5000 UV-vis spectrophotometer was used to measure diffuse reflectance spectra (DRS) in the UV-visible range. A Shimadzu KRATOS AXIS-NOVA system was used to perform X-ray photoelectron spectroscopy (XPS) at ambient temperature under 10^{-9} Pa utilizing Al K radiation and the C 1s peak (284.6 eV) as a reference. The photoluminescence (PL) spectroscopy measurements were carried out at room temperature using a fluoro-spectrophotometer (Hitachi FL4600) with an excitation wavelength of 325 nm. A Brucker EPR A200 spectrometer was used to record the electron paramagnetic resonance (EPR) radical signals.

4.2.4 Photoelectrochemical measurements

The photocatalyst was dissolved in 30 mL of acetone and put through an ultrasonic treatment for 60 minutes to create the common working electrode. Then, 20 mg of single iodine was added to it to boost its ionic strength, and it was sonicated for 30 minutes. The item was then electroplated onto a 6 cm×1 cm piece of conductive glass using an electrophoresis method and a 15 V DC power supply for 5 minutes (ITO). In order to create the film electrode, the ITO glass was finally cured for 10 hours at 60°C. The working electrode was exposed to light from a 420 nm filter cutoff Xe arc lamp. The electrolyte was an aqueous solution of Na_2SO_4 (0.1M). A Pt electrode served as the counter electrode and an Ag/AgCl electrode served as the reference electrode during photoelectrochemical measurements using an electrochemical analyzer (CHI660D, Shanghai, Chenhua). In addition, the light source switch was controlled with the shutter every 20 seconds to test the time-photocurrent response.

4.2.5 Photocatalytic activities evaluation

4.2.5.1 Degradation of rhodamine B (RhB) experiment

In order to assess the photooxidation activity of as-prepared materials, RhB was used as a pollutant model. A typical experiment involved mixing 120 mg of photocatalyst with 120 mL of a 20 mg/L RhB aqueous solution. The suspension was agitated in the dark for 30 minutes before to irradiation to achieve adsorption-desorption equilibrium. Then, 4 mL of the sample was obtained for each of the photocatalytic tests and filtered to eliminate photocatalyst particles. Finally, the UV-vis spectrophotometer was used to monitor the degradation results in accordance with the maximum absorption peak (λ_{max} = 554 nm for RhB).

4.2.5.2 Hydrogen (H_2) evolution experiment

In a bottom-irradiation vessel coupled to a glass gas circulation system, photocatalytic hydrogen evolution reactions (HER) were conducted. 50 mL of an aqueous solution containing 10 vol% triethanolamine as a sacrificial agent were mixed with 20 mg of the photocatalyst powder. H_2PtCl_6 was dissolved in the aforementioned 50 mL reaction solution to create the 3 wt% Pt deposition as a reducing co-catalyst, which was subsequently in-situ photo-deposited for an hour. With the help of a condensation water circulation system, the reaction temperature was regulated about 15 °C. With the use of an online gas chromatograph, the amount of H_2 produced was calculated (Fuli GC9790 Plus). Before the photocatalytic performance could be seen, the system was entirely degassed and Ar was injected as a carrier gas. The light source was a 300 W Xe lamp with a 420 nm filter cutoff.

4.2.5.3 Photocatalytic reduction of Cr(VI) solution

The GHX-2 photocatalytic reactor was used for the Cr(VI) photocatalytic evaluation test. Simulated visible light source system was a single 250 W Xe lamp with > 420 nm filter, and a temperature control of 25 °C. The following is the procedure for testing the Cr(VI) efficiency of photocatalysis: The reaction flask was first filled with 120 mL of 20 mg/L $K_2Cr_2O_7$ solution, 120 mg of photocatalysts, and 1 mL of 100 mg/mL formic acid. Once the experimental temperature has been set, the circulating water should be opened, and stirring should continue for 60 minutes in the dark to achieve the photocatalyst and Cr(VI) aqueous solution's adsorption-desorption equilibrium. Diphenylcarbazide (DPC) spectrophotometry was used to determine the final Cr(VI) concentration in the filtrate; the purple complex formed by DPC and Cr(VI) had a maximum absorption wavelength of 540 nm in the UV-vis spectrophotometer.

4.2.6 Active species trapping experiments

In order to identify active species in the RhB solution (120 ml, 20 mg/L), the photocatalyst was dispersed with a different scavenger and $K_2Cr_2O_7$ was used as an electron (e^-) scavenger, EDTA-2Na was chosen as the hole (h^+) scavenger, tert-butanol (TBA) was used as the hydroxyl radical(•OH) scavenger. The processes listed below mirrored the RhB photodegradation experiment described in **4.2.5.1**'s experimental section.

4.3 Results and Discussion

4.3.1 Morphology characterization

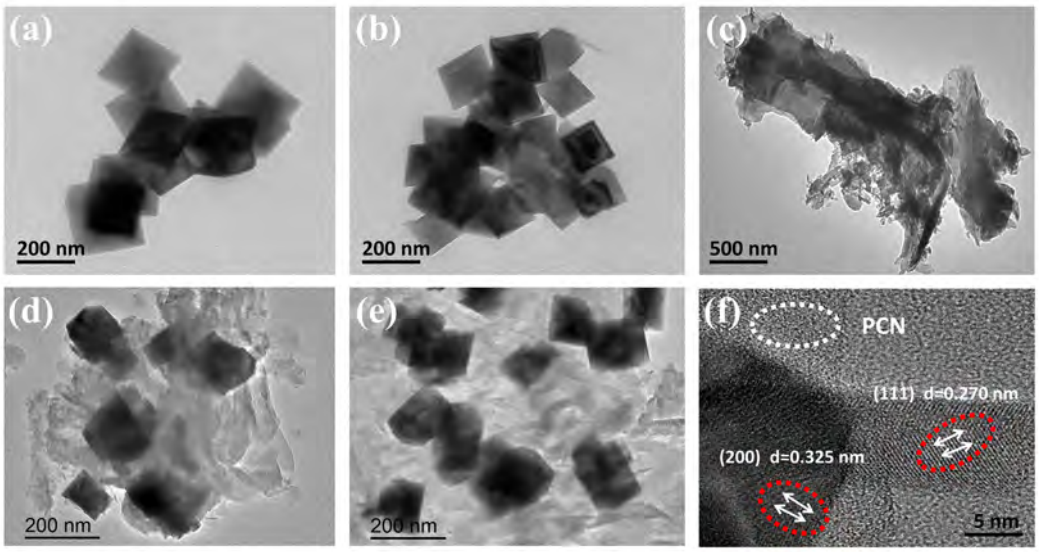

Figure 4-1. TEM and HR-TEM images of (a) CeO_2; (b) PCN; (c) Y-doped CeO_2; (d) CeO_2/PCN and (e) YCC; (f) CeO_2 lattice fringe in YCC of (200) plane and (111) plane.

TEM and HR-TEM analysis were used to describe the morphology of the YCC photocatalyst. **Figure 4-1a** demonstrates the octahedral morphology of hydrothermally produced CeO_2, which has an average particle size of roughly 100 nm. The as-prepared Y-doped CeO_2 nanocrystals still have an octahedral shape, as seen in **Figure 4-1b**. **Figure 4-1c** makes the multi-layered block structure of PCN with a flat surface very evident. As shown in **Figure 4-1d-e**, the coating of PCN with many

CeO_2 and Y-doped CeO_2 polyhedral nanoparticles was successful, then forming the heterojunction in CeO_2/PCN and YCC, respectively.

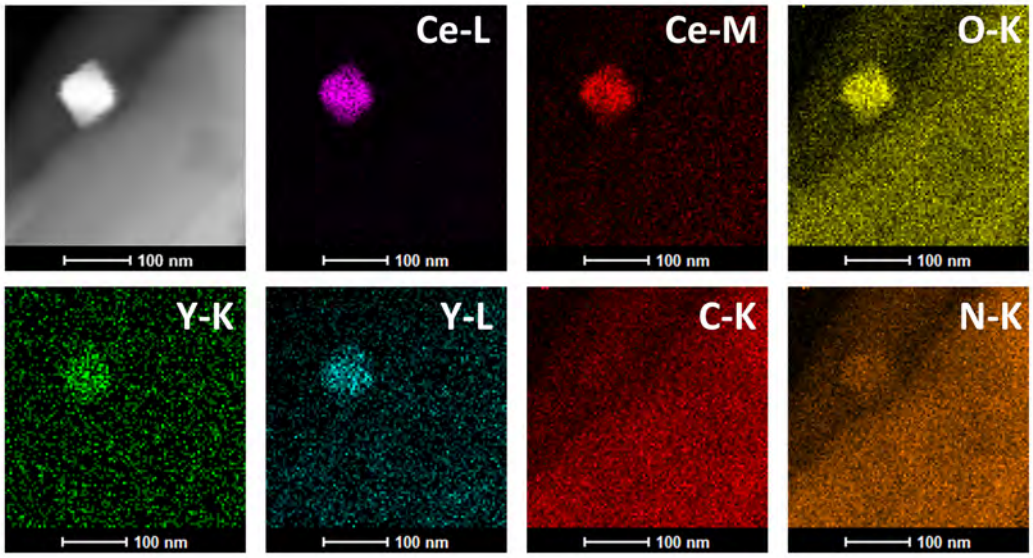

Figure 4-2. EDS elemental mapping of Ce-K; Ce-L; Ce-M; O-K; Y-K; C-K and N-K.

Compared to its PCN and CeO_2 counterparts, this morphology of YCC has a larger BET value of 23.11 m^2/g and 39.26 m^2/g, which is advantageous for catalytic reactions. The seemingly random distribution of CeO_2 nanocrystals anchored on the surface of PCN in YCC is caused by the unpredictable distribution of amino groups inside CN conjugated frameworks. According to **Figure 4-1f**, CeO_2 has lattice spacing values of 0.270 nm and 0.325 nm, which indicate that these crystal faces are part of the (200) and (111) exposed crystal planes of CeO_2's cubic fluorite structure. In the YCC, CeO_2 and PCN have clear interfacial transition zones. We can infer from the data above that the (111) and (200) planes of CeO_2 and the amorphous PCN are where the heterojunction of YCC is created. Additionally, the energy dispersive spectrometer (EDS) measurement reveals that the elements Y, Ce, O, C, and N make up YCC nanocomposites. **Figure 4-2**, which shows the results of the EDS mapping, further demonstrates that these elements have an excellent distribution throughout the YCC's surface and interior. Therefore, according to the aforementioned results, this simple in-situ

hydrothermal process effectively produced the YCC hybridized photocatalyst.

4.3.2 Structure characterization

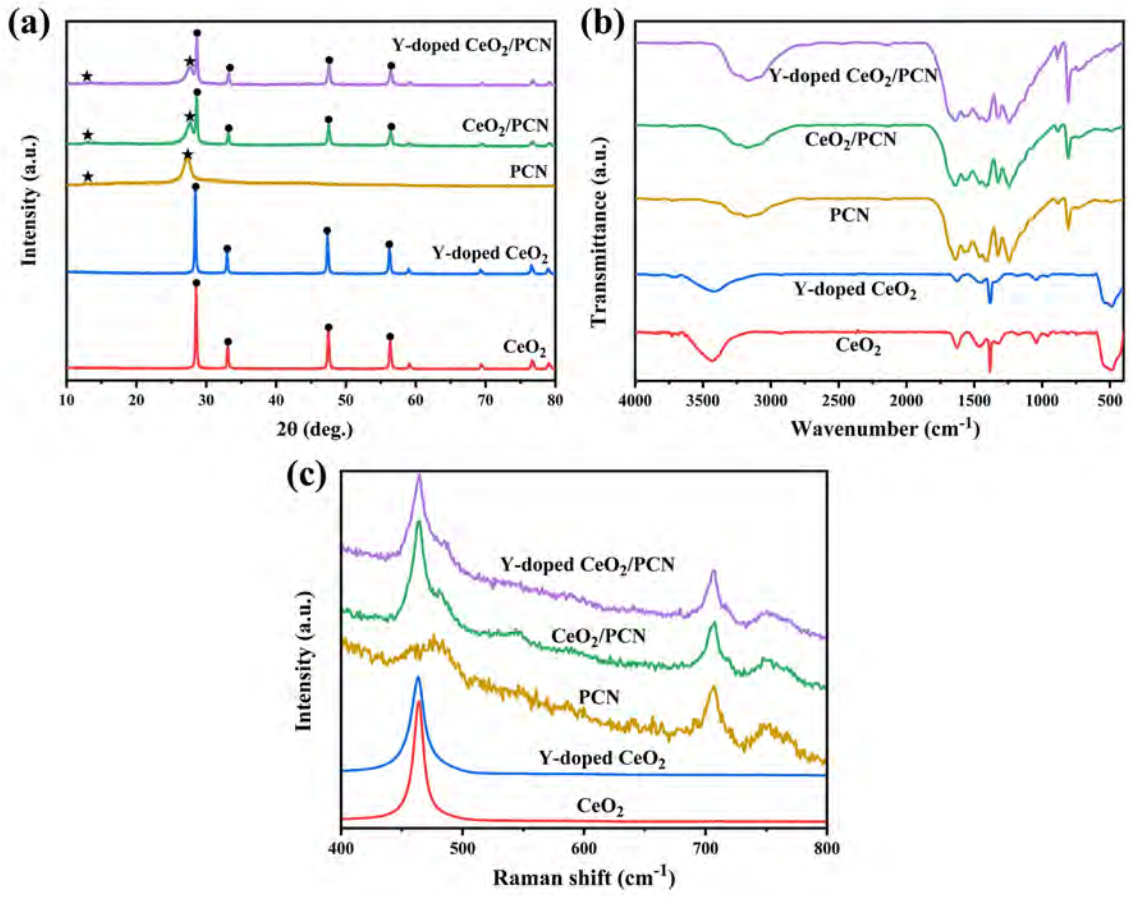

Figure 4-3. Structure characterization of as-prepared samples: (a) XRD patterns; (b) FT-IR spectra and (c) Raman spectra.

The PCN, CeO_2, Y-doped CeO_2, CeO_2/PCN, and YCC's XRD patterns are displayed in **Figure 4-3**. Pure PCN and YCC both exhibit two separate peaks at 13.1° and 27.5°, as seen in **Figure 4-3a**. A typical peak associated with the (002) interlayer stacking of aromatic systems for graphitic materials is the peak with the highest intensity at 27.5 degree. The localization of electrons and increased interaction between the layers may result from the dense structure [21]. At degree of 13.08 of the YCC, the smaller angle peak is attributed to (100) (d = 0.676 nm), which is connected to within-planar repeating nitride pores. Due to the structure's modest rotational angularity, the distance (about

0.730 nm) is slightly lower than the size of one tris-s-triazine unit.

The typical CeO_2 diffraction peaks are located at 28.5°, 33.1°, 47.6°, and 56.4°, and these angles correspond to the crystal planes of the (111), (200), (220), and (311) planes, respectively [22, 23]. These differentiating peaks' relative intensity ratios are comparable to the published standard data in JCPDS cards (No. 34-0394), demonstrating that the CeO_2 nanocrystals as manufactured have not undergone orientation crystal growth. The CeO_2 phase with a cubic fluorite structure can be identified by all of the diffraction lines (space group: Fm-3m (225)). The high degree of crystallinity without impurity peaks suggested by the sharp diffraction peaks of all CeO_2-containing samples suggests that the concentration of the Y dopant has little impact on the products' purity of the crystalline phase. By contrasting the highest XRD peak of CeO_2 with Y-doped CeO_2, it can be shown that the (111) peak of CeO_2 drastically changed after yttrium doping, going from an angle of 28.58° to a lower angle of 28.43°. It shows that the addition of yttrium to the crystal structure of Y-doped CeO_2 caused the crystal lattice to expand noticeably. In general, YCC still has the distinctive PCN and CeO_2 diffraction peaks.

Table 4-1. Summary of lattice parametres, calculated grain sizes and particle sizes of CeO_2, Y-doped CeO_2 and YCC.

Samples	Lattice parametres (Å)	Calculated grainsize (nm)	R_{wp}	Particles size (nm)
CeO_2	5.4129	67.3	9.10	120
Y-doped CeO_2	5.4325	45.2	9.08	120
YCC	5.4286	58.2	8.67	100

Additionally, Rietveld refinements were further carried out on various parameters in accordance with its diffraction lines in [24] in order to analyze the actual doping quantity and the doping position. After yttrium doping, the lattice parameter value (a) of CeO_2 changed from 5.4129 Å to 5.4325 Å

(**Table 4-1**). The successful doping of yttrium into the CeO_2 lattice is indicated by the increased lattice parameter, which allows for the crystal lattice to expand noticeably. Value (a) of the YCC lattice is 5.4286 Å. This outcome is just a little bit worse than the yttrium-doped CeO_2 sample. It might be brought on by the partial restriction of Y^{3+} entry into the CeO_2 lattice caused by the steric hindrance effect produced by PCN and Y-doped CeO_2. The particle size (D) of the samples was estimated using Scherrer's formula (**Table 4-1**). The D values of Y-doped CeO_2 (45.2 nm) and YCC (58.2 nm) are marginally lower than those of the yttrium-doped CeO_2 counterpart (67.3 nm). The outcomes are fairly consistent with the observations made using HR-TEM and SEM. Doping has the effect of reducing the change in particle size caused by the crystal lattice's expansion or contraction [25, 26].

Figure 4-3b displays the FT-IR spectra of PCN, CeO_2, Y-doped CeO_2, CeO_2/PCN, and YCC. For pure PCN, the stretching vibration of C=N is said to be responsible for the peak at 1646 cm^{-1}, whereas the stretching vibration of aromatic C-N is thought to be responsible for the peaks at 1565 cm^{-1}, 1408 cm^{-1}, 1320 cm^{-1}, and 1238 cm^{-1} [24]. The peak near 805 cm^{-1} is attributed to the triazine unit connection's out-of-plane breathing vibration [27, 28]. For pure CeO_2, the Ce-O stretching vibration is what causes the absorption peak at 485 cm^{-1} [29]. The PCN and CeO_2 characteristic vibration peaks are both still present in the case of YCC [30]. The F_{2g} vibration of the fluorite-type structure can be attributed to a significant Raman shift at 460 cm^{-1} of CeO_2. The F_{2g} peak changed from 464.11 cm^{-1} to 463.52 cm^{-1} when yttrium was added to CeO_2, sufficiently demonstrating the addition of Y ions into MO_8 in the CeO_2 lattice. The characteristic peak of PCN, which is seen at 476 cm^{-1}, 706 cm^{-1}, and 752 cm^{-1}, and they were definitely displaced in YCC [31], further demonstrates the strong interaction between Y-doped CeO_2 and PCN.

The equation of $(\alpha h\nu)^n = B(h\nu - E_g)$ was used to describe the semiconductor band's absorption

edge. Where the absorption coefficient is represented by α, the material-dependent constant is represented by B, the discrete photon energy is represented by h, the absorption bandgap is represented by E_g, and the diversity of electronic transitions is represented by n, According to calculations shown in **Figure 4-4b**, the band gaps of CeO_2, Y-doped CeO_2, and PCN are 2.88 eV, 2.79 eV, and 2.62 eV, respectively. CeO_2/PCN and YCC have total band gaps of 2.72 eV and 2.66 eV, respectively. Evidently, in comparison to CeO_2 monomer, composite materials displayed considerable red-shift (**Figure 4-4a**). If the band structures of the two parts of the YCC are suitably matched, they can effectively facilitate the separation of the photogenerated charges and accelerate the photocatalytic redox processes.

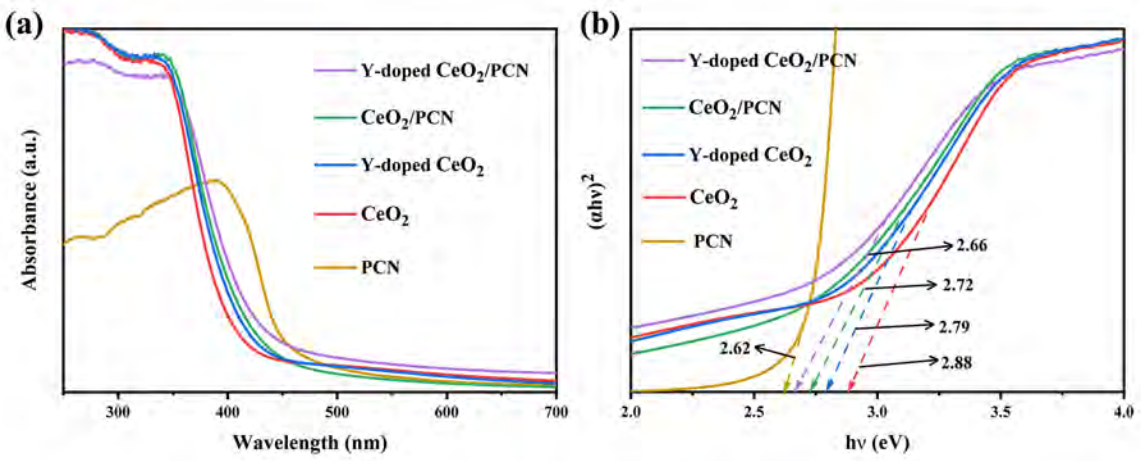

Figure 4-4. (a) UV-vis absorbance spectra and (b) Kubelka-Munk spectra of samples.

XPS analysis was used to look at the surface chemical states of YCC and the interaction between PCN and CeO_2. According to the survey spectra of YCC, the prepared composite contains the elements Ce, O, Y, C, and N, which is in line with the findings of the EDS. Following deconvolution, two group peaks (designated as v and u) were obtained, which were shown in **Figure 4-5a** [32, 33]. As agreed with published values [32], the labels of (U, V), (U_2, V_2), and (U_3, V_3), which come from the final states of Ce ($3d^94f^0$) O ($2p^6$), Ce ($3d^94f^1$) O ($2p^5$), and Ce ($3d^94f^2$) O ($2p^4$), respectively, can

be categorized as Ce $3d_{5/2}$ and Ce $3d_{3/2}$ connected to Ce^{4+}, according to prior studies. For the Ce 3d bond energy peak attributed to Ce^{3+}, there are two pairs of doublets (U_0, V_0) and (U_1, V_1), and the double lines represent Ce ($3d^9 4f^1$) O ($2p^6$) and Ce ($3d^9 4f^1$) O ($2p^5$), respectively. The Ce^{3+}/Ce^{4+} peak positions in the YCC were higher binding energy than their CeO_2 counterparts, attesting to the formation of a heterojunction between PCN and CeO_2.

Calculations were made to determine the proportion of cerium in the tervalent oxidation state. And **Table 4-2** provided a summary of the [Ce^{3+}] concentration values. In comparison to the concentrations in the CeO_2 (18.13%), Y-doped CeO_2 (22.88%), and CeO_2/PCN (24.17%) samples, the [Ce^{3+}] concentration in the YCC sample was enhanced to a level of 27.90%. Due of the stabilizing impact of trivalent cerium ions on PCN support, it also supports the idea that CeO_2 and PCN interact strongly in YCC [34].

Table 4-2. Calculated [Ce^{3+}] and [O_{sur}] concentrations of as-prepared samples from XPS.

Samples	[Ce^{3+}]%	[O_{sur}]%
CeO_2	18.13	28.76
Y-doped CeO_2	22.88	30.17
CeO_2/PCN	24.17	33.38
YCC	27.90	37.16

As **Figure 4-5b** displayed, the O 1s signal may also be seen. The lattice oxygen (O_{lat}) and surface oxygen (O_{sur}) of CeO_2 were attributed to the YCC's O1s peaks at 529.49 eV and 532.04 eV, respectively. When compared to a CeO_2 sample without yttrium doping and PCN hybridization, the lattice oxygen and surface oxygen binding energies in YCC both clearly changed to higher binding energies. We were able to determine the surface oxygen concentration [O_{sur}] following deconvolution

and multiple-peak separation, and the outcomes for surface active oxygen [O_{sur}] were also presented in **Table 4-2**. The percentage of [O_{sur}] for the YCC is roughly 37.16%, which is significantly greater than the percentage for other samples. The surface oxygen binding energy is primarily affected by the strong contact brought on by YCC, which can also increase surface oxygen activity [35]. The oxygen vacancy content strongly affects by the number of photoexcited electron-hole pairs, as well as their recombination and separation. As a result, YCC with comparatively greater oxygen vacancy content may exhibit significantly improved photocatalytic performance.

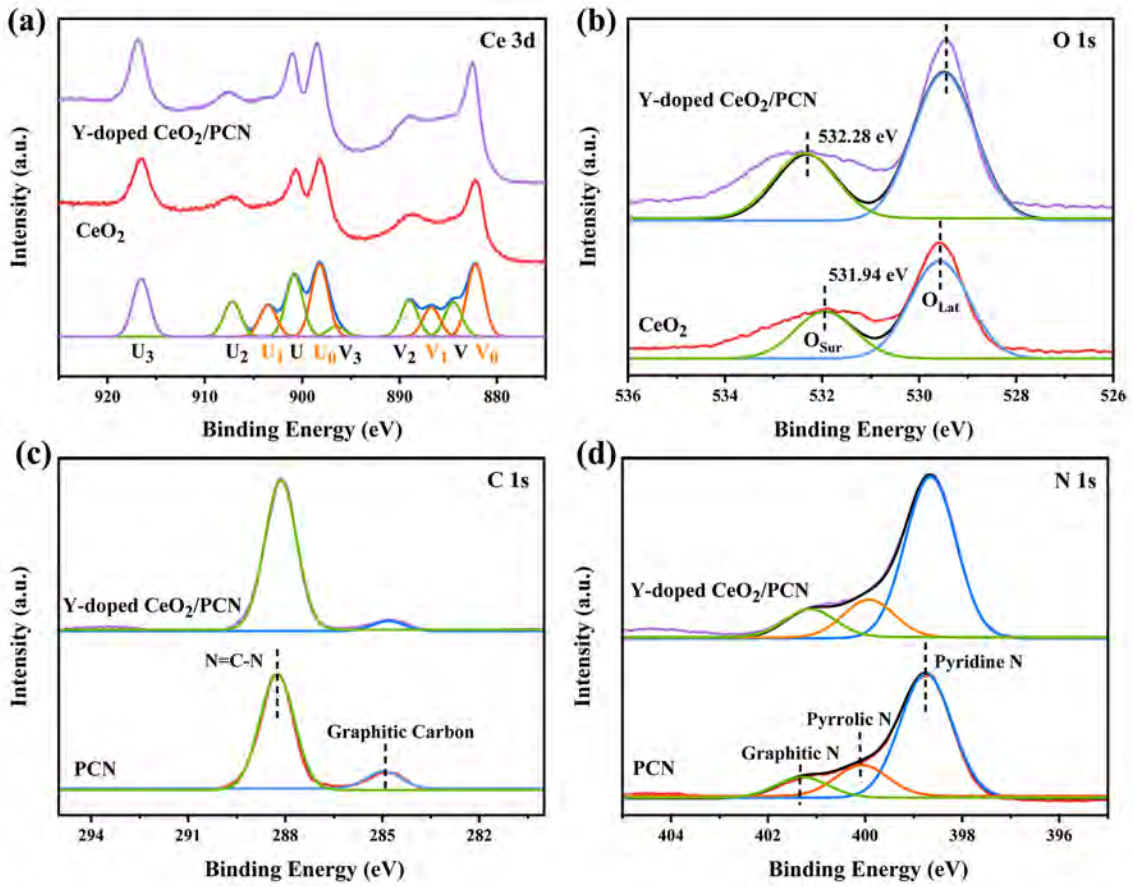

Figure 4-5. High resolution of XPS spectra: (a) Ce3d (b) O1s (c) C1s and (d) N1s.

The primary characteristics of C 1s were shown in **Figure 4-5c**; The sp^2-bond carbon (N=C-N) of PCN was responsible for the characteristic peak at 288.24 eV, while the graphitic carbon of PCN was responsible for the distinctive peak at 284.69 eV [35]. The binding energy of the sp^2-bond carbon

in YCC was 288.14 eV, which is around 0.10 eV less than in PCN. The pyridine N, pyrrolic N, and graphitic N, which would be allocated to three fitted peaks at 398.81 eV, 400.07 eV, and 401.3 eV, respectively, were obtained from the deconvoluted N 1s peak of PCN in **Figure 4-5d** [36]. Pyridine N's binding energy in YCC is 398.65 eV, a decrease of 0.16 eV from PCN. The binding energies of the Ce 3d and O 1s peaks in YCC shifted to a higher value than their CeO_2 counterparts, but they remained slightly lower than those of PCN. In terms of chemistry, the oppositely shifting substantially promoted the interactions between PCN and Y-doped CeO_2 [37, 38]. The XPS data therefore thoroughly revealed the establishment of heterojunction in YCC nanocomposite was thus fully illustrated by the XPS results, which were also in line with the findings of the TEM, XRD, FT-IR, and Raman analyses that were mentioned earlier.

4.3.3 Photocatalytic redox activity

4.3.3.1 Photocatalytic degradation of RhB

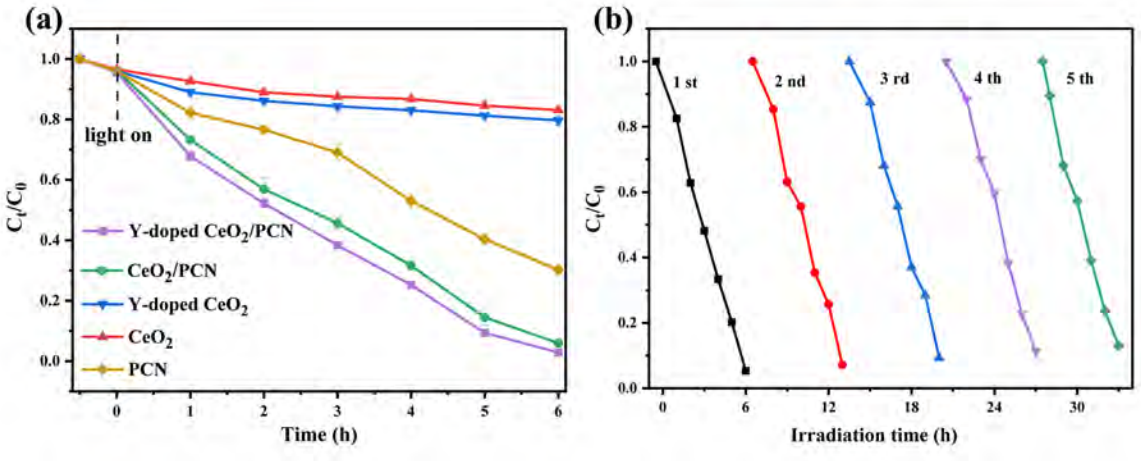

Figure 4-6. Activity evaluation: (a) RhB photooxidation variation curves and (b) Stability test.

The degradation of the RhB pollutant was used to gauge the samples' photooxidation capacity. **Figure 4-6a** shows that the degradation curve of YCC, which is obviously superior than other samples, reached 97.12% after 360 mins of visible light irradiation. On the other hand, due to their weak visible

light absorption and limited specific surface area, CeO_2 and Y-doped CeO_2 samples performed less well in the RhB degrading process. Additionally, **Figure 4-6b** looked at the kinetics of RhB's photocatalytic breakdown. Equation of $-In(C_t/C_0) = kt$ states that the variation in a first-order kinetics equation describes how RhB concentration changes over time. RhB's initial concentration is C_0, and its current concentration is C_t at a specific moment. Calculations show that the rate constant and concentration change are consistent, proving that the Langmuir-Hinshelwood rate rule governs RhB oxidation.

Table 4-3. Summary of the first order kinetic equation and RhB photooxidation reaction rate constant of as-prepared samples.

Samples	The first order kinetic equation	K(h^{-1})	R^2
PCN	$-In(C_t/C_0) = 0.0573t$	0.0573	0.9733
CeO_2	$-In(C_t/C_0) = 0.0388t$	0.0388	0.9682
Y-doped CeO_2	$-In(C_t/C_0) = 0.0440t$	0.0440	0.9511
CeO_2/PCN	$-In(C_t/C_0) = 0.1738t$	0.1738	0.9523
YCC	$-In(C_t/C_0) = 0.2315t$	0.2315	0.9550

Table 4-3 lists the results for rate constants. It is noteworthy that the photooxidation removal of RhB containments by the YCC sample was 5.97, 4.04, and 1.33 times higher than that of CeO_2, PCN, and CeO_2/PCN. Four further cycles of photocatalytic degradation RhB tests were conducted in order to examine the stability and repeatability of the photooxidation activity of YCC. **Figure 4-6c** displays the outcomes, demonstrating that after five iterations of photocatalytic oxidation processes, the photodegradation rate has essentially not changed. As a result, the YCC composited photocatalyst exhibits excellent photocatalytic stability and reusability.

4.3.3.2 Photocatalytic hydrogen evolution and reduction of Cr(VI)

Figure 4-7a illustrates the after 120 minutes of visible light exposure on YCC, the H_2 generation rate was 48.5 $mol^{-1}•h^{-1}$, which is 3.74 times and 3.06 times greater than that of its CeO_2 (13.0 $mol^{-1}•h^{-1}$) and PCN (15.8 $mol^{-1}•h^{-1}$) counterparts, respectively. This data is offered to help assess the photoinduced reduction activity of the prepared photocatalysts. Additionally, the rates of H_2 generation for Y-doped CeO_2 and CeO_2/PCN are 24.4 and 28.6 $mol^{-1}•h^{-1}$, respectively, and both are significantly lower than those of YCC.

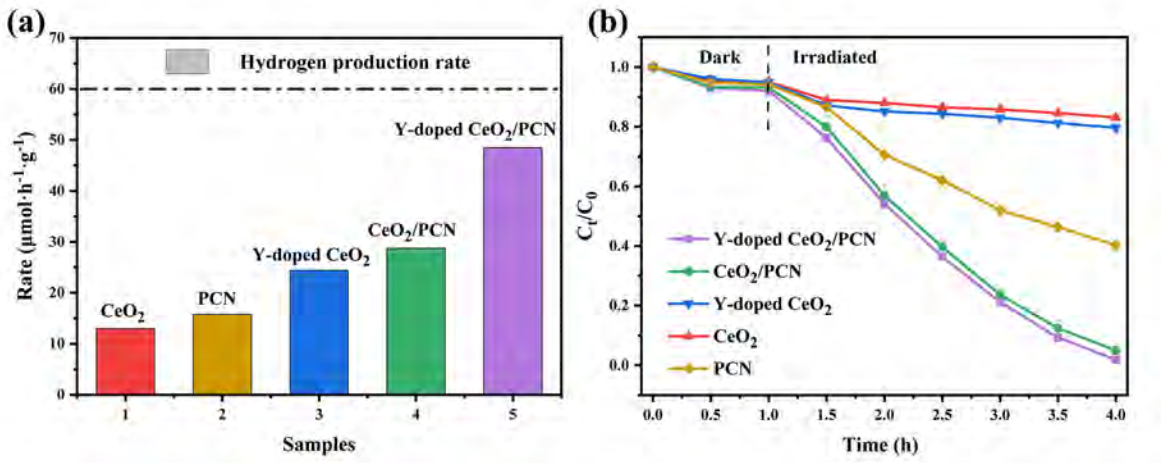

Figure 4-7. (a) Photoreduction activity for H_2 production of samples and (b) Cr(VI) adsorption and photocatalytic reduction performance.

Additionally, when compared to pure CeO_2, YCC demonstrated clearly greater adsorption as well as quicker photocatalytic reduction of Cr(VI) (shown in **Figure 4-7**). The degradation rate of YCC reached 98.12% in just 4 hours, which was 1.61 and 5.79 times larger, respectively, than that of pure PCN (60.76%) and CeO_2 (16.94%). The reaction rate constant (k) for each sample was calculated in order to compare the photocatalytic activities of Cr(VI) quantitatively. In comparison to pure CeO_2 (0.0127 min^{-1}) and PCN (0.0651 min^{-1}), YCC's greatest K value was 0.4287 min^{-1}. As both photooxidation activity and photocatalytic reduction capacity are simultaneously increasing, YCC is therefore a truly efficient bifunctional photocatalyst [39].

4.3.4 Proposed Mechanism

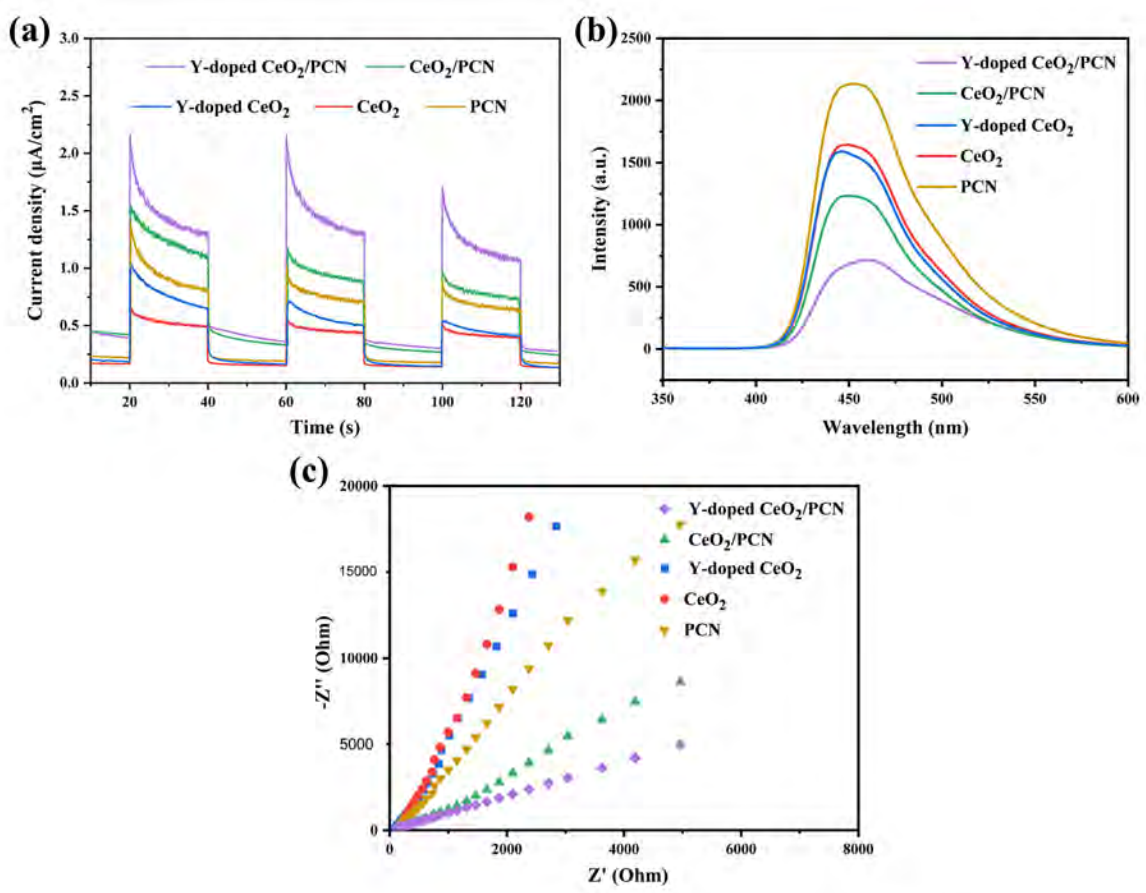

Figure 4-8. Photo-elctrochemical characterization: (a) Transient photocurrent response; (b) PL spectra; and (c) EIS Nynquist plots of as-prepared samples.

The photocurrent-time response was used to assess the kinetics of charge separation at the interface. It is evident from the photocurrent response curves shown in **Figure 4-8a** that when the light source is turned on and off, the photocurrent response curves of all samples rapidly rise and decrease, demonstrating their inherent semiconductor nature. In comparison to PCN (0.76 μA/cm^2), CeO_2 (0.52 μA/cm^2), Y-doped CeO_2 (0.92 μA/cm^2), and CeO_2/PCN (1.24 μA/cm^2), the photocurrent density of YCC reached 1.41 μA/cm^2, which is 1.85, 2.71, 1.52 and 1.13 times higher, respectively. The enhanced photocurrent shows that the YCC separates photogenerated charge carriers far more effectively than counterpart samples. The stronger the photocurrent intensity, the more efficiently photogenerated electrons and holes can be transferred [41]. To take part in the ensuing photocatalytic

redox processes and boost photocatalytic performance, YCC will produce significantly more segregated photo-induced electrons and holes.

The photoluminescence (PL) examination was carried out to ascertain the electron-hole pairs recombination rate of each sample, and the matching PL emission spectrum is displayed in **Figure 4-8b**. Surface defects frequently exist between the O_{2p} valence band and the Ce_{4f} conduction band, causing a large peak cantered at 450 nm in both the pure and Y-doped CeO_2 [43]. It is well known that oxygen vacancies are the most common surface defects in CeO_2. It's interesting to note that after compositing, both CeO_2 and PCN's PL emission intensity was significantly decreased. As a result, the rate at which hole and electron pairs recombine within a single component can be decreased by connecting PCN with CeO_2, as shown by PL experiments [44]. The YCC sample in particular displays the lowest PL intensity, demonstrating that the constructed heterojunction structure has greatly improved the separation of photo-induced carriers in this sample. So the photocatalytic redox performance can therefore be clearly enhanced.

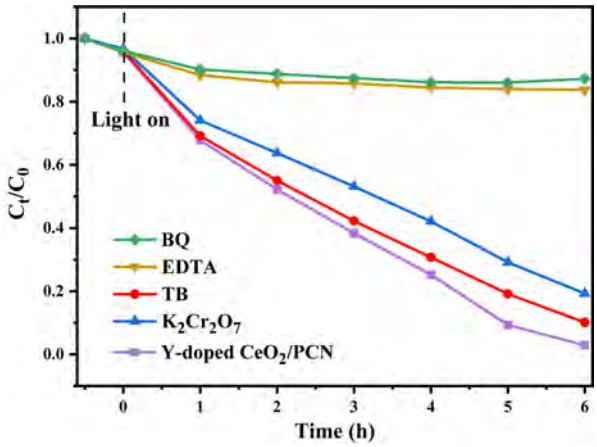

Figure 4-9. Degradation of RhB with the addition of BQ, EDTA, TBA and $K_2Cr_2O_7$ scavengers.

Figure 4-8c displays the electrochemical impedance spectra (EIS) Nyquist plots for the pure PCN, CeO_2, Y-doped CeO_2, CeO_2/PCN, and YCC. Charge transmission is indicated by the semicircle on the EIS plot. The fact that the arc radius of the YCC is much less than that of the PCN and CeO_2

counterparts suggests that the YCC heterojunction can significantly improve the transfer efficiency of photoexcited electron-hole pairs generated by the internal electric field and interfacial interaction [42]. In general, the smaller the semicircle's diameter, the lower the resistance to electron transport in the photocatalyst. Additionally, it means that photogenerated electrons and holes can be separated more quickly, which enables improved photocatalytic activity [15].

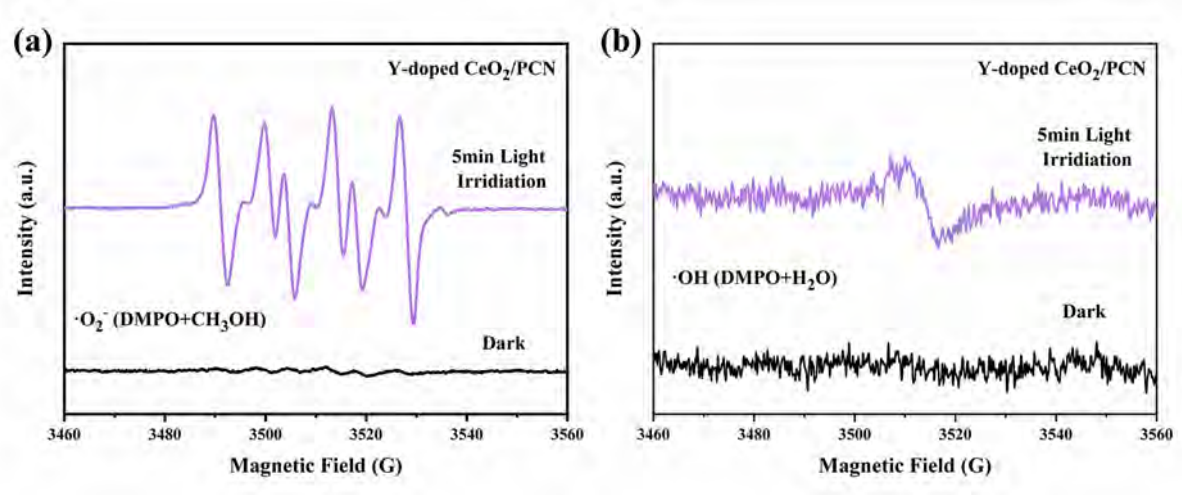

Figure 4-10. EPR spectra of YCC photocatalyst.

Trapping studies were utilized to identify the main active species in the photocatalytic processes and to definitively probe the promotion mechanism. **Figure 4-9** showed that the addition of tert-butanol (TBA, 1 mM) as a •OH scavenger somewhat reduced the efficiency of RhB's degradation. Additionally, $K_2Cr_2O_7$ (1 mM) as an electron (e^-) scavenger exhibited less of an impact on the degradation efficiency. Furthermore, RhB pollution was substantially less effective in degrading when ethylenediaminetetraacetic acid disodium (EDTA-2Na, 1 mM) was added as a hole (h^+) scavenger. Additionally, 1, 4-benzoquinone (BQ, 1 mM) as an $•O_2^-$ scavenger also demonstrated a significant impact on the ultimate degradation rate [45, 46]. According to the active substance capture tests' findings, the principal active substances in the breakdown of RhB under visible light irradiation were $•O_2^-$ and h^+, while OH and e^- had little effects. By using EPR, the reactive oxygen species (ROS)

•O_2^- was effectively found. According to **Figure 4-10**, the very weaker •OH signal and stronger •O_2^- signal are caught in YCC after 5 minutes of visible light irradiation. The outcome is in line with the findings of the experiment involving active species trapping.

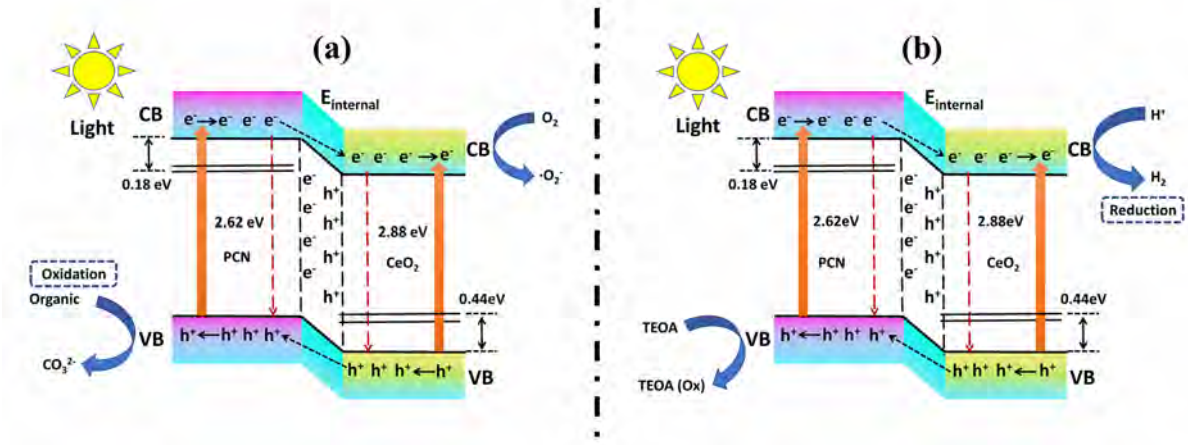

Figure 4-11. Proposed mechanism for photo-redox promotion on YCC photocatalyst.

The proposed schematic diagram of a potential photocatalytic mechanism for YCC was based on the studies mentioned above. They can effectively construct a charge-separation-type heterojunction structure thanks to the deduced from VB-XPS and Tauc plot matchable overlapping band energies of PCN (CB=-1.05 eV, VB=1.57 eV), and CeO_2 (CB=-0.87 eV, VB= 2.01 eV). By using visible light to excite and separate the electrons and holes in the YCC, the electrons in the conduction band of PCN smoothly transition to the conduction band of CeO_2, while the holes in the valence band of CeO_2 migrate to the valence band of PCN, resulting in a stable built-in electric field in the YCC heterojunction interfaces. The internal electric field effectively prevents active photo-generated electrons and holes from recombining. The YCC heterojunction, as shown in **Figure 4-11**, provides expected since more photogenerated holes and electrons collect in the CB of CeO_2 and VB of PCN in YCC, the associated photooxidation of RhB dye and proton photoreduction to make hydrogen function better than expected.

4.4 Conclusions

To summarize, a straightforward in-situ hydrothermal technique was used to create the Y-doped CeO_2/PCN hybridized photocatalyst. The morphology and structure information of the as-prepared YCC photocatalyst were carefully examined using a variety of spectroscopic techniques. And the YCC nanocomposited photocatalyst has a bandgap value that was 0.22 eV lower than that of pure CeO_2. Under visible light irradiation, YCC performed superior photoredox performance, allowing for RhB degradation and H_2O photoreduction to produce H_2 at rates that are 5.73 times and 3.74 times higher than those of pure CeO_2, respectively. A proposed mechanism was as a result created for superexcellent YCC heterojunction, which also demonstrated how the matching band energies of PCN and CeO_2 helped to create a built-in electric field and separate photogenerated holes and electrons efficiently for improving their photooxidation and photoreduction performance at the same time. As a result, this research can offer a practical method for restricting various redox processes are triggered by the photogenerated electrons and holes recombining on the photocatalyst surface.

Reference

1. Chen, De-ming, Gang Xu, Lei Miao, Setsuo Nakao, and Ping Jin. "Sputter Deposition and Computational Study of M-TiO_2 (M=Nb, Ta) Transparent Conducting Oxide Films." Surface and Coatings Technology 206, no. 5 (2011): 1020-1023. https://dx.doi.org/10.1016/j.surfcoat.2011.04.007.

2. Fu, Tao, Jian-min Sun, Zafer Alajmi, and Feng Wu. "Sol-Gel Preparation, Corrosion Resistance and Hydrophilicity of Ta-Containing TiO_2 Films on Ti6al4v Alloy." Transactions of Nonferrous Metals Society of China 25, no. 2 (2015): 471-476. https://dx.doi.org/10.1016/s1003-6326(15)63626-3.

3. Pan, J. W., C. Li, Y. F. Zhao, R. X. Liu, Y. Y. Gong, L. Y. Niu, X. J. Liu, and B. Q. Chi. "Electronic Properties of TiO_2 Doped with Sc, Y, La, Zr, Hf, V, Nb and Ta." Chemical Physics Letters 628 (2015): 43-48. https://dx.doi.org/10.1016/j.cplett.2015.03.056

4. Bueno-López, A. "Diesel Soot Combustion Ceria Catalysts." Applied Catalysis B: Environmental 146 (2014): 1-11. https://dx.doi.org/10.1016/j.apcatb.2013.02.033

5. Lee, Chong-il, Qing-long Meng, Hiroshi Kaneko, and Yutaka Tamaura. "Dopant Effect on Hydrogen Generation in Two-Step Water Splitting with CeO_2–ZrO_2–MO_x Reactive Ceramics." International Journal of Hydrogen Energy 38, no. 36 (2013): 15934-15939. https://dx.doi.org/10.1016/j.ijhydene.2012.09.111

6. Qi, Gongshin and Ralph T. Yang. "Performance and Kinetics Study for Low-Temperature SCR of NO with NH_3 over MnO_x-CeO_2 Catalyst." Journal of Catalysis 217, no. 2 (2003): 434-441. https://dx.doi.org/10.1016/s0021-9517(03)00081-2

7. Trovarelli, Alessandro. "Catalytic Properties of Ceria and CeO_2-Containing Materials." Catalysis Reviews 38, no. 4 (1996): 439-520. https://dx.doi.org/10.1080/01614949608006464

8. Jampaiah, Deshetti, Katie M. Tur, Perala Venkataswamy, Samuel J. Ippolito, Ylias M. Sabri, James Tardio, Suresh K. Bhargava, and Benjaram M. Reddy. "Catalytic Oxidation and Adsorption of Elemental Mercury over Nanostructured CeO_2–MnO_x Catalyst." RSC Advances 5, no. 38 (2015): 30331-30341. https://dx.doi.org/10.1039/c4ra16787b.

9. Shan, Wenpo, Fudong Liu, Yunbo Yu, and Hong He. "The Use of Ceria for the Selective Catalytic Reduction of NO_x with NH_3." Chinese Journal of Catalysis 35, no. 8 (2014): 1251-1259. https://dx.doi.org/10.1016/s1872-2067(14)60155-8.

10. Mandal, Bappaditya and Aparna Mondal. "Solar Light Sensitive Samarium-Doped Ceria Photocatalysts: Microwave Synthesis, Characterization and Photodegradation of Acid Orange 7 at Atmospheric Conditions and in the Absence of Any Oxidizing Agents." RSC Advances 5, no. 54 (2015): 43081-43091. https://dx.doi.org/10.1039/c5ra03758a.

11. Saranya, Jayapalan, Kugalur Shanmugam Ranjith, Padmanaban Saravanan, Devanesan Mangalaraj, and Ramasamy Thangavelu Rajendra Kumar. "Cobalt-Doped Cerium Oxide Nanoparticles: Enhanced Photocatalytic Activity under UV and Visible Light Irradiation." Materials Science in Semiconductor Processing 26 (2014): 218-224. https://dx.doi.org/10.1016/j.mssp.2014.03.054.

12. Florea, Ileana, Cédric Feral-Martin, Jérome Majimel, Dris Ihiawakrim, Charles Hirlimann, and Ovidiu Ersen. "Three-Dimensional Tomographic Analyses of CeO_2 Nanoparticles." Crystal Growth & Design 13, no. 3 (2013): 1110-21. https://dx.doi.org/10.1021/cg301445h.

13. Tan, Joyce Pei Ying, Hui Ru Tan, Chris Boothroyd, Yong Lim Foo, Chao Bin He, and Ming Lin. "Three-Dimensional Structure of CeO_2 Nanocrystals." The Journal of Physical Chemistry C 115, no. 9 (2011): 3544-3551. https://dx.doi.org/10.1021/jp1122097.

14. Bojdys, M. J., J. O. Muller, M. Antonietti, and A. Thomas. "Ionothermal Synthesis of Crystalline, Condensed, Graphitic Carbon Nitride." Chemistry 14, no. 27 (2008): 8177-8182. https://dx.doi.org/10.1002/chem.200800190.

15. Tian, Na, Hongwei Huang, Chengyin Liu, Fan Dong, Tierui Zhang, Xin Du, Shixin Yu, and Yihe Zhang. "In Situ co-Pyrolysis Fabrication of CeO_2/g-C_3N_4 n–n Type Heterojunction for Synchronously Promoting Photo-Induced Oxidation and Reduction Properties." Journal of Materials Chemistry (2015): 17120-17129. https://dx.doi.org/10.1039/c5ta03669k.

16. Wang, Xinchen, Siegfried Blechert, and Markus Antonietti. "Polymeric Graphitic Carbon Nitride for Heterogeneous Photocatalysis." ACS Catalysis 2, no. 8 (2012): 1596-1606. https://dx.doi.org/10.1021/cs300240x.

17. Zhang, Qitao, Bin Xu, Saisai Yuan, Ming Zhang, and Teruhisa Ohno. "Improving g-C_3N_4 Photocatalytic Performance by Hybridizing with $Bi_2O_2CO_3$ Nanosheets." Catalysis Today 284 (2017): 27-36. https://dx.doi.org/10.1016/j.cattod.2016.10.027

18. Yan, S. C., Z. S. Li, and Z. G. Zou. "Photodegradation Performance of g-C_3N_4 Fabricated by Directly Heating Melamine." Langmuir 25, no. 17 (Sep 1 2009): 10397-10401. https://dx.doi.org/10.1021/la900923z

19. Zhao, Zaiwang, Yanjuan Sun and Fan Dong. "Graphitic Carbon Nitride Based Nanocomposites: A Review." Nanoscale 7, no. 1 (Jan 7 2015): 15-37. https://dx.doi.org/10.1039/c4nr03008g

20. Wu, Linen, Siman Fang, Lei Ge, Changcun Han, Ping Qiu, and Yongji Xin. "Facile Synthesis of Ag@CeO_2 Core-Shell Plasmonic Photocatalysts with Enhanced Visible-Light Photocatalytic Performance." J Hazard Mater 300 (Dec 30 2015): 93-103. https://dx.doi.org/10.1016/j.jhazmat.2015.06.062.

21. Zhang, Xiaodong, Xiao Xie, Hui Wang, Jiajia Zhang, Bicai Pan, and Yi Xie. "Enhanced Photoresponsive Ultrathin Graphitic-Phase C_3N_4 Nanosheets for Bioimaging." *J Am Chem Soc* 135, no. 1 (Jan 9 2013): 18-21. https://dx.doi.org/10.1021/ja308249k.

22. Xu, Bin, Qitao Zhang, Saisai Yuan, Ming Zhang, and Teruhisa Ohno. "Morphology Control and Characterization of Broom-Like Porous CeO_2." Chemical Engineering Journal 260 (2015): 126-32. https://dx.doi.org/10.1016/j.cej.2014.09.001

23. Zhang, Xiaodong, Xiao Xie, Hui Wang, Jiajia Zhang, Bicai Pan, and Yi Xie. "Enhanced Photoresponsive Ultrathin Graphitic-Phase C_3N_4 Nanosheets for Bioimaging." J Am Chem Soc 135, no. 1 (Jan 9 2013): 18-21. https://dx.doi.org/10.1021/ja308249k

24. Rangaswamy, Agolu, Putla Sudarsanam, Bolla Govinda Rao, and Benjaram M. Reddy. "Novel Molybdenum–Cerium Based Heterogeneous Catalysts for Efficient Oxidative Coupling of Benzylamines under Eco-Friendly Conditions." Research on Chemical Intermediates 42, no. 5

(2015): 4937-4950. https://dx.doi.org/10.1007/s11164-015-2332-7.

25. Ciston, James, Rui Si, Jose A. Rodriguez, Jonathan C. Hanson, Arturo Martínez-Arias, Marcos Fernandez-García, and Yimei Zhu. "Morphological and Structural Changes During the Reduction and Reoxidation of CuO/CeO_2 and $Ce1–xCu_xO_2$ Nanocatalysts: In Situ Studies with Environmental Tem, Xrd, and Xas." The Journal of Physical Chemistry C 115, no. 28 (2011): 13851-13859. https://dx.doi.org/10.1021/jp203882h.

26. Zhang, Feng, Siu-Wai Chan, Jonathan E. Spanier, Ebru Apak, Qiang Jin, Richard D. Robinson, and Irving P. Herman. "Cerium Oxide Nanoparticles: Size-Selective Formation and Structure Analysis." Applied Physics Letters 80, no. 1 (2002): 127-129. https://dx.doi.org/10.1063/1.1430502.

27. Zhou, X. D. and W. Huebner. "Size-Induced Lattice Relaxation in CeO_2 Nanoparticles." Applied Physics Letters 79, no. 21 (2001): 3512-3514. https://dx.doi.org/10.1063/1.1419235

28. Zhang, Jinshui, Xiufang Chen, Kazuhiro Takanabe, Kazuhiko Maeda, Kazunari Domen,* Jan Dirk Epping, Xianzhi Fu, Markus Antonietti, and Xinchen Wang. "Synthesis of a Carbon Nitride Structure for Visible-Light Catalysis by Copolymerization." Angew Chem Int Ed Engl 49, no. 2 (2010): 441-444. https://dx.doi.org/10.1002/anie.200903886

29. Liu, Jinghai, Tiekai Zhang, Zhichao Wang, Graham Dawson, and Wei Chen. "Simple Pyrolysis of Urea into Graphitic Carbon Nitride with Recyclable Adsorption and Photocatalytic Activity." *Journal of Materials Chemistry* 21, no. 38 (2011)14398. https://dx.doi.org/10.1039/c1jm12620b.

30. Abbasi, Zahra, Mohammad Haghighi, Esmaeil Fatehifar, and Nader Rahemi. "Comparative Synthesis and Physicochemical Characterization of CeO_2 nanopowder Via Redox Reaction, Precipitation and Sol-Gel Methods Used for Total Oxidation of Toluene." Asia-Pacific Journal of Chemical Engineering 7, no. 6 (2012): 868-876. https://dx.doi.org/10.1002/apj.652

31. Hu, Shichao, Feng Zhou, Lingzhi Wang, and Jinlong Zhang. "Preparation of Cu_2O/CeO_2 Heterojunction Photocatalyst for the Degradation of Acid Orange 7 under Visible Light Irradiation." Catalysis Communications 12, no. 9 (2011): 794-797. https://dx.doi.org/10.1016/j.catcom.2011.01.027

32. Yao, Xiaojiang, Changjin Tang, Zeyang Ji, Yue Dai, Yuan Cao, Fei Gao, Lin Dong, and Yi Chen. "Investigation of the Physicochemical Properties and Catalytic Activities of $Ce_{0.67}M_{0.33}O_2$(M = Zr^{4+}, Ti^{4+}, Sn^{4+}) Solid Solutions for NO Removal by CO." Catal. Sci. Technol. 3, no. 3 (2013): 688-698. https://dx.doi.org/10.1039/c2cy20610b

33. He, Yiming, Yan Wang, Lihong Zhang, Botao Teng, and Maohong Fan. "High-Efficiency Conversion of CO_2 to Fuel over ZnO/g-C_3N_4 Photocatalyst." Applied Catalysis B: Environmental 168-169 (2015): 1-8. https://dx.doi.org/10.1016/j.apcatb.2014.12.017

34. Ji, Huanhuan, Fei Chang, Xuefeng Hu, Wei Qin, and Jiaowen Shen. "Photocatalytic Degradation of 2,4,6-Trichlorophenol over g- C_3N_4 under Visible Light Irradiation." Chemical Engineering Journal 218 (2013): 183-190. https://dx.doi.org/10.1016/j.cej.2012.12.033

35. Cao, Shao-Wen, Yu-Peng Yuan, James Barber, Say Chye Joachim Loo, and Can Xue. "Noble-Metal-Free g- C_3N_4/Ni(dmgH)$_2$ Composite for Efficient Photocatalytic Hydrogen Evolution under Visible Light Irradiation." Applied Surface Science 319 (2014): 344-349.

https://dx.doi.org/10.1016/j.apsusc.2014.04.094

36. Huang, Ze'ai, Qiong Sun, Kangle Lv, Zehui Zhang, Mei Li, and Bing Li. "Effect of Contact Interface between TiO_2 and g-C_3N_4 on the Photoreactivity of g-C_3N_4/TiO_2 Photocatalyst: (001) Vs (101) Facets of TiO_2." Applied Catalysis B: Environmental 164 (2015): 420-427. https://dx.doi.org/10.1016/j.apcatb.2014.09.043

37. Huang, Liying, Yeping Li, Hui Xu, Yuanguo Xu, Jixiang Xia, Kun Wang, Huaming Li, and Xiaonong Cheng. "Synthesis and Characterization of CeO_2/g-C_3N_4 Composites with Enhanced Visible-Light Photocatatalytic Activity." Rsc Advances 3, no. 44 (2013). https://dx.doi.org/10.1039/c3ra42712a

38. Xu, Bin, Qitao Zhang, Saisai Yuan, Ming Zhang, and Teruhisa Ohno. "Synthesis and Photocatalytic Performance of Yttrium-Doped CeO_2 with a Porous Broom-Like Hierarchical Structure." Applied Catalysis B: Environmental 183 (2016): 361-70. https://dx.doi.org/10.1016/j.apcatb.2015.10.021.

39. Dumrongrojthanath, Phattharanit, Titipun Thongtem, Anukorn Phuruangrat, and Somchai Thongtem. "Hydrothermal Synthesis of Bi2wo6 Hierarchical Flowers with Their Photonic and Photocatalytic Properties." Superlattices and Microstructures 54 (2013): 71-77. https://dx.doi.org/10.1016/j.spmi.2012.11.001

40. Deng, Fang, Yin Liu, Xubiao Luo, Dezhi Chen, Shaolin Wu, and Shenglian Luo. "Enhanced Photocatalytic Activity of Bi_2WO_6/TiO_2 Nanotube Array Composite under Visible Light Irradiation." Separation and Purification Technology 120 (2013): 156-161. https://dx.doi.org/10.1016/j.seppur.2013.09.032.

41. Wang, Guofeng, Qiuying Mu, Ting Chen, and Yude Wang. "Synthesis, Characterization and Photoluminescence of CeO_2 Nanoparticles by a Facile Method at Room Temperature." Journal of Alloys and Compounds 493, no. 1-2 (2010): 202-207. https://dx.doi.org/10.1016/j.jallcom.2009.12.053.

42. Channei, D., B. Inceesungvorn, N. Wetchakun, S. Ukritnukun, A. Nattestad, J. Chen, and S. Phanichphant. "Photocatalytic Degradation of Methyl Orange by CeO_2 and Fe-Doped CeO_2 Films under Visible Light Irradiation." Sci Rep 4 (Aug 29 2014): 5757. https://dx.doi.org/10.1038/srep05757.

43. Tian, Na, Hongwei Huang, Chengyin Liu, Fan Dong, Tierui Zhang, Xin Du, Shixin Yu, and Yihe Zhang. "In Situ co-Pyrolysis Fabrication of CeO_2/g-C_3N_4 n–n Type Heterojunction for Synchronously Promoting Photo-Induced Oxidation and Reduction Properties." Journal of Materials Chemistry A 3, no. 33 (2015): 17120-17229. https://dx.doi.org/10.1039/c5ta03669k.

44. Ji, Pengfei, Jinlong Zhang, Feng Chen, and Masakazu Anpo. "Study of Adsorption and Degradation of Acid Orange 7 on the Surface of CeO_2 under Visible Light Irradiation." Applied Catalysis B: Environmental 85, no. 3-4 (2009): 148-154. https://dx.doi.org/10.1016/j.apcatb.2008.07.004.

Part 5.

Conclusions and Outlooks

5.1 General conclusions

In this dissertation, the basic photocatalytic reactions principle, preparation and applications of CeO_2-based photocatalysts are introduced firstly. Then, instead of the traditional single method of regulating CeO_2-based photocatalysts, some modification strategies mainly including RE metal ions doping, noble metal modification and coupling with PCN materials were applied. And the related photocatalytic applications of CH_3CHO degradation of materials prepared in my work with those reported papers were comprehensively investigated as **Table 5-1** in detail. The modification strategies used in my work can indeed solve the technical problem of low visible light utilization and high photogenerated carriers' recombination rate of traditional CeO_2-based photocatalytic materials.

Table 5-1 Comparison of CH_3CHO degradation properties over the materials prepared in my work with reported papers.

Samples	Light condition	CO_2 evolution (ppm)	Evolution rate (ppm/h)	Reference
CeO_2	300–800 nm	36	1.5	Part 1
Sm-CeO_2	300–800 nm	304	12.7	
Ag@Sm-CeO_2	420–800 nm	772	32.2	Part 2
Y-CeO_2/PCN	420–800 nm	932	**39.1**	Part 3
Sm-CeO_2/PCN	420–800 nm	938	38.8	
P25	400–800 nm	21	0.9	Appl. Catal. B Environ. 142 (2013) 362–367.
S-TiO_2	400–800 nm	125	5.2	
Fe(III)-Pt(II)/TiO_2	LED 455 nm	325	65	Appl. Catal. A-Gen. 634 (2022) 118539.
Y-CeO_2	LED 365 nm (UV)	345	14.4	Appl. Catal. B Environ. 164 (2015) 120–127.
$Bi_2O_2CO_3$/PCN	LED 435 nm	670	27.9	Catal. Today 315 (2018) 18.

Doped-CeO_2 can generally narrow the bandgap and enhance the absorption of visible light. Doping RE metal ions also form a trapping center in CeO_2, which inhibits the transport of charge carriers. Furthermore, due to the LSPR properties of precious metals, modification of Ag quantum dots on CeO_2 can further improve its response to visible light. In addition, coupling CeO_2 with PCN semiconductor can form heterojunction photocatalyst, which can improve the separation of electrons and holes and improve photocatalytic efficiency.

These above-mentioned modification strategies can solve the technical problems of low visible light utilization and high photogenerated carrier recombination rate of traditional CeO_2-based photocatalytic materials. Finally, visible light responsive composite photocatalytic materials with controllable morphology and uniform grain size can be prepared, including (Sm, Y, La and Nd)-doped CeO_2, Ag@Sm-CeO_2 and Y-doped CeO_2/PCN photocatalysts. And the experimental results indicated the photocatalytic performance followed the outstanding improved tendency when combining the strategies reasonably. This dissertation can provide a credible theoretical basis for realizing the practical application of other CeO_2-based photocatalysts.

5.2 Outlooks of the future work

Although CeO_2-based photocatalysts have the characteristics of broad light absorption to weak visible light compared to traditional photocatalysts such as TiO_2 and some other rare earth oxides, leading the CeO_2-based photocatalysts are promising materials. However, the low utilization of visible light still hinders the further application of solar photocatalysis. Some preparation process of products is complicated, and the yield is meager. Therefore, a simple and high yield synthesis strategy is demanded for CeO_2-based photocatalysts in our laboratory. And it is still urgent to solve the problem of capacity loss and recovery in photocatalyst recycling.

Additionally, since dyes degrade quickly, the majority of studies used dyes as research subjects to comprehend how photocatalytic technology degrades. But a few uses persistent organic pollutants as a model. Therefore, it is still necessary for us to further understand the degradation mechanism and charge transfer pathway. These scientific problems are significant for the practical application of CeO_2 matrix composites in the photodegradation of organic pollutants on our daily environment.

List of Publications

[1] **H. Yang**, L. Jia, B. Xu, Q. Zhang, Z. Nan, M. Zhang, T. Ohno, Constructing cerium-based isogenous S-scheme heterojunction for photocatalytic removal of trace acetaldehyde, ***Environmental Science & Technology***, (2023) Submitted.

[2] **H. Yang**, L. Jia, Z. Zhang, B. Xu, Q. Zhang, S. Yuan, Y. Xiao, Z. Nan, M. Zhang, Y. Zhang, T. Ohno, Enhanced photocatalytic VOCs degradation performance on Fe-doped ceria under visible light, ***Applied Materials Today***, 29 (2022) 101651.

[3] **H. Yang**, L. Jia, J. Haraguchi, Y. Wang, B. Xu, Q. Zhang, Z. Nan, M. Zhang, T. Ohno, Nitrogen and sulfur co-doped CeO_2 nanorods for efficient photocatalytic VOCs degradation, ***Catalysis Science & Technology***, 12 (2022) 5203-5209.

[4] **H. Yang**, L. Jia, Z. Zhang, B. Xu, Z. Liu, Q. Zhang, Y. Cao, Z. Nan, M. Zhang, T. Ohno, Novel cerium-based MOFs photocatalyst for photocarrier collaborative performance under visible light, ***Journal of Catalysis***, 405 (2022) 74-83.

[5] **H. Yang**, B. Xu, Q. Zhang, S. Yuan, Z. Zhang, Y. Liu, Z. Nan, M. Zhang, T. Ohno, Boosting visible-light-driven photocatalytic performance of waxberry-like CeO_2 by samarium doping and silver QDs anchoring, ***Applied Catalysis B: Environmental***, 286 (2021) 119845.

[6] B. Xu, **H. Yang**, Q. Zhang, S. Yuan, A. Xie, M. Zhang, T. Ohno, Design and Synthesis of Sm, Y, La and Nd-doped CeO_2 with a broom-like hierarchical structure: a photocatalyst with enhanced oxidation performance, ***ChemCatChem***, 12 (2020) 2638-2646. (Equal contribution)

[7] **H. Yang**, B. Xu, S. Yuan, Q. Zhang, M. Zhang, T. Ohno, Synthesis of Y-doped CeO_2/PCN nanocomposited photocatalyst with promoted photoredox performance, ***Applied Catalysis B: Environmental***, 243 (2019) 513-521.

[8] C. Chen, Q. Zhang, **H. Yang**, Lei Yu, Establishing Fe-Cu interaction in a novel free-standing material to boost the catalytic activity for ligand-free Suzuki-Miyaura cross-couplings, ***Journal of Catalysis***, 416 (2022) 176-185.

[9] J. Bai, Y. Kong, Z. Liu, **H. Yang**, M. Li, D. Xu, Q. Zhang, Ag modified Tb-doped double-phase In_2O_3 for ultrasensitive hydrogen gas sensor, ***Applied Surface Science***, 583 (2022) 152521.

[10] Y. Cao, S.N. Lou, S. Wang, **H. Yang**, Q. Zhang, C. Wang, N. Murakami, T. Ohno, Fe(III)-Pt(II) oxide-co-sensitized brookite TiO_2 nanorods for photocatalytic degradation of acetaldehyde under visible light, ***Applied Catalysis A: General***, 634 (2022) 118539.

[11] C. Chen, Z. Teng, M. Yasugi, **H. Yang**, Y. Cao, L. Yu, T. Ohno, A homogeneous copper bismuth sulfide photocathode prepared by spray pyrolysis deposition for efficient photoelectrochemical hydrogen generation, ***Materials Letters***, 325 (2022) 132801.

[12] A. Xie, S.-W. Mao, T.-J. Chen, **H. Yang**, M. Zhang, Microstructure and properties of cerium oxide/polyurethane elastomer composites, ***Rare Metals***, 40 (2021) 3685-3693.

Acknowledgements

Time flies, two and a half years-doctoral studies and scientific research life at the Kyushu Institute of Technology is coming to an end and it is very unforgettable for me. In the future study and work, I will always remember the inculcate of all the teachers and continue to work hard.

First of all, I would like to extend my most sincere thanks to my supervisors of Prof. Teruhisa Ohno, who gave me full, serious and meticulous guidance in many aspects such as thesis topic selection, experimental design, mechanism elaboration, paper writing and submission. And Ohno sensei's wealth of knowledge and high moral character was a source of respect. Also, I want to express my gratitude to my Chinese supervisors in Yangzhou University of Prof. Bin Xu, Prof. Ming Zhang and Prof. Zhaodong Nan, for giving me such a precious opportunity to join the dual-degree joint program between Yangzhou University and Kyushu Institute of Technology. I was deeply impressed by the four teachers' solid theoretical and practical literacy, rigorous scientific research style and optimistic and positive attitude towards life.

I also would like to express my sincere thanks to Professor Youichi Shimizu, Professor Toshiki Tsubota, and Professor Naoya Murakami for help me in revising doctoral dissertation. I also want to thank for Dr. Cao Yu, Dr. Chao Chen, Ms. Yue Wang, Dr. Wenan Cai, Dr. Xiaoyu Sun, Dr. Katsuichiro Kobayashi, Yoshioka Mari san, Jun Haraguchi san, Nishihara san and other students in the Ohno lab for their help on my daily life. In addition, I would like to express my heartfelt thanks to Professor Lifeng Zhang in the Department of Electrical and Engineering, and Mrs. Dongming Wang in the Student Section for their help in my life at KIT.

Finally, I need to thank my parents and families for their support, understanding, companionship and tolerance, which made it perfect for me to complete my studies in Japan.

Hui Yang

2023.01.30